Synthesis and characterisation of small molecule and macromolecular photoredox catalysts for radical thiol-ene reactions

Nozuko Motimani

University of Cape Town

February 2021

Synthesis and characterisation of small molecule and macromolecular photoredox catalysts for radical thiol-ene reactions

Nozuko Motimani

Dissertation presented for the degree of

Master of Science in Chemistry

University of Cape Town

Department of Chemistry

Supervisor: Associate Professor Gregory S. Smith (UCT)

February 2021

Plagiarism Declaration

I know the meaning of plagiarism and declare that all work contained in the document **"Synthesis and characterisation of small molecule and macromolecular ruthenium(II) complexes as photoredox catalysts for olefin transformation reactions"** is my own work and that all sources of information I have used or quoted have been acknowledged by means of complete referencing. By submitting this dissertation, I declare that to the best of my knowledge, this work has never been submitted for examination for any degree at any university.

Signed by candidate

29/01/2021

---------- ----------

Signature Date

Acknowledgements

I want to express my deepest gratitude to my supervisor, Assoc. Prof. G. S. Smith, for welcoming me to his research group and providing me with immense knowledge, expertise and training. The door to his office was always open whenever I needed guidance with regards to my research project. I really appreciate his constant encouragement, constructive comments and for sharing his pearls of wisdom and assistance during the course of this research. I would also like to thank Dr S. Ngubane for his invaluable expertise, training and input towards my project, particularly with respect to electrochemistry.

I am also grateful for my fellow colleagues and friends, Taryn Golding, Sinethemba Mkhize and Thato Medupe who kept me going through the ups and downs I faced throughout this venture and for sharing great experiences with me. I thank Dr Shepherd Siangwata, my fellow colleague and friend, for his patience in the laboratory when I started this project and for his unwearied help and advice. My appreciation also goes to Stephen de Doncker for the time and energy he spent on proofreading my dissertation Chapters.

I take this opportunity to express my gratitude to the members of the GS Organometallic research group for their great ideas and input in our group meetings that encouraged me to think outside the box with respect to my research project. Also, the University of Cape Town for giving me the opportunity to pursue my MSc degree and the Chemistry Department for their support, and the facilities they made available for me to be able to get to this final stage of my research.

A special thanks goes to Sasol for their financial support towards my studies, I would not have been able to pursue this degree if it was not for their continuous support.

Finally, I would like to express my profound appreciation to my mother, sister and friends for their unfailing support, encouragement and motivation throughout my studies.

Thank you all for your support!

Abstract

The use of polynuclear complexes is attracting significant attention, offering several advantages over mononuclear analogues. In the context of this project, the presence of several photoactive centres can lead to a multi-electron transfer in a single step and offering other modalities. With the aim to improve the reactivity and stability of photoredox catalysts, multinuclear photoredox catalysts were developed. Consequently, bipyridyl monomeric and trimeric ligands functionalised with imine and amine functionalities were synthesised *via* Schiff base condensation and reductive amination reactions, respectively. The ligands were then reacted with *cis*-dichlorobis(2,2'-bipyridine)ruthenium(II) to afford two new mononuclear and two new trinuclear Ru(II)-based complexes. The resulting complexes were then fully characterised by various spectroscopic and analytical techniques such as ^{1}H NMR, ^{13}C{^{1}H} NMR, FT-IR spectroscopy and mass spectrometry. Furthermore, electrochemical, electronic absorption and emission studies for the complexes were conducted and the collected data displayed the effects of ligand modifications on the photophysical and redox properties of the complexes. All the ligand-modified complexes exhibited red shifted emission spectra (614−633 nm) relative to the $[Ru(bpy)_3](PF_6)_2$ complex (609 nm) and this emission band was attributed to the transition from the triplet metal-to-ligand charge transfer excited-state (^{3}MLCT) to the ground-state.

The excited-state redox potentials for the ligand-modified complexes were comparable to that of the known complex thus displaying promising photocatalytic activity. The photoexcited $[Ru(bpy)_3]^{2+}$ complex had the most positive excited-state reduction potential ($E_{red\ (2+*/+)}$ = +0.350 V vs Ag/Ag^{+}), making it a more potent oxidant than the photoexcited states of the ligand-modified complexes. The complexes were then evaluated as photoredox catalysts in the radical hydrothiolation reaction of olefins (thiol-ene reactions) to produce thioethers, which are valuable starting materials in the pharmaceutical industry, material and polymer science.

The isolated yields, from the reaction between thiophenol and styrene, were higher for the $[Ru(bpy)_3](PF_6)_2$ complex (54%) in comparison to the ligand-modified mononuclear complexes (8–24%). This result was expected since $[Ru(bpy)_3](PF_6)_2$ exhibited the most positive excited-state reduction potential ($E_{red\ (2+*/+)}$ = +0.350 V vs Ag/Ag^{+}), making the photoexcited state of this complex more readily quenched by the thiophenol. Control reactions

carried out in the absence of the photocatalyst resulted in either significantly lower yields (6%) or no product formation, showing the role of the complexes as photoredox catalysts in the reactions. Varying the substrates by using styrene and 1-butanethiol afforded the desired coupled thioether product, while the reaction between thiophenol and allyl alcohol resulted in the formation of the disulfide product. However, when allyl alcohol was reacted with 1-butanethiol, the desired anti-Markovnikov thioether product was formed and this indicated the importance of substrate choice and compatibility with the photoexcited catalyst when designing a photocatalytic system.

The reactions carried out using trinuclear complexes ($E_{red\ (2+*/+)}$ = +0.300 V vs Ag/Ag^+ for each metal centre) resulted in almost a three-fold increase in isolated yields (26% (mononuclear), 73% (trinuclear)) when compared to their respective mononuclear analogues (8% (mononuclear), 22% (trinuclear)). This demonstrated the benefits of having a multinuclear photocatalyst with several photoactive centres.

Abbreviations, Symbols and Units

°	Degrees
°C	Degrees celsius
δ	Chemical shift
ε	Molar attenuation coefficient
ν	Wavenumber
ΔG_{ES}	Gibbs free energy for excited-state
λ_{abs}	Absorption wavelength
λ_{em}	Emission wavelength
λ_{ex}	Excitation wavelength
aq.	Aqueous
Ar	Aromatic
Ar-H	Aromatic proton
ATR-IR	Attenuated total reflectance infrared spectroscopy
bpy	2,2'-Bipyridine
bpz	2,2'-Bipyrazine
^{13}C NMR	Carbon-13 nuclear magnetic resonance
calcd.	Calculated
$CDCl_3$	Deuterated chloroform
CD_3CN	Deuterated acetonitrile
$(CD_3)_2CO$	Deuterated acetone
CD_3OD	Deuterated methanol
$(CD_3)_2SO$	Deuterated dimethyl sulfoxide
cm^{-1}	Reciprocal centimetres
d	Doublet
dd	Doublet of doublets
ddd	Doublet of doublets of doublets
dq	Doublet of quartets
dt	Doublet of triplets
eq.	Equivalents
ESI-MS	Electrospray ionisation mass spectrometry
eV	Electronvolt(s)

FT-IR	Fourier transform infrared spectroscopy
g	Gram(s)
g/mol	Gram(s) per mol
h	Hour(s)
^{1}H NMR	Proton nuclear magnetic resonance
HOMO	Highest occupied molecular orbital
HR	High resolution
HSQC	Heteronuclear single quantum correlation
Hz	Hertz
ISC	Intersystem crossing
IR	Infrared
J	Coupling constant
kcal/mol	Kilocalorie per mole
LC-MS	Liquid chromatography-mass spectrometry
LED	Light emitting diode
LUMO	Lowest unoccupied molecular orbital
m	Meter(s) for length, or multiplet for nuclear magnetic resonance
mg	Milligram(s)
MHz	Megahertz
mL	Millilitre
MLCT	Metal-to-ligand charge transfer
^{1}MLCT	Singlet state metal-to-ligand charge transfer
^{3}MLCT	Triplet state metal-to-ligand charge transfer
mol	Mole(s)
mmol	Millimole(s)
MS	Mass spectrometry
mV	Millivolt(s)
mV/s	Millivolt(s) per second
m/z	Mass to charge ratio
nm	Nanometres
NMR	Nuclear magnetic resonance
PGM	Platinum group metals
ppm	Parts per million

q	Quartet
qd	Quartet of doublets
rt	Room temperature
Ru(II)	Ruthenium(II)
*Ru(II)	Excited-state of ruthenium(II)
s	Singlet (NMR), or strong (IR)
SET	Single-electron transfer
t	Triplet
td	Triplet of doublets
TON	Turnover number
UV	Ultraviolet
V	Volt(s)

Table of contents

Chapter 1

A general overview of the development of transition metal photocatalysis and applications in organic synthesis

Chapter 2

Synthesis and characterisation of mononuclear and multinuclear ruthenium complexes

Chapter 3

Evaluation of ligand-modified ruthenium(II) complexes as visible-light photoredox catalysts for the hydrothiolation reaction of olefins

Chapter 1

A general overview of the development of transition metal photocatalysis and applications in organic synthesis

1.1 Introduction to catalysis

Catalysis is a cornerstone of synthetic chemistry due to more than 80% of chemicals and materials that are manufactured globally by means of catalytic processes.[1] Catalytic processes enable the production of useful compounds following energy-efficient, economical and environmentally friendly strategies. Furthermore, this allows the control of crucial factors in synthetic chemistry, such as selectivity towards specific products as well as improved stability of formed intermediates during the catalytic process.[2]

Catalysts can generally be classified as either heterogeneous or homogeneous, and this study focuses on the latter, which is widely applied in the bulk and fine chemicals industry.[2] Homogeneous catalysts are more versatile than heterogeneous catalysts, and exist in the same phase as the reactants and products.[2] This allows for the ease to fine-tune properties such as reactivity and stability, through either changing ligands coordinated to the metal centre or through changing the metal centre.[2,3] Many organic transformations that were previously unachievable under catalyst-free conditions have been successfully carried out using homogeneous catalysts. Examples of such processes include the well-known palladium-catalysed cross-coupling reaction, selective hydrogenation, olefin metathesis, C−H functionalisation as well as the industrially popular hydroformylation reaction.[4-7]

Organic transformations utilising transition metal catalysts, such as those mentioned above, were developed to facilitate reaction products in yields unachievable for stoichiometric organic synthesis. However, some of these catalytic processes require harsh reaction conditions, such as high temperatures, to activate the catalyst.[8,9] In light of this, the use of alternative forms of energy such as photochemical energy is necessary, especially from the viewpoint of Green Chemistry since light is known to be an abundant, inexpensive, clean and renewable source of energy.[10,11] Visible-light has been shown to provide photon energies in the 71–38 kcal/mol range, which is comparable to the energy barrier of most transition metal-catalysed reaction under thermal conditions.[5] One of the first scientists to realize the use of light to promote

chemical reactions was Giacomo Ciamician, inspired by nature's ability to convert solar energy to chemical energy in photosynthesis in 1908.[12] Ciamician's work pioneered modern developments in photochemistry, being the first to study photochemical reactions in a systematic way, towards efforts in understanding the energy or electron transfer pathways involved in natural photosynthesis. The field of photochemistry has since found widespread applications in the solar energy conversion industry and organic syntheses, where researchers have developed catalytic systems that mimic photosynthesis for the production of useful precursors such as hydrogen in water oxidation (Figure 1.1).[13-15]

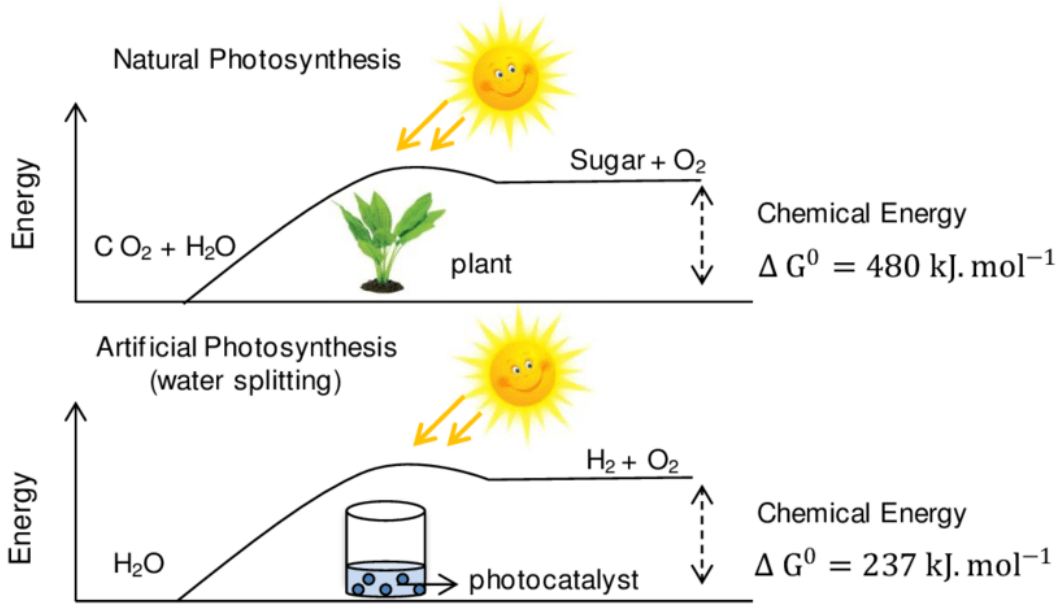

Figure 1.1 Energy diagram of natural photosynthesis and photocatalysed water-splitting reaction.[16]

Traditionally, photochemical reactions make use of high energy ultraviolet (UV) light, requiring specialised photo-reactors and these systems are often inefficient and unsustainable compared to the direct utilization of incident sunlight or visible-light.[13] Additionally, the required wavelengths for these processes are not abundant in the solar spectrum. Recent research has therefore focused on the use of low energy visible-light as an energy source for photochemical reactions.[13]

1.2 Transition metal complexes as visible-light photoredox catalysts

Several advances have been made towards the use of visible-light for the rapid and efficient synthesis of organic compounds.[17-19] However, the lack of the ability to absorb visible-light by many organic molecules has significantly limited the application of photochemical reactions on an industrial scale.[17,20,21] In an effort to find new and efficient processes that utilise visible-light, scientists have designed and synthesised photocatalysts, which are compounds that are able to absorb visible light and initiate the desired chemical transformations.[22] It has become a powerful tool for several favourable reasons, for example, it occurs at relatively mild reaction conditions, yields high efficiency and provides better selective excitation of the photocatalyst, consequently aiding in preventing or minimising the formation of undesirable reaction by-products.[18,23]

Transition metal-based complexes play a significant role in a variety of light-induced chemical processes such as photoredox catalysis.[24] Types of photoredox catalysts that have been developed in the past decades include organic dye molecules,[25] inorganic semiconductors[26] and hybrid systems which are a combination of an organic dye, semiconductor and an organometallic complex.[27] Transition metal complexes have become the preferred choice for visible-light photoredox catalysis.[28] Metal-based photoredox catalysts are more versatile in that their ligands can be modified or the metal ion exchanged unlike their purely organic counterparts (Figure 1.2, **I** and **II**). These suffer from drawbacks including inefficient reaction systems which require sacrificial electron donors to reduce to their corresponding active species.[10,28,29]

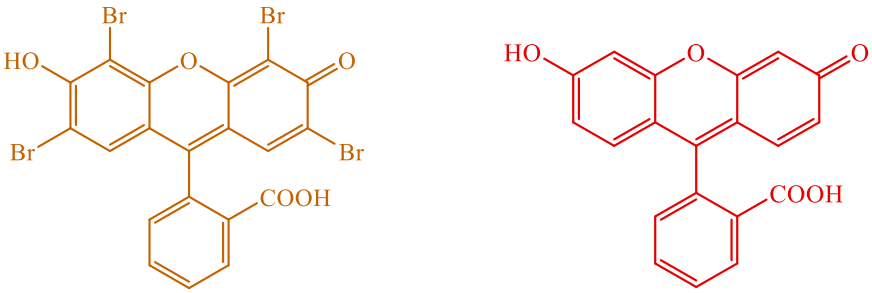

(**I**) (**II**)

Figure 1.2 Examples of common organic dyes, eosin-Y (**I**) and fluorescein (**II**), used in photoredox catalysis.[10]

The most widely studied transition metal photoredox catalysts are based on the rare, fast-depleting and expensive second- and third-row transition metals such as ruthenium and iridium.[1,30] There are, however, few examples of photoredox catalysts using first-row transition metals such as iron, copper, cobalt, chromium and nickel.[31-33] The use of these complexes containing first-row metals require further development owing to their inability to engage in photoinduced electron transfer processes upon photoexcitation.[6] By way of example, Ferrere and Gregg described the first functional dye-sensitized solar cell designed by using an iron(II)-based polypyridyl complex (Figure 1.3, **III**) for the injection of an electron into a nanocrystalline TiO_2 conduction band.[34] Even though this solar cell was functional, the measured efficiency was significantly lower compared to its ruthenium(II) analogue. This was attributed to an extremely short-lived, non-emissive excited state (*ca*. in the picosecond range), making it a poor candidate for this system.[34] Gualandi *et al*. reported the first use of $[Fe(bpy)_3]Br_2$ (Figure 1.3, **IV**) for stereoselective organic synthesis under visible-light photoredox catalytic conditions.[30] This iron(II) complex successfully photocatalysed the reaction between hydrocinnamaldehyde and dimethyl bromomalonate upon irradiation with visible-light. Although this complex was highly effective as a photoredox catalyst, the excellent enantioselectivity that was observed at room temperature was due to a combination of the photoredox catalyst, an organocatalyst and a redox mediator.[30]

In 2012, Hwang *et al*. reported a copper-catalysed Sonogashira reaction of aryl halides that was initiated by visible-light irradiation at room temperature.[35] The reaction generated copper-acetylide as an intermediate, which was subsequently photoexcited to access the excited-state responsible for the accelerated reaction using copper(I) chloride salt.[35] Interestingly, this reaction was carried out under mild conditions in contrast to the conventional palladium-catalysed reaction which required thermal energy input. Sonogashira coupling reactions of aryl halides catalysed by a copper complex are known to undergo a sluggish oxidative addition step.[36] Under dual copper/photoredox catalytic conditions, reactions proceeded efficiently with moderate to good yields (38-96%).[37] More recently, Engl and Reiser reported a visible light-mediated, copper-catalysed (Figure 1.3, **V**) atom transfer radical addition (ATRA) reaction that enabled efficient, vicinal difunctionalisation of olefins using iodoform.[38] The reaction proceeded with an excellent yield of 97% for the desired product upon irradiation with green LED light at 530 nm.

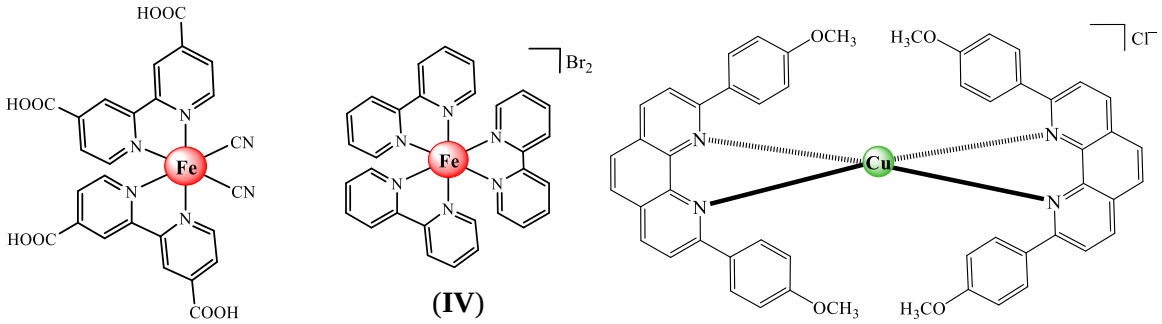

Figure 1.3 Structures of first-row transition metal complexes evaluated by Ferrere and Gregg (**III**),[34] Gualandi *et al*. (**IV**)[30] and Engl and Reiser (**V**)[38] as photoredox catalysts.

Visible-light photoredox catalysis has shown promise as an alternative for several reactions, including those that have been well-developed. By example, the Heck coupling reaction of C(sp^3) hybridised alkyl electrophiles, which are known to be challenging reactions, have utilised photoredox mediated catalysis.[39] The reaction provided the effective synthesis of functionalised allyl compounds such as allyl silanes from the corresponding α-heteroatom-substituted methyl halides – an organic transformation known to be difficult to achieve using traditional thermal methods.[39]

Due to their abundance, first-row transition metal complexes would advance the area of photocatalysis, however, research on these types of photoredox catalysts remains underdeveloped. This is due to bipyridyl catalysts containing first-row transition metal atoms exhibiting non-luminescent excited-states with insufficient lifetimes in the picosecond range.[30] For these reasons, research in photoredox catalysis largely utilises metal-based catalysts based on ruthenium and iridium ions (Figure 1.4, **VI-IX**).[36-43]

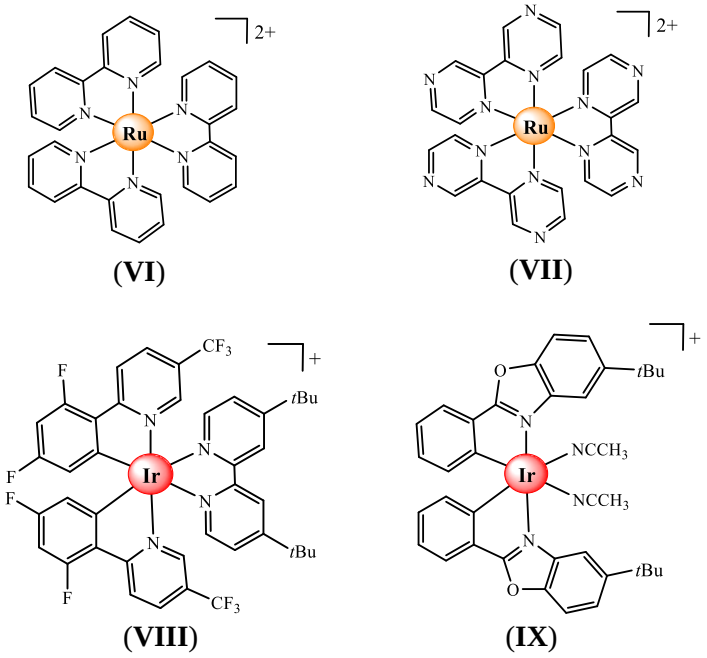

Figure 1.4 Typical structures of ruthenium- and iridium-based photoredox catalysts $[Ru(bpy)_3](PF_6)_2$ (**VI**), $[Ru(bpz)_3](PF_6)_2$ (**VII**), $[Ir(dF(CF_3)ppy)_2(t\text{Bu-bpy})](PF_6)$ (**VIII**) and iridium(I) benzoxazole complex [Λ-IrO](PF_6) (**IX**).[40-43]

These complexes exhibit unique photophysical and photochemical properties such as photostability, high activity and long-lived excited-states in the microsecond range.[44] They can also be modified by introducing substituents on the ligands within the coordination sphere to tailor the complexes for various applications ranging from solar energy harvesting, chemical sensing, photodynamic therapy and molecular self-assembly (Figure 1.5).[45,46]

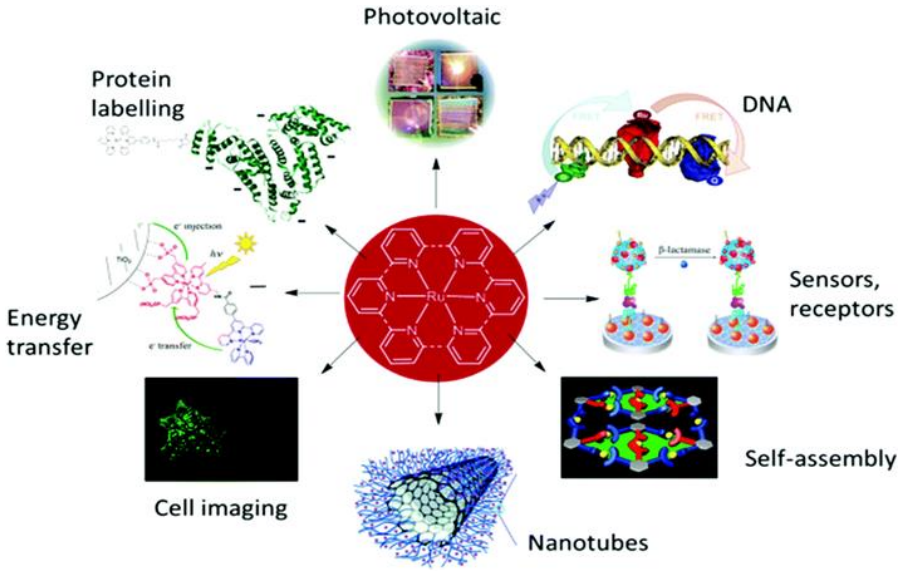

Figure 1.5 Different applications of ruthenium-based photocatalysts taken from the 2018 review article by Mede *et al.*[46]

1.3 Ruthenium(II) polypyridyl complexes as photoredox catalysts

One of the first examples of ruthenium-based photoredox catalysts was reported by Kellogg and co-workers in the 1970s.[47] Their study describing a photo-induced reduction of sulfonium ions to the corresponding alkanes and thioethers was established using *N*-substituted 1,4-dihydropyridines as a terminal reductant and $[Ru(bpy)_3]Cl_2$ as the photoredox catalyst.[47,48] Thereafter, Deronzier *et al.* reported the first successful net oxidative reaction involving the conversion of benzylic alcohols to their corresponding aldehydes using aryldiazonium salts and a ruthenium bipyridyl complex as the terminal oxidant and photoredox catalyst, respectively.[49] Furthermore, the authors discovered that the Pschorr reaction could be catalysed by $[Ru(bpy)_3]Cl_2$ – a reaction usually catalysed by a copper catalyst often resulting in low yields.[50,51] This reaction involves the intramolecular substitution of aromatic compounds *via* aryladiazonium salts intermediates.[51] Additionally, they observed that the quantum efficiency of the reaction was higher under photoredox catalytic conditions than in direct photolysis of the reaction mixture resulting in quantitative yields of the phenanthrene product (Scheme 1.1).[52,53]

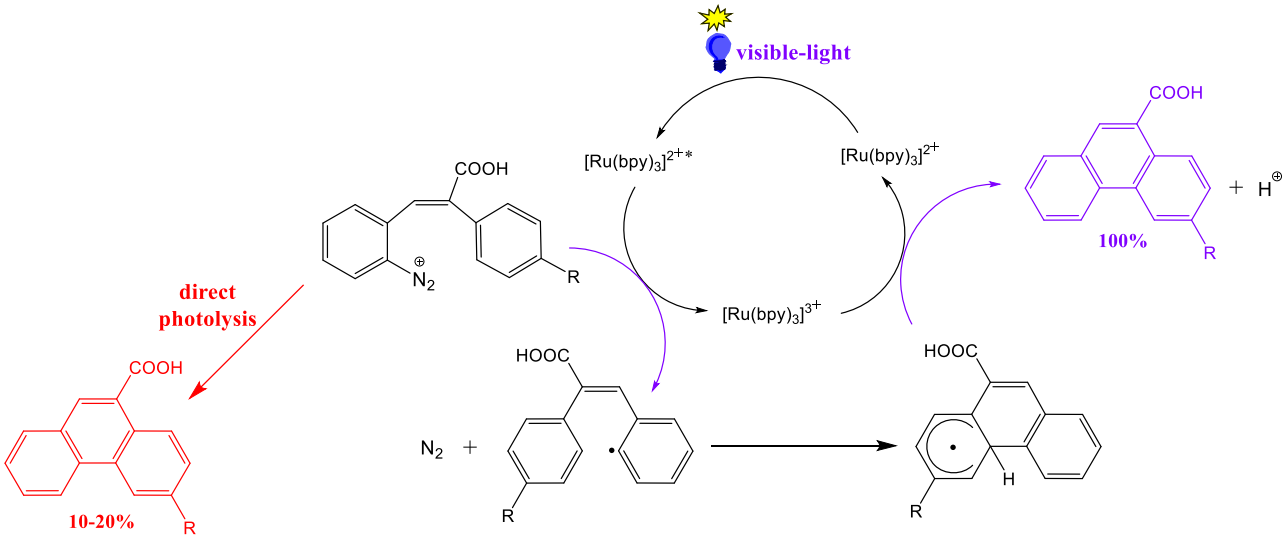

Scheme 1.1 Reaction mechanism of the photoredox-catalysed Pschorr reaction by Deronzier and co-workers.[53]

In spite of these findings, the potential of photoredox catalysis in organic synthesis remained relatively unacknowledged until the late 2000s.[22] An exponential increase in the number of publications (Figure 1.6) pertaining to the use of photoredox catalysts in organic synthesis resulted in renewed interest in the field.[22] Yoon and co-workers disclosed an intramolecular [2+2] enone cycloaddition reaction in 2008 that was carried out in the presence of a photoredox

catalyst resulting in excellent diastereoselectivity toward the formation of cyclobutane products.[54] A few years later, Stephenson's group reported a photoredox-catalysed aza-Henry reaction that successfully functionalised *N*-arylamines with nitroalkanes under mild reaction conditions.[55]

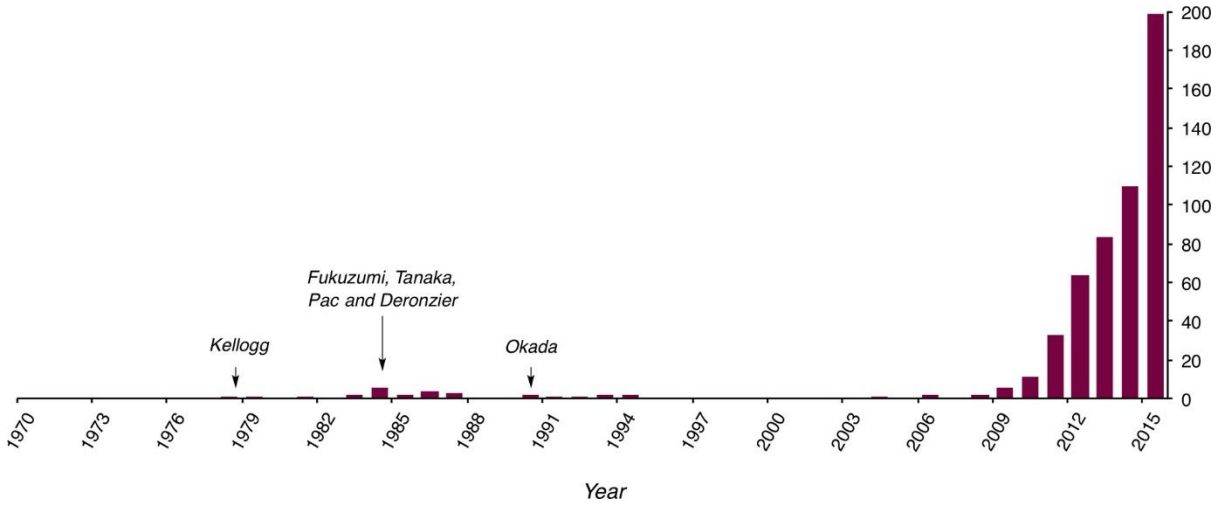

Figure 1.6 Number of publications that employ photoredox catalysis taken from the 2016 perspective article by Shaw *et al.*[22]

MacMillan and co-workers also made significant contributions towards the design of photoredox-catalysed organic reactions when they developed a dual photoredox catalytic system that merged an organocatalyst and a metal-based photoredox catalyst.[15] By utilising a ruthenium-based photocatalyst, they mediated the radical dehalogenation of an α-bromocarbonyl, generating a reactive radical intermediate.[15] The organocatalyst then activated the aldehyde towards enantioselective functionalization at the α-position.[56,57] From these selected examples, it is clear that ruthenium polypyridyl complexes show promise to the advancement of green organic synthesis and these complexes continue to play a significant role in a wide range of applications today.

1.4 Properties of ruthenium(II) polypyridyl complexes for visible-light photoredox catalysis

The photochemistry of transition metals with a d^6 electronic configuration have shown to be useful in the design of light-enabled processes, particularly, the ruthenium polypyridyl complexes.[58,59] This is attributed to unique properties exhibited by these metal complexes such

as their relatively strong absorption at *ca*. 450 nm, participation in single electron transfer (SET) processes, stable and long-lived excited-states as well as their ability to act as effective oxidants and reductants.[23,45]

Theoretical studies conducted by Bhand *et al*. have shown that these complexes adopt a low-spin $4d^6 5s^0$ electronic configuration with doubly occupied three d-orbitals.[58] The two unoccupied orbitals are responsible for the observed pseudo-octahedral geometry of the ligands around the metal ion.[58] Moreover, this study shows ruthenium non-bonding d-orbitals contribute significantly to the highest occupied molecular orbital (HOMO) of the complex. The lowest unoccupied molecular orbital (LUMO) is largely localised on the aromatic rings of the ligands and the transitions between these orbitals gives rise to the unique properties of these complexes (Figure 1.7).[58]

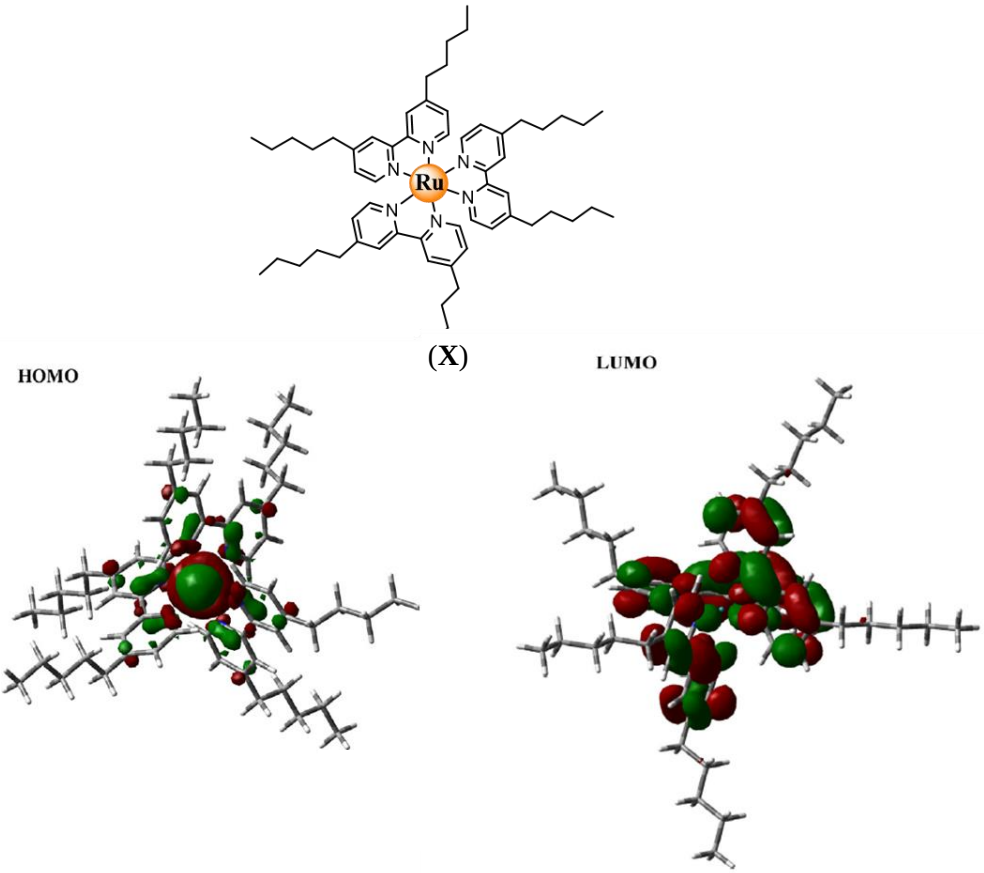

Figure 1.7 Representative frontier orbitals of a ruthenium(II) bipyridyl complex (**X**).[58]

Notably, these complexes are not catalytically active in their ground state, however, when exposed to visible-light, they generate highly reactive charge-transfer excited-states that are able to oxidise or reduce organic substrates *via* single electron transfer (SET) processes.[60] To

fully understand how this photocatalytic activity arises, we need to have a closer look into the mechanistic pathway that these complexes generally follow.

1.4.1 Mechanism of visible light-mediated catalytic processes

There are generally three reaction pathways followed by a photoredox catalyst upon photoexcitation with visible-light, namely *via* (i) electron transfer, (ii) atom transfer or, (iii) through the metal centre.[22,61] Pertinent to our study, we will focus on electron transfer, which involves the transfer of an electron between a substrate and a photoredox catalyst *via* an outer-sphere electron transfer mechanism. This then generates highly reactive radicals that can engage in organic reactions that were previously inaccessible under thermal control.[22,61]

The reaction mechanism for this electron transfer process involves three main steps, namely light absorption, MLCT excited states and quenching processes.[62] Upon excitation, an electron from the filled metal-centred t_{2g} orbitals of the photocatalyst is excited to the low-lying π^* orbital of the bipyridyl ligand (Scheme 1.2).[63] A redox-active excited-state *Ru(II) is then generated, which undergoes intersystem crossing (ISC) – a rapid conversion from a singlet excited-state to a lower-energy triplet excited-state *via* a non-radiative pathway, resulting in a relatively long-lived excited triplet state (^{3}MLCT).[60,64] The generated triplet excited-state can then interact with other organic molecules through quenching processes where it can act as either a reductant or an oxidant (Scheme 1.2).[60,61]

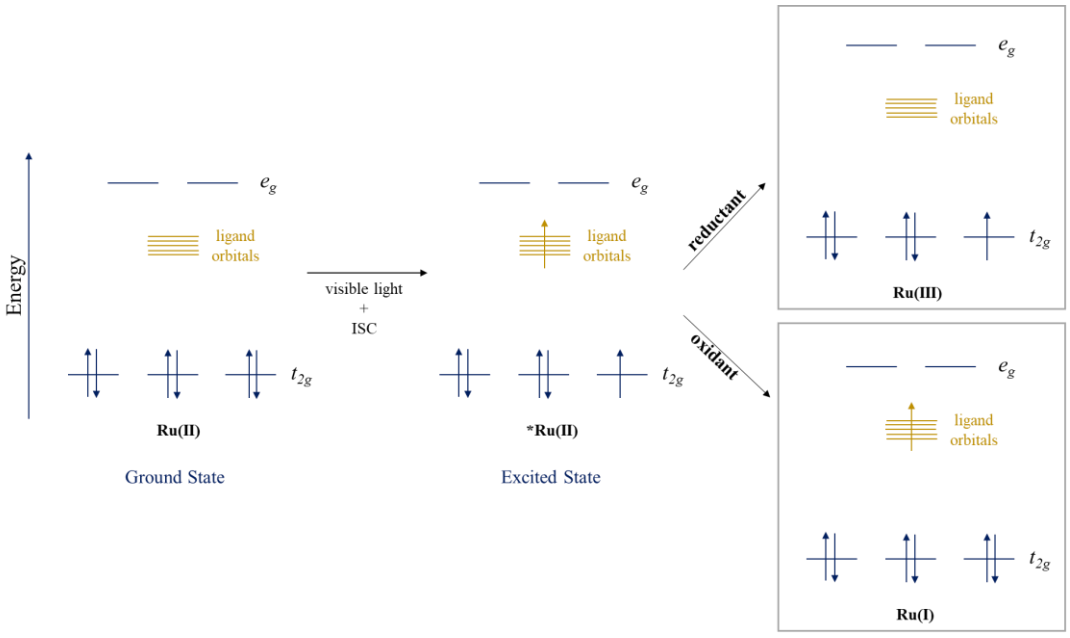

Scheme 1.2 Molecular orbital depiction of the photoexcitation of $[Ru(bpy)_3]^{2+}$.[60]

The pathways in which the excited-states of a photoredox catalyst are quenched are through oxidative or reductive quenching pathways (Scheme 1.3).[60,65] In oxidative quenching, the excited photocatalyst, $PCat^{*}$, reacts with an electron-accepting substrate to give an oxidised ground-state, $PCat^{+*}$.[65] The oxidised ground-state further reacts with a reductant to regenerate the photoredox catalyst.[65] Reductive quenching involves the reaction of the photoexcited catalyst, $PCat^{*}$, with an electron-rich donor to give a highly reactive radical and the reduced ground-state, $PCat^{*-}$, which can be oxidised to regenerate the catalyst.[65]

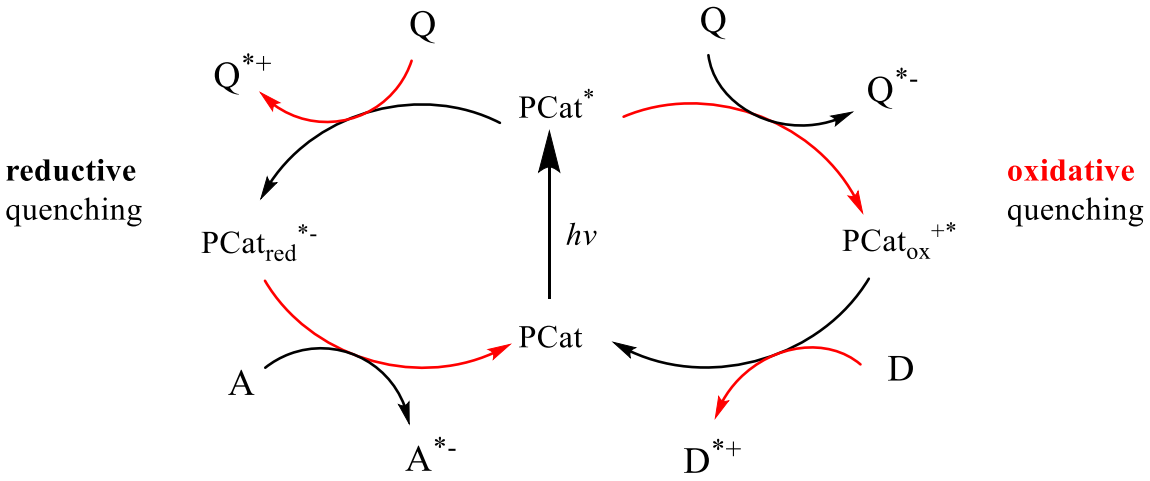

Scheme 1.3 General depiction of photoredox catalysis by reductive or oxidative quenching processes. PCat = photocatalyst, Q = quencher, D = donor, A = acceptor.[65]

1.4.2 Free-radical chemistry mediated by visible-light

The potential of photoredox catalysis for organic transformations arises from the ability of the photocatalyst to generate reactive open-shell radicals or radical ions.[14] These radicals are generated from stable and well-matched precursors under mild conditions of visible-light irradiation, as illustrated in Scheme 1.3 above.[14]

Radical chemistry has experienced remarkable developments over the last few decades, despite the field enduring a few drawbacks that have hindered its full recognition in chemistry.[66] To overcome these drawbacks, new advances are required to exploit the full potential of this field, playing a crucial role in many disciplines such as natural products, agriculture, synthesis of medicinal drugs and polymerisation.[67-70] Conventional methods of generating radical species often required harsh reaction conditions such as the use of initiators like tin(IV) derivatives or hydrogen donors, which are typically toxic, unstable to air, high-energy demanding and lack of chemoselectivity.[67,71] To avoid the toxicity associated with the abovementioned initiators,

hydrogen atom donors such as 1,4-cyclohexadiene or triethylsilane have been used with little success.[71]

The renewed interest of visible-light photoredox catalysis, stimulated a wide array of approaches to generate alkyl radicals from alkyl halides toward reactive intermediates for coupling reactions.[72] Photoredox catalysts have been shown to chemoselectively reduce activated carbon-halogen bonds under mild reaction conditions through irradiation by visible-light.[68] The use of these compounds therefore represents a breakthrough in fields such as photochemistry and free-radical chemistry.[68] This highlights the advantages of photoredox catalysis in radical chemistry with the possibility of extension to multinuclear systems that can potentially replace the overly used tin derivatives and trialkylboranes.[73]

1.5 Multinuclear visible-light photoredox catalysts

Several examples of multinuclear complexes that have been evaluated as potential photoredox catalysts have been reported, with applications in energy and electron transfer processes such as water oxidation and CO_2 reduction.[74,75] Multinuclear complexes provide multiple active sites, high reactivity, improved stability and have been demonstrated to overcome the poor durability of reported mononuclear catalysts.[76]

The challenges in CO_2 reduction are due to inherent molecular stability making this electrochemical transformation difficult as it requires a high reduction potential in order to activate the CO_2 for one-electron reduction.[77] To overcome this, a multi-electron transfer system may be introduced into the reduction of CO_2, achievable through the use of multinuclear photoredox catalysts.[77] The advantages of these multinuclear compounds arise from their ability to accelerate electron transfer leading to improved performance of the photocatalytic process.[77] This results in higher durability since the unstable excited or reduced states of the multinuclear units can be consumed more rapidly by the other subunit during the photocatalytic cycle.[78-80]

The improvement in activity exhibited by a multinuclear photoredox catalyst was demonstrated by Zhang *et al*. in the photocatalytic oxidation of water (Figure 1.8).[81] It was observed that the trinuclear catalyst displayed high activity towards water oxidation with a turnover number

(TON) that was approximately twice that of its binuclear analogue.[81] A similar trend was observed by Cancelliere *et al*. where a trinuclear Ru(II)-Re(I) supramolecular complex was evaluated as a photocatalyst for CO_2 reduction (Figure 1.8).[82]

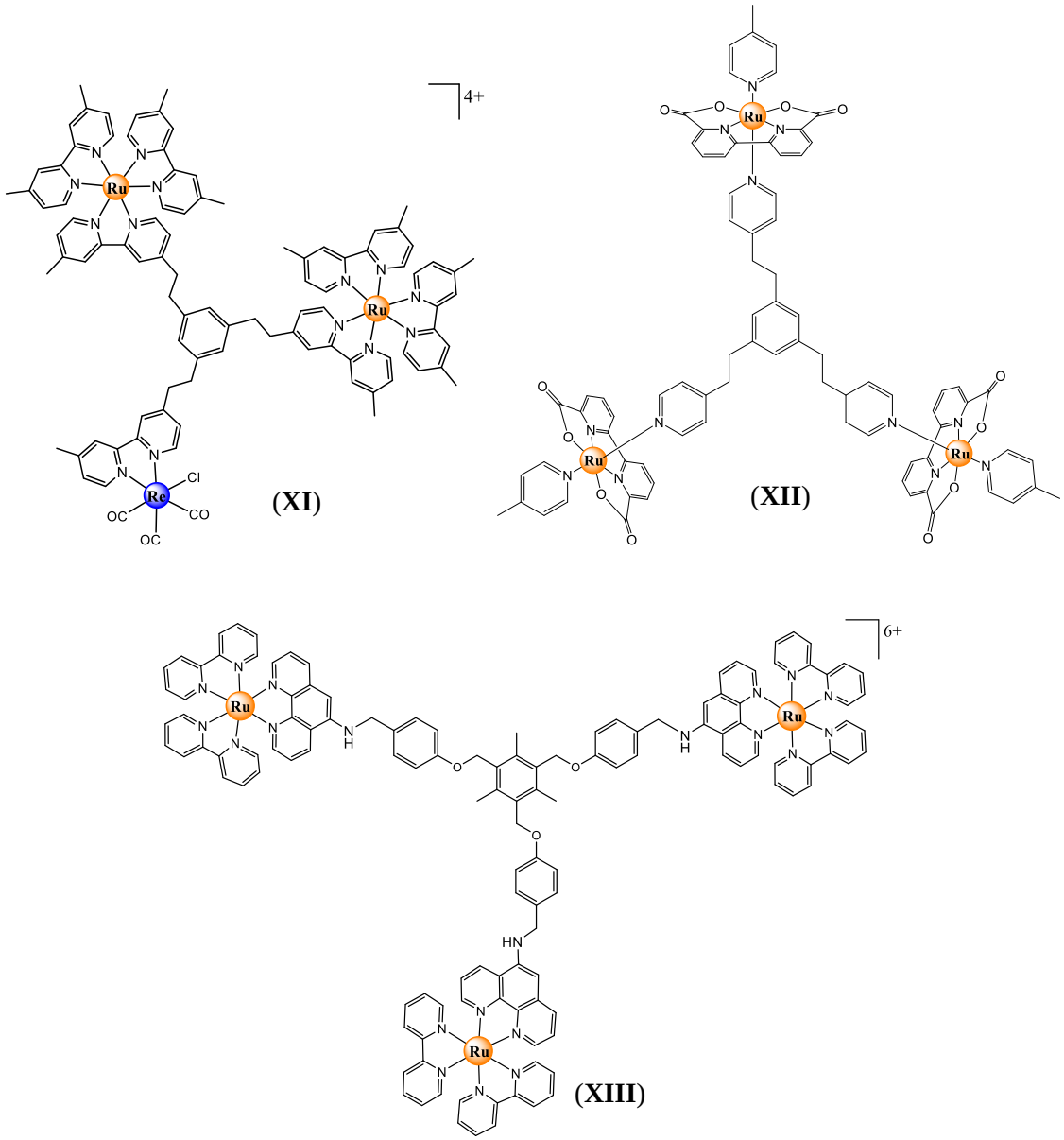

Figure 1.8 Selected examples of multinuclear ruthenium-based photoredox catalysts for CO_2 reduction (**XI**), water oxidation (**XII**) and, photophysical and redox properties evaluation (**XIII**).[81-83]

The increased catalytic activity of these multinuclear complexes is attributed to the enhanced redox properties inherent to the multinuclearity of the photocatalyst unit contained within a single macromolecule.[83]

1.6 Photoredox catalysis in synthetic organic chemistry: olefin hydrofunctionalisation

An important transformation in organic synthesis is the addition to alkenes *via* alkene hydrofunctionalisation reactions, which provides a direct method for the synthesis of some of the most essential commodities and fine chemicals containing carbon-heteroatom bonds.[84,85] The selective anti-Markovnikov addition of an acid (H−X, where X = OR, SR, NR_2 etc.) to alkenes is key in the formation of carbon-heteroatom bonds but this reaction has proven to be challenging in the field of catalysis.[84,86]

Transition metal-based catalytic platforms have been designed to address the challenges associated with anti-Markovnikov addition reactions, with notable success demonstrated by Hartwig and Buchwald for the hydroamination reaction of olefins.[87,88] Although efficient metal-based catalytic systems have been developed for the construction of carbon-heteroatom bonds, most of these reactions focused on the formation of C−O, C−N, C−P as well as C−B bonds (Figure 1.9).[89,90] The construction of compounds containing C−S bonds were excluded from this rapidly expanding research area as they were considered to deactivate active catalytic species.[91]

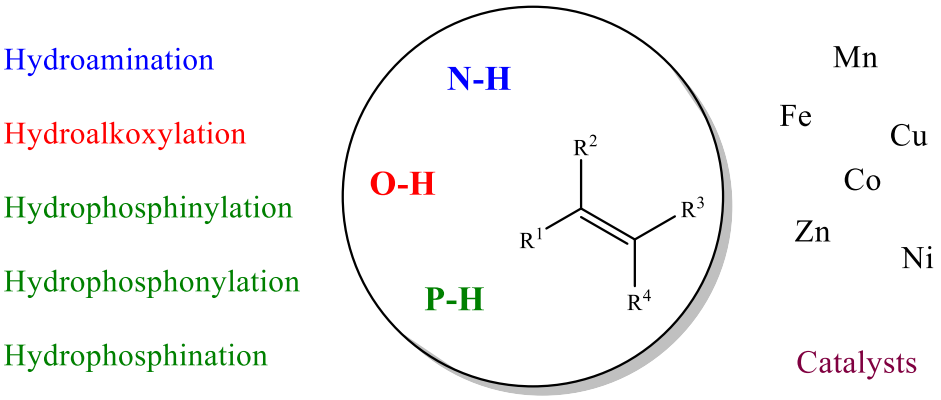

Figure 1.9 Examples of metal-catalysed alkene hydrofunctionalisation reactions.[90]

Sulfur-containing compounds are extensively used as building blocks for various precursors with applications in the pharmaceutical industry, material science and food chemistry.[92,93] Traditional methods for the preparation of these compounds involve nucleophilic substitution at carbon-centred electrophiles of various sulfanyl precursors such as thiols, followed by sulfide oxidation, a method that is not compatible with a broad scope of substrates.[94] Furthermore, Pd-catalysed C−S bond formation – a common catalytic system for the construction of C−O and C−N bonds, results in the deactivation of metal catalysts *via* the

strong coordinating properties of these sulfur-containing substrates.[92]

To overcome the limitations of this hydrofunctionalisation reaction, research has been undertaken to explore the use of visible light-induced transformations that allow these reactions to proceed under milder conditions without the need for stoichiometric oxidants.[95] The success of visible light-mediated hydrofunctionalisation reactions was demonstrated by Romero *et al*. where a well-defined redox cycle was developed for alkene hydrofunctionalisation.[96] This resulted in complete anti-Markovnikov selectivity utilising catalytic amounts of an organic dye photooxidant.[96]

The main disadvantage of an organophotoredox catalyst is the difficulty in tenability which tends to limit the substrate scope. Additionally, a hydrogen atom donor is required for the photocatalytic process to proceed successfully.[96] In light of this, further research in the design of metal-based photoredox catalysts for C−S bond construction is ongoing.

1.7 Rationale for the current study

The increasing need for the development of catalytic systems driven by sustainable energy sources continue to motivate the development of catalytic processes making use of natural light energy to initiate chemical reactions.[97,98] The use of polynuclear complexes is attracting significant attention in many fields, offering several advantages over mononuclear analogues.[99] In the context of this project, the presence of several photoactive centres can lead to a multi-electron transfer in a single step, and improved reactivity and stability.

Photoredox catalysis has the ability to utilise light energy to drive chemical reactions leading to important progress in organic synthesis.[100] It provides access to highly reactive intermediates under very mild conditions of visible-light at room temperature, thus making the process a more sustainable approach compared to photochemical reactions that utilise specialised equipment and high-energy UV-light.[101] There are however, limitations in the scope of substrates that can undergo photocatalytic transformation with the prototypical $[Ru(bpy)_3]^{2+}$ catalyst.[102] Moreover, there are only a few examples from the literature that make use of multinuclear photoredox catalysts for the hydrothiolation reaction of olefins.[43,102] It is against this backdrop that ligand-modified photoredox catalysts and their multinuclear analogues were

explored with the aims of improving the efficiency of the complexes as photocatalysts in conjunction with the greater stability afforded by the multinuclear system.

The design of the photoredox catalyst included a ruthenium metal, 2,2'-bipyridine that was functionalised with various electron-withdrawing and electron-donating substituents (Figure 1.10). The motivation behind the use of the precious platinum-group metal (PGM) is that it is readily available in South Africa (beneficiation of natural resources), imparts stability on the photocatalyst, and the excited-state deactivation of ruthenium-bearing complexes is slow in comparison to first-row transition metal photocatalysts.[103-105] This enhanced stability arises from the larger d-orbital splitting of ruthenium bipyridyl complexes resulting in the e_g orbitals of the complex to be less accessible, which is common for second- and third-row transition metal complexes.[60]

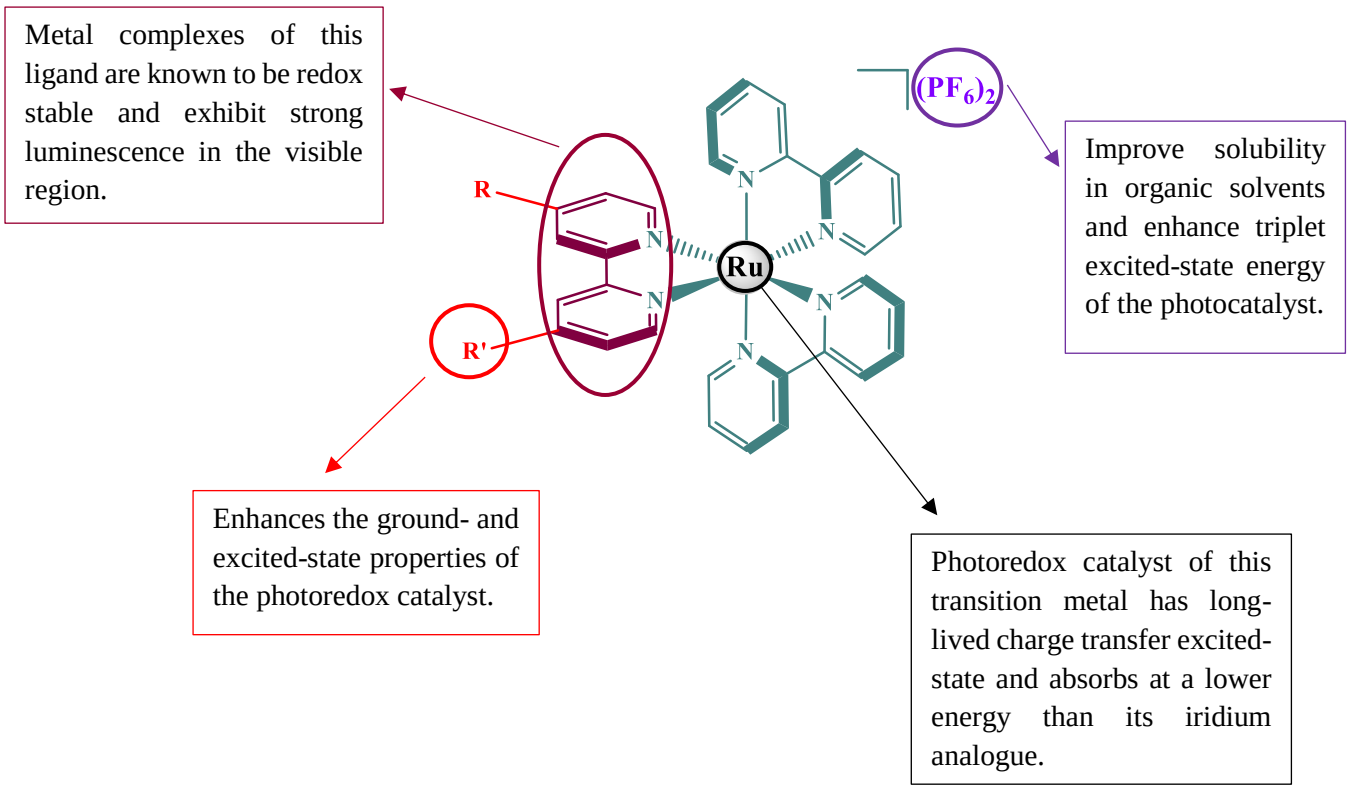

Figure 1.10 Design of ruthenium(II) complexes for photoredox catalysis.

Furthermore, 2,2'-bipyridine has been shown to exhibit robust redox stability and it can be functionalised at various positions of the aromatic rings.[106,107] The incorporation of substituents at the 4,4'-position of the N^N ligand was aimed at fine-tuning the LUMO orbitals of the

ligands and thus enhancing the ground- and excited-state photophysical and redox properties of the complex as a photoredox catalyst.[108] Lastly, the non-coordinating hexafluorophosphate counter-ion may improve solubility of the photocatalyst in organic solvents and possibly improve the reactivity of the photocatalyst in the hydrothiolation reaction of olefins (Figure 1.10).[9]

This design was extended to trinuclear analogues in efforts to improve the efficiencies of the complexes as photoredox catalysts. All complexes were evaluated as photoredox catalysts in the alkene hydrothiolation reaction to produce various thioethers, which are important building blocks in materials and biomedical sciences.[92]

1.8 Aims and objectives

1.8.1 General aims

The aim of this project was to synthesise and characterise small molecule and macromolecular ruthenium polypyridyl complexes that were used as photoredox catalysts for thiol-ene coupling reactions.

1.8.2 Specific objectives

The specific objectives of the project were:

(a) To synthesise the aldehyde-functionalised bipyridyl ligand (**1**) (Scheme 1.4).

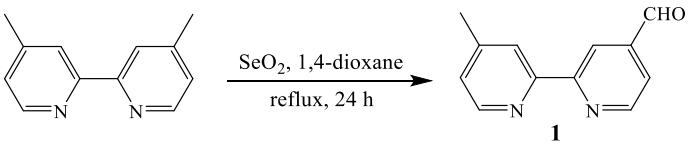

1

Scheme 1.4 Outline for the synthesis of monomeric bipyridyl ligand precursor (**1**).

(b) To synthesise monomeric amine- and imine-functionalised bipyridyl ligands (**2, 3**) (Scheme 1.5).

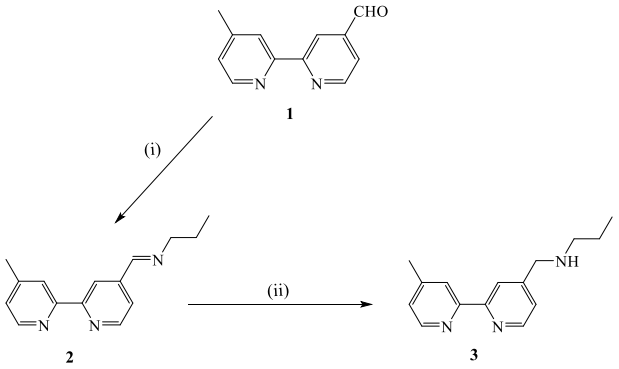

Scheme 1.5 Outline for the synthesis of monomeric bipyridyl ligands (**2, 3**), following reaction conditions (i) 1 mol eq. of (**1**), 1 mol eq. *n*-propylamine, CH_2Cl_2, $MgSO_4$, rt, 24 h and, (ii) 2.6 eq. $NaBH_4$, CH_3OH, rt, 24 h.

(c) To synthesise trimeric amine- and imine-functionalised bipyridyl ligands (**4, 5**) (Scheme 1.6).

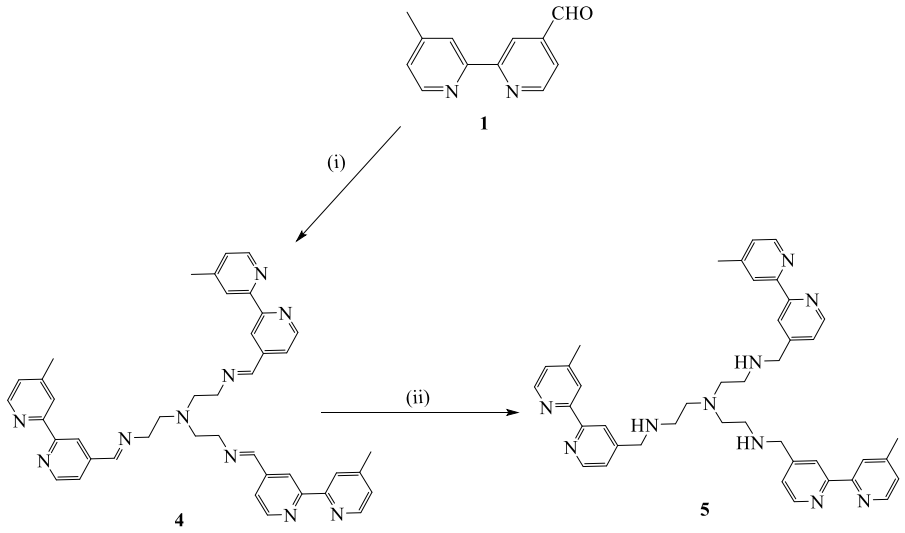

Scheme 1.6 Outline for the synthesis of trimeric bipyridyl ligands (**4, 5**), following reaction conditions (i) 3 mol eq. of (**1**), 1 mol eq. tris(2-aminoethyl)amine, CH_2Cl_2, $MgSO_4$, rt, 48 h and, (ii) 4.5 eq. $NaBH_4$, CH_3OH, rt, 48 h.

(d) To synthesise mononuclear ruthenium(II) bipyridyl complexes (**6, 7**) (Scheme 1.7).

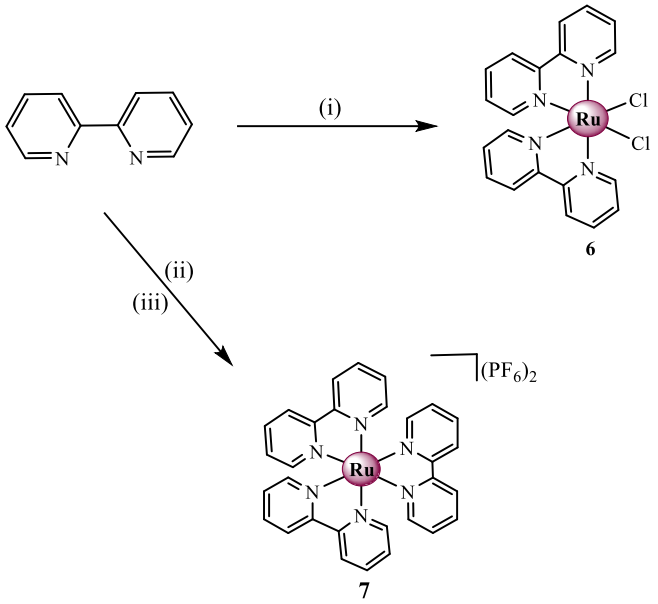

Scheme 1.7 Outline for the synthesis of mononuclear Ru(II) bipyridyl complexes (**6, 7**), following reaction conditions (i) 2 mol eq. of 2,2'-bipyridine, $RuCl_3.xH_2O$, $(CH_3)_2NCH$, LiCl, reflux, 24 h, (ii) 3 mol eq. of 2,2'-bipyridine, $RuCl_3.xH_2O$, $(CH_3)_2NCH$, reflux, 24 h and, (iii) 2.5 mol eq. NH_4PF_6 (aq.), rt, 30 min.

(e) To synthesise mononuclear ruthenium(II) heteroleptic complexes (**8-10**) (Scheme 1.8).

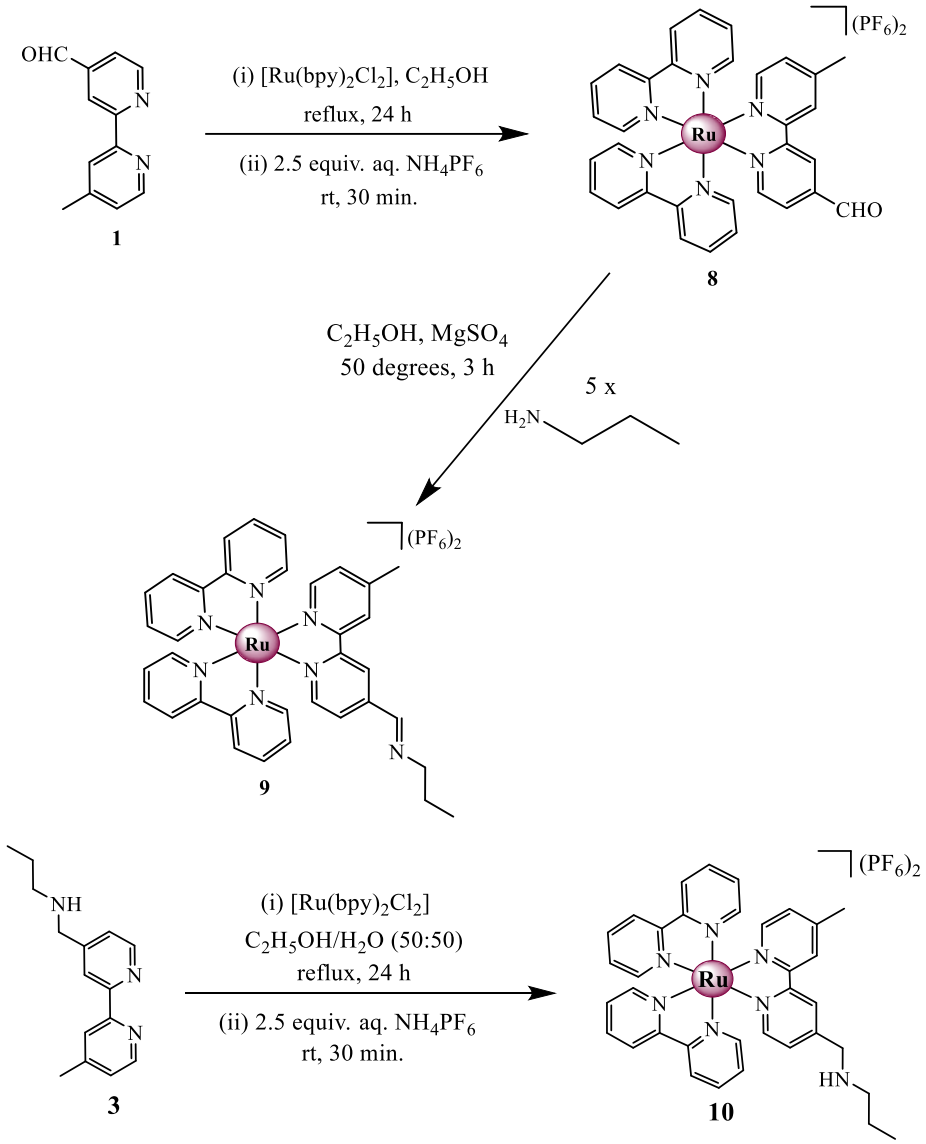

Scheme 1.8 Outline for the synthesis of mononuclear Ru(II) bipyridyl complexes (**6-10**).

(f) To synthesise trinuclear ruthenium bipyridyl complexes (**11**, **12**) (Scheme 1.9).

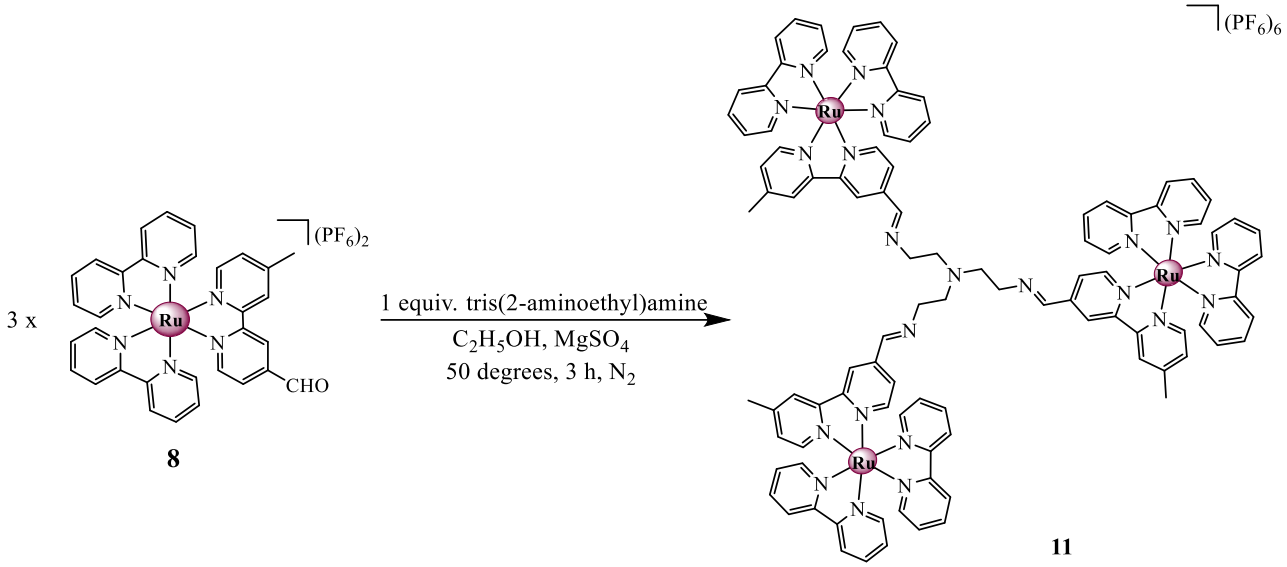

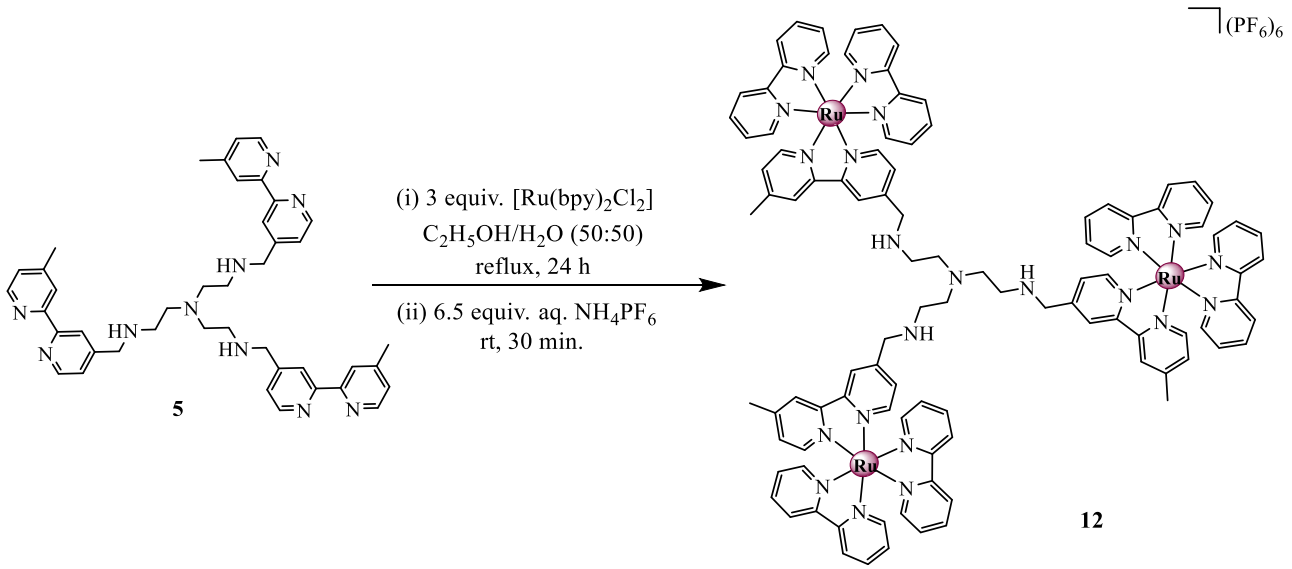

Scheme 1.9 Outline for the synthesis of trinuclear ruthenium bipyridyl heteroleptic complexes (**11, 12**).

(g) To characterise the synthesised compounds using spectroscopic and analytical techniques including ^{1}H NMR, $^{13}C\{^{1}H\}$ NMR, infrared spectroscopy and mass spectrometry.

(h) To conduct electrochemical, electronic absorption and emission studies for all the synthesised complexes.

(i) To evaluate complexes as photoredox catalysts for radical thiol-ene reactions followed by isolation and quantification of product by column chromatography.

1.9 References

1. R. Noyori, *Nat. Chem.*, 2009, **1**, 5-6.
2. S. H. Leenders, R. Gramage-Doria, B. de Bruin, and J. N. Reek, *Chem. Soc. Rev.*, 2015, **44**, 433-448.
3. S. Atalay and G. Ersöz, Novel Catalysts in Advanced Oxidation of Organic Pollutants, *Springer, Cham*., 2016, 7-22.
4. C. C. Johansson Seechurn, M. O. Kitching, T. J. Colacot and V. Snieckus, *Angew. Chem. Int. Ed.*, 2012, **51**, 5062-5085.
5. P. Barbaro, C. Bianchini, G. Giambastiani and S. L. Parisel, *Coord. Chem. Rev.*, 2004, **248**, 2131-2150.
6. W. M. Cheng and R. Shang, *ACS Catal.*, 2020, **10**, 9170-9196.
7. L. C. Matsinha, S. Siangwata, G. S. Smith and B. C. E. Makhubela, *Catal. Rev.*, 2019, **61**, 111-133.
8. D. M. Hood, R. A. Johnson, A. E. Carpenter, J. M. Younker, D. J. Vinyard and G. G. Stanley, *Science*, 2020, **367**, 542-548.
9. E. P. Farney, S. J. Chapman, W. B. Swords, M. D. Torelli, R. J. Hamers and T. P. Yoon, *J. Am. Chem. Soc.*, 2019, **141**, 6385-6391.
10. M. K. Sahoo and E. Balaraman, *Green Chem.*, 2019, **21**, 2119-2128.
11. M. Lancaster, Green Chemistry: An Introductory Text. *Royal Society of Chemistry*, 2020.
12. A. Albini and M. Fagnoni, *ChemSusChem*, 2008, **1**, 63-66.
13. D. M. Schultz and T. P. Yoon, *Science*, 2014, **343**, 1239176.
14. T. P. Yoon, M. A. Ischay and J. Du, *Nat. Chem.*, 2010, **2**, 527.
15. D. A. Nicewicz and D. W. MacMillan, *Science*, 2008, **322**, 77-80.
16. A. Kudo and Y. Miseki, *Chem. Soc. Rev.*, 2009, **38**, 253-278.
17. N. Hoffmann, *Chem. Rev.*, 2008, **108**, 1052-1103.
18. N. Kaur, *Synth. Commun.*, 2018, **48**, 1259-1284.
19. Q. Q. Zhou, Y. Q. Zou, L. Q. Lu and W. J. Xiao, *Angew. Chem. Int. Ed.*, 2019, **58**, 1586-1604.
20. J. Xuan and W. J. Xiao, *Angew. Chem. Int. Ed.*, 2012, **51**, 6828-6838.
21. J. M. Narayanam, J. W. Tucker and C. R. Stephenson, *J. Am. Chem. Soc.*, 2009, **131**, 8756-8757.
22. M. H. Shaw, J. Twilton and D. W. MacMillan, *J. Org. Chem.*, 2016, **81**, 6898-6926.

23. W. G. Jia, M. X. Cheng, L. L. Gao, S. M. Tan, C. Wang, X. Liu and R. Lee, *Dalton Trans.*, 2019, **48**, 9949-9953.
24. J. K. McCusker, *Science*, 2019, **363**, 484-488.
25. X. Wu, C. Meng, X. Yuan, X. Jia, X. Qian and J. Ye, *Chem. Commun.*, 2015, **51**, 11864-11867.
26. S. Sato, T. Arai, T. Morikawa, K. Uemura, T. M. Suzuki, H. Tanaka and T. Kajino, *J. Am. Chem. Soc.*, 2011, **133**, 15240-15243.
27. S. Sato, T. Morikawa, S. Saeki, T. Kajino and T. Motohiro, *Angew. Chem. Int. Ed.*, 2010, **49**, 5101-5105.
28. B. M. Hockin, C. Li, N. Robertson and E. Zysman-Colman, *Catal. Sci. Technol.*, 2019, 9, 889-915.
29. A. U. Meyer, T. Slanina, C. J. Yao and B. König, *ACS Catal.*, 2016, **6**, 369-375.
30. A. Gualandi, M. Marchini, L. Mengozzi, M. Natali, M. Lucarini, P. Ceroni and P. G. Cozzi, *ACS Catal.*, 2015, **5**, 5927-5931.
31. M. Stevenson, M. P. Shores and E. M. Ferreira, *Angew. Chem. Int. Ed.*, 2015, **54**, 6506-6510.
32. M. E. Weiss, L. M. Kreis, A. Lauber and E. M. Carreira, *Angew. Chem. Int. Ed.*, 2011, **50**, 11125-11128.
33. B. J. Shields, B. Kudisch, G. D. Scholes and A. G. Doyle, *J. Am. Chem. Soc.*, 2018, **140**, 3035-3039.
34. S. Ferrere and B. A. Gregg, *J. Am. Chem. Soc.*, 1998, **120**, 843-844.
35. A. Sagadevan and K. C. Hwang, *Adv. Synth. Catal.*, 2012, **354**, 3421-3427.
36. R. Giri, A. Brusoe, K. Troshin, J. Y. Wang, M. Font and J. F. Hartwig, *J. Am. Chem. Soc.*, 2018, **140**, 793-806.
37. C. Le, T. Q. Chen, T. Liang, P. Zhang and D. W. MacMillan, *Science*, 2018, **360**, 1010-1014.
38. S. Engl and O. Reiser, *ACS Catal.*, 2020, **10**, 9899-9906.
39. D. Kurandina, M. Parasram and V. Gevorgyan, *Angew. Chem. Int. Ed.*, 2017, **56**, 14212-14216.
40. D. C. Fabry, M. A. Ronge, J. Zoller and M. Rueping, *Angew. Chem. Int. Ed.*, 2015, **54**, 2801-2805.
41. H. Huo, C. Wang, K. Harms and E. Meggers, *J. Am. Chem. Soc.*, 2015, **137**, 9551-9554.

42. A. Gualandi, E. Matteucci, F. Monti, A. Baschieri, N. Armaroli, L. Sambri and P. G. Cozzi, *Chem. Sci.*, 2017, **8**, 1613-1620.
43. E. L. Tyson, M. S. Ament and T. P. Yoon, *J. Org. Chem.*, 2013, **78**, 2046-2050.
44. M. Pirtsch, S. Paria, T. Matsuno, H. Isobe and O. Reiser, *Chem.–Eur. J.*, 2012, **18**, 7336-7340.
45. T. C. Motley, L. Troian-Gautier, M. K. Brennaman and G. J. Meyer, *Inorg. Chem.*, 2017, **56**, 13579-13592.
46. T. Mede, M. Jäger and U. S. Schubert, *Chem. Soc. Rev.*, 2018, **47**, 7577-7627.
47. D. M. Hedstrand, W. H. Kruizinga and R. M. Kellogg, *Tetrahedron Lett.*, 1978, **19**, 1255-1258.
48. T. J. Van Bergen, D. M. Hedstrand, W. H. Kruizinga and R. M. Kellogg, *J. Org. Chem.*, 1979, **44**, 4953-4962.
49. H. Cano-Yelo and A. Deronzier, *Tetrahedron Lett.*, 1984, **25**, 5517-5520.
50. H. Cano-Yelo and A. Deronzier, *J. Photochem.*, 1987, **37**, 315-321.
51. J. J. Li, Name Reactions: A Collection of Detailed Mechanisms and Synthetic Applications, *Springer Science & Business Media*, 4th Ed., 2010.
52. R. M. Elofson and F. F. Gadallah, *J. Org. Chem.*, 1971, **36**, 1769-1771.
53. J. M. Narayanam and C. R. Stephenson, *Chem. Soc. Rev.*, 2011, **40**, 102-113.
54. M. A. Ischay, M. E. Anzovino, J. Du and T. P. Yoon, *J. Am. Chem. Soc.*, 2008, **130**, 12886-12887.
55. A. G. Condie, J. C. González-Gómez and C. R. Stephenson, *J. Am. Chem. Soc.*, 2010, **132**, 1464-1465.
56. D. A. Nagib, M. E. Scott and D. W. MacMillan, *J. Am. Chem. Soc.*, 2009, **131**, 10875-10877.
57. P. V. Pham, D. A. Nagib and D. W. MacMillan, *Angew. Chem. Int. Ed.*, 2011, **50**, 6119-6122.
58. S. Bhand, D. N. Lande, E. Pereira, S. P. Gejji, T. Weyhermüller, D. Chakravarty and S. Salunke-Gawali, *Polyhedron*, 2019, **164**, 96-107.
59. M. V. Bobo, A. Paul, A. J. Robb, A. M. Arcidiacono, M. D. Smith, K. Hanson and A. K. Vannucci, *Inorg. Chem.*, 2020, **59**, 6351-6358.
60. F. Muniz-Miranda, L. De Bruecker, A. De Vos, F. Vanden Bussche, C. V. Stevens, P. Van Der Voort and V. Van Speybroeck, *J. Phys. Chem. A*, 2019, **123**, 6854-6867.

61. Y. Xi, H. Yi and A. Lei, *Org. Biomol. Chem.*, 2013, **11**, 2387-2403
62. M. Fagnoni, D. Dondi, D. Ravelli and A. Albini, *Chem. Rev.*, 2007, **107**, 2725-2756.
63. K. Kalyanasundaram, *Coord. Chem. Rev.*, 1982, **46**, 159-244.
64. D. Staveness, I. Bosque and C. R. Stephenson, *Acc. Chem. Res.*, 2016, **49**, 2295-2306.
65. K. Zeitler, *Angew. Chem. Int. Ed.*, 2009, **48**, 9785-9789.
66. C. R. Stephenson, T. P. Yoon and D. W. MacMillan, Visible Light Photocatalysis in Organic Chemistry, *John Wiley & Sons*, 1st Ed., 2018.
67. B. Schweitzer-Chaput, M. A. Horwitz, E. de Pedro Beato and P. Melchiorre, *Nat. Chem.*, 2019, **11**, 129-135.
68. J. W. Tucker, J. D. Nguyen, J. M. Narayanam, S. W. Krabbe and C. R. Stephenson, *Chem. Commun.*, 2010, 46, 4985-4987.
69. S. K. Pagire, T. Föll and O. Reiser, *Acc. Chem. Res.*, 2020, **53**, 782-791.
70. L. Breloy, V. Brezová, A. Blacha-Grzechnik, M. Presset, M. S. Yildirim, I. Yilmaz and D. L. Versace, *Macromolecules*, 2019, **53**, 112-124.
71. J. D. Nguyen, E. M. D'amato, J. M. Narayanam and C. R. Stephenson, *Nat. Chem.*, 2012, **4**, 854.
72. S. Roslin and L. R. Odell, *Eur. J. Org. Chem.*, 2017, **2017**, 1993-2007.
73. P. A. Baguley and J. C. Walton, *Angew. Chem. Int. Ed.*, 1998, **37**, 3072-3082.
74. F. Cheng, C. He and S. Yu, *Transit. Met. Chem.*, 2017, **42**, 395-403.
75. Y. Jiang, F. Li, B. Zhang, X. Li, X. Wang, F. Huang and L. Sun, *Angew. Chem. Int. Ed.*, 2013, **125**, 3482-3485.
76. M. Sun, C. Wang, C. Y. Sun, M. Zhang, X. L. Wang and Z. M. Su, *J. Catal.*, 2020, **385**, 70-75.
77. H. Takeda and O. Ishitani, *Coord. Chem. Rev.*, 2010, **254**, 346-354.
78. Y. Tamaki and O. Ishitani, *ACS Catal.*, 2017, **7**, 3394-3409.
79. K. Kozawa, A. Inagaki and M. Akita, *Chem. Lett.*, 2014, **43**, 290-292.
80. R. O. Reithmeier, S. Meister, A. Siebel and B. Rieger, *Dalton Trans.*, 2015, **44**, 6466-6472.
81. L. L. Zhang, Y. Gao, Z. Liu, X. Ding, Z. Yu and L. C. Sun, *Dalton Trans.*, 2016, **45**, 3814-3819.
82. A. M. Cancelliere, F. Puntoriero, S. Serroni, S. Campagna, Y. Tamaki, D. Saito and O. Ishitani, *Chem. Sci.*, 2020, **11**, 1556-1563.
83. C. He, S. Yu, S. Ma and F. Cheng, *Transit. Met. Chem.*, 2019, **44**, 515-524.

84. D. A. Nicewicz and D. S. Hamilton, *Synlett*, 2014, **25**, 1191.
85. X. L. Zhou, F. Yang, H. L. Sun, Y. N. Yin, W. T. Ye and R. Zhu, *J. Am. Chem. Soc.*, 2019, **141**, 7250-7255.
86. K. A. Margrey and D. A. Nicewicz, *Acc. Chem. Res.*, 2016, **49**, 1997-2006.
87. M. Utsunomiya, R. Kuwano, M. Kawatsura and J. F. Hartwig, *J. Am. Chem. Soc.*, 2003, **125**, 5608-5609.
88. S. Zhu, N. Niljianskul and S. L. Buchwald, *J. Am. Chem. Soc.*, 2013, **135**, 15746-15749.
89. N. V. Orlov, *ChemistryOpen*, 2015, **4**, 682-697.
90. S. Bezzenine-Lafollée, R. Gil, D. Prim and J. Hannedouche, *Molecules*, 2017, **22**, 1901.
91. M. Beller, J. Seayad, A. Tillack and H. Jiao, *Angew. Chem. Int. Ed.*, 2004, **43**, 3368-3398.
92. Z. Qiao, J. Wei and X. Jiang, *Org. Lett.*, 2014, **16**, 1212-1215.
93. S. V. Ley and A. W. Thomas, *Angew. Chem. Int. Ed.*, 2003, **42**, 5400-5449.
94. N. W. Liu, S. Liang and G. Manolikakes, *Synthesis*, 2016, **48**, 1939-1973.
95. K. Luo, Y. Z. Chen, W. C. Yang, J. Zhu and L. Wu, *Org. Lett.*, 2016, **18**, 452-455.
96. N. A. Romero and D. A. Nicewicz, *J. Am. Chem. Soc.*, 2014, **136**, 17024-17035.
97. P. T. Smith, E. M. Nichols, Z. Cao and C. J. Chang, *Acc. Chem. Res.*, 2020, **53**, 575-587.
98. M. Waki, S. Shirai, K. I. Yamanaka, Y. Maegawa and S. Inagaki, *RSC Adv.*, 2020, **10**, 13960-13967.
99. A. Welsh, L. I. Rylands, V. B. Arion, S. Prince and G. S. Smith, *Dalton Trans.*, 2020, **49**, 1143-1156.
100. F. Glaser and O. S. Wenger, *Coord. Chem. Rev*., 2020, **405**, 213129.
101. C. K. Prier, D. A. Rankic and D. W. MacMillan, *Chem. Rev*., 2013, **113**, 5322-5363.
102. P. A. Anderson, G. F. Strouse, J. A. Treadway, F. R. Keene and T. J. Meyer, *Inorg. Chem.*, 1994, **33**, 3863-3864.
103. F. Crundwell, M. Moats, V. Ramachandran, T. Robinson and W. G. Davenport, Extractive Metallurgy of Nickel, Cobalt and Platinum Group Metals. *Elsevier*. 1st Ed., 2011.
104. A. Obuchi, A. Ohi, M. Nakamura, A. Ogata, K. Mizuno and H. Ohuchi, *Appl. Catal. B*, 1993, **2**, 71-80.
105. C. B. Larsen and O. S. Wenger, *Chem.–Eur. J*., 2018, **24**, 2039-2058.

106. Z. Wang, Y. Wang, Y. Xu, J. Li, X. Ke, C. Jia and Q. Duan, *Adv. Opt. Mater.*, 2020, **105**, 109876.
107. C. Kaes, A. Katz and M. W. Hosseini, *Chem. Rev.*, 2000, **100**, 3553-3590.
108. D. L. Ashford, M. K. Brennaman, R. J. Brown, S. Keinan, J. J. Concepcion, J. M. Papanikolas and T. J. Meyer, *Inorg. Chem.*, 2015, **54**, 460-469.

Chapter 2

Synthesis and characterisation of mononuclear and multinuclear ruthenium complexes

2.1 Introduction

Over the past decades, metal polypyridyl complexes based on the second and third row transition metals have contributed significantly to the development of transition metal electrochemistry, photochemistry electron, and energy transfer studies.[1,2] As discussed in Chapter 1 of this thesis, the commonly used metal complex for these studies is the dicationic tris(2,2'-bipyridine)ruthenium(II) complex composed of a second row metal and a strong, chelating bidentate ligand binding to the metal ion through the pyridyl nitrogen atoms. Despite the extensive range of applications of the tris(2,2'-bipyridine)ruthenium(II) complex in various fields, there are still limitations in the scope of substrates that can undergo photocatalytic transformations with the homoleptic $[Ru(bpy)_3]^{2+}$ complex.[3] Therefore, research focus needs to be directed on developing heteroleptic and modified derivatives in order to enhance the properties and performance of these complexes as photocatalysts for a broad range of reactions.

The distinct relationship between the structural features and redox properties of the photocatalyst allows for the design of analogous complexes by modification of the ligand and the metal of choice.[4] Among the types of polypyridyl ligands used, 2,2'-bipyridine has become the ideal candidate for the design of transition metal photocatalysts since these ligands are readily functionalised through the various sites of the aromatic rings.[5,6] Introducing electron-withdrawing or electron-donating substituents at the 4 or/and 4' positions of the bipyridine ligands results in heteroleptic complexes with altered ground- and excited-state properties such as the quantum yield, excited-state lifetime, redox potentials and wavelength of emission maximum of the resulting complexes.[7,8]

Attesting to this, Waki *et al*. reported on an efficient photocatalytic system for water oxidation where the photochemical properties of ruthenium complexes were tuned through the incorporation of electron-donating and electron-withdrawing functionalities on the bipyridine ligands (Figure 2.1, **I-IV**).[9] The experimental findings from this study revealed the advantages of incorporating substituents on the bipyridine, where the photocatalyst containing electron-

withdrawing substituents (Figure 2.1, **III**) resulted in a 4-fold increase in turnover numbers, toward water oxidation, relative to the unmodified analogue.[9]

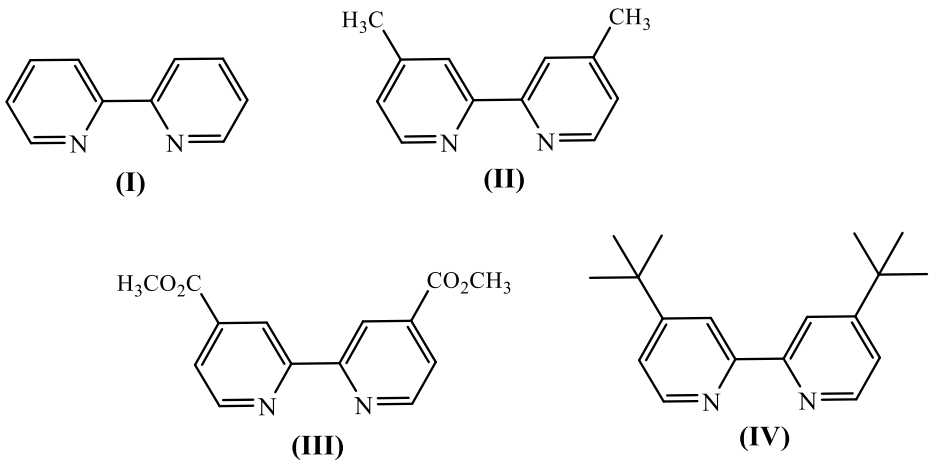

Figure 2.1 Functionalised bipyridyl ligands used in the preparation of ruthenium(II) complexes as photocatalysts for water oxidation.[9]

This enhanced activity was attributed to variations in the π^* levels of the bipyridyl ligands, affected by the presence of the different substituents on the ligands.[9] It is evident that functionalisation of the bipyridine ligands has a direct effect on the redox and photophysical properties of transition metal complexes.

To illustrate the changes in photophysical properties, Figure 2.2 depicts how the energy levels are shifted by changing or modifying the ligands on the ruthenium(II) metal complexes. From the figure it is observed that the separation between the lowest ligand π^* and ruthenium t_{2g} orbitals gives the energy of the MLCT transition.[2,10] Tuning the ligand by introducing an electron-withdrawing group, for instance, decreases the relative energy of the π^* orbital of the ligand thus reducing the MLCT energy gap of the photocatalyst (Figure 2.2).[9] Conversely, complexes with ligands bearing electron-donating substituents are expected to increase the electron density around the metal centre leading to an increase in the reductive power of the complex.

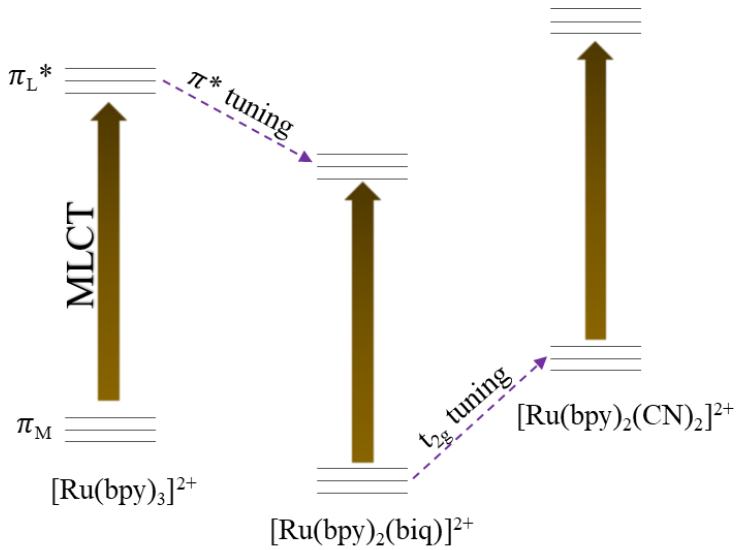

Figure 2.2 Selected example of the effects of ligand modification on the HOMO (t_{2g}) and LUMO (π^*) energy levels of Ru^{II}-type complexes.[2]

Furthermore, ligand modifications have been demonstrated to induce changes on the excited-state redox potentials of the Ru^{II}-type complexes.[11] Therefore, the excited-state acting as a reductant ($Ru^{3+/2+*}$) and oxidant ($Ru^{2+*/+}$) for the synthesised complexes will be examined and determined using Equations 2.1 and 2.2.[12] The free energies of the excited-state above the ground-state, ΔG_{ES}, will be determined from the emission spectra obtained for the complexes and this will be explained later in this Chapter.

$$E^{\circ\prime}(Ru^{2+*/+}) = E^{\circ\prime}(Ru^{2+/+}) + \Delta G_{ES} \quad (2.1)$$

$$E^{\circ\prime}(Ru^{3+/2+*}) = E^{\circ\prime}(Ru^{3+/2+}) - \Delta G_{ES} \quad (2.2)$$

The design and synthesis of ligand-modified complexes will be extended to multinuclear systems. The multinuclearity of ruthenium(II) bipyridyl complexes has been shown to provide multiple active sites, high reactivity, improved stability and has the ability to overcome the poor durability of reported mononuclear catalysts.[13] The improvement in photocatalytic activity exhibited by these multinuclear photoredox catalysts is attributed to the enhanced photophysical and redox properties contained within a single macromolecule.[14] Therefore, herein we report on the synthesis and characterisation of mononuclear complexes and their multinuclear analogues.

The synthesis of heteroleptic ruthenium(II) complexes containing *N*,*N*-ligands, are undertaken *via* several routes. The previously reported methods describe preparation of ruthenium(II) complexes from the *cis*-dichlorobis(2,2'-bipyridine)ruthenium(II) complex precursor.[15,16] The ruthenium(II) complexes in this study are synthesised using $[Ru(bpy)_2Cl_2]$, where bpy = bipyridine, as a precursor in the preparation of the heteroleptic mononuclear and trinuclear ruthenium(II) complexes. The complexes are coordinated by bipyridyl ligands containing relatively electron-withdrawing and electron-donating groups at the 4 or/and 4' position of one of the bipyridyl ligands.

2.2 Synthesis and characterisation of aldehyde-functionalised bipyridyl ligand (1)

Compound **1** was successfully synthesised *via* the oxidation reaction of 4,4'-dimethyl-2,2'-bipyridine with selenium dioxide in 1,4-dioxane (Scheme 2.1).[17]

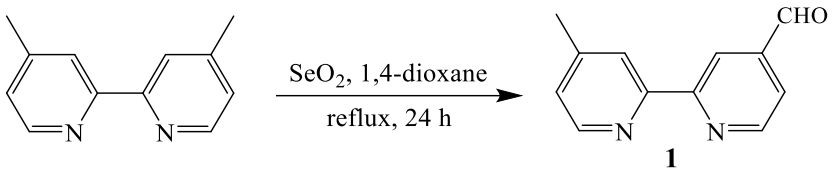

1

Scheme 2.1 Synthesis of aldehyde-functionalised ligand **1**.

The aldehyde (**1**) was obtained in low yield (28%) and this can be attributed to the formation of by-products during the reaction that is speculated to be resulting from overoxidation to carboxylic acids[17] and selenium by-products, which were removed during the reaction workup. Additionally, the possibility of poor conversion of the aldehyde into bisulfite adducts and extraction of the product during the purification and deprotection stages, cannot be ruled out (Scheme 2.2). The desired product (**1**) was then separated and extracted by increasing the pH to 10 since the efficient formation of the aldehyde requires high pH.[18]

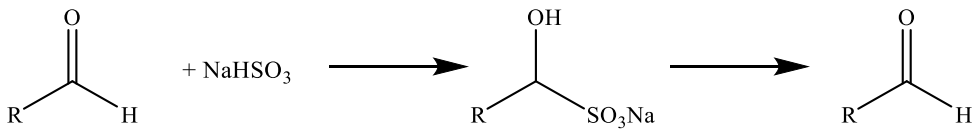

Scheme 2.2 Purification of aldehydes *via* the formation of bisulfite adducts.

2.2.1 NMR spectroscopy

The successful synthesis of 4'-methyl-2,2'-bipyridine-4-carboxaldehyde (**1**) was confirmed by ^{1}H NMR spectroscopy. The stacked spectra (Figure 2.3) shows a diagnostic singlet at 10.18 ppm, for ligand **1** (Figure 2.3b), assigned to the aldehyde proton (-C**H**O) and a singlet at 2.49 ppm, integrating for three protons, corresponding to the methyl protons confirming the successful oxidation of one methyl group. In addition to the singlet at 10.18 ppm, three new signals are observed in the aromatic region assigned to H-5, H-3 and H-6, which are not present in the spectrum of the starting material (Figure 2.3a). These new proton signals are due to the different substituents on the bipyridine rings breaking the symmetry that was observed for the starting material (Figure 2.3a). Two singlets at 8.84 and 8.29 ppm each integrating for one proton assigned to H-3 and H-3' of ligand **1**, appear to be more deshielded than H-5 and H-5'and this is due to the deshielding effects of the non-bonding electrons of the nitrogen atom of the adjacent pyridine ring in the *trans* configuration.[19] The signals assigned to H-5', H-6', H-5 and H-6, in the aromatic region, were assigned by evaluating their respective spin-spin coupling constants. The signals assigned to protons H-5 and H-5' at 7.72 and 7.20 ppm respectively appearing as doublets of doublets are coupling to H-6 (^{3}J = 4.9 Hz) and H-6' (^{3}J = 4.9 Hz), respectively. Protons H-5 and H-5' are also experiencing long-range coupling to protons H-3 (^{4}J = 1.5 Hz) and H-3' (^{4}J = 0.8 Hz) respectively, hence the observed doublets of doublets – a common observation for bipyridine protons.[17,19] It is interesting to note that there is a doubling up of signals assigned to H-6', H-3' and H-5' suggesting the presence of conformational isomers due to free rotation around the 2,2'-carbon single bond of the bipyridine. The obtained spectral data was compared against previously reported literature values and found to be in agreement.[17]

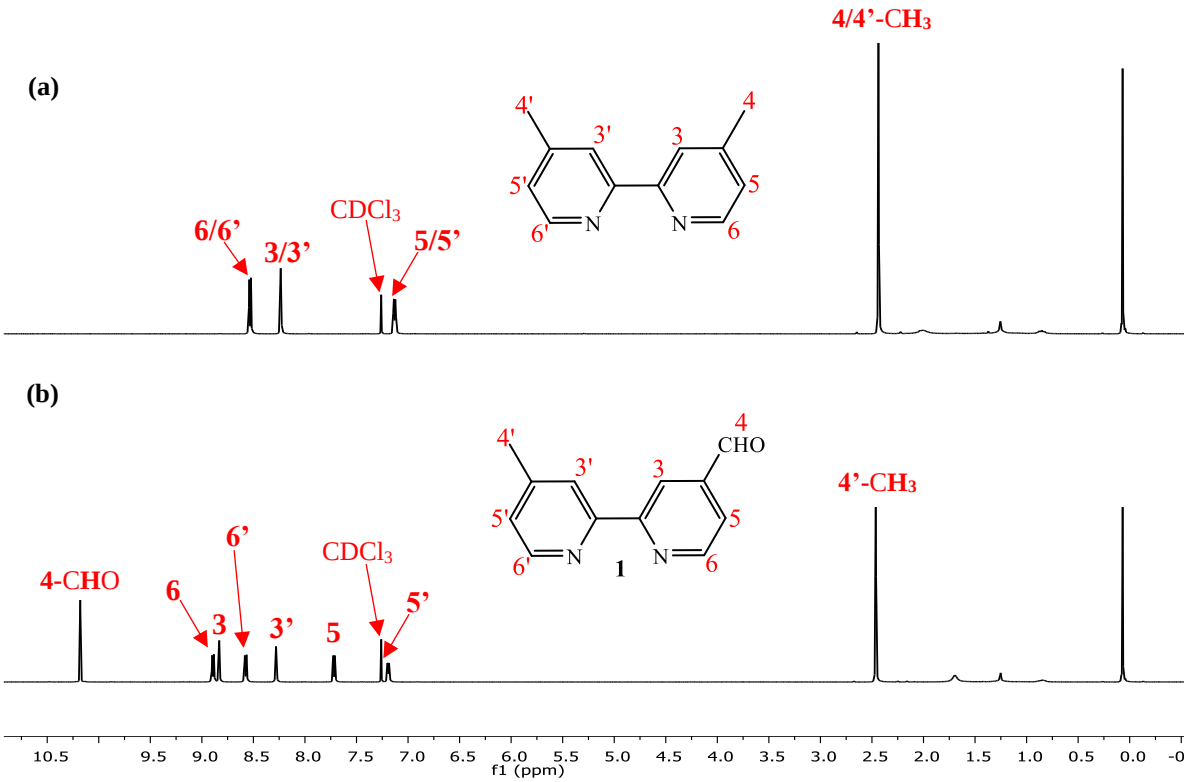

Figure 2.3 Stacked ^{1}H NMR spectra of (a) 4,4'-dimethyl-2,2'-bipyridine and (b) ligand **1** in $CDCl_3$.

2.2.2 Infrared (IR) spectroscopy

The infrared spectrum of **1** (Figure 2.4) further supports the ^{1}H NMR data (Figure 2.3), where a characteristic absorption band at 1702 cm^{-1} assigned to the ν(C=O) stretching frequency is observed thus confirming the successful oxidation of the methyl to a formyl group. Additionally, an absorption band at 1595 cm^{-1} attributed to the ν(C=N) stretching frequency in the structure of ligand **1** is observed and this agrees with the literature reported value of 1598 cm^{-1}.[17]

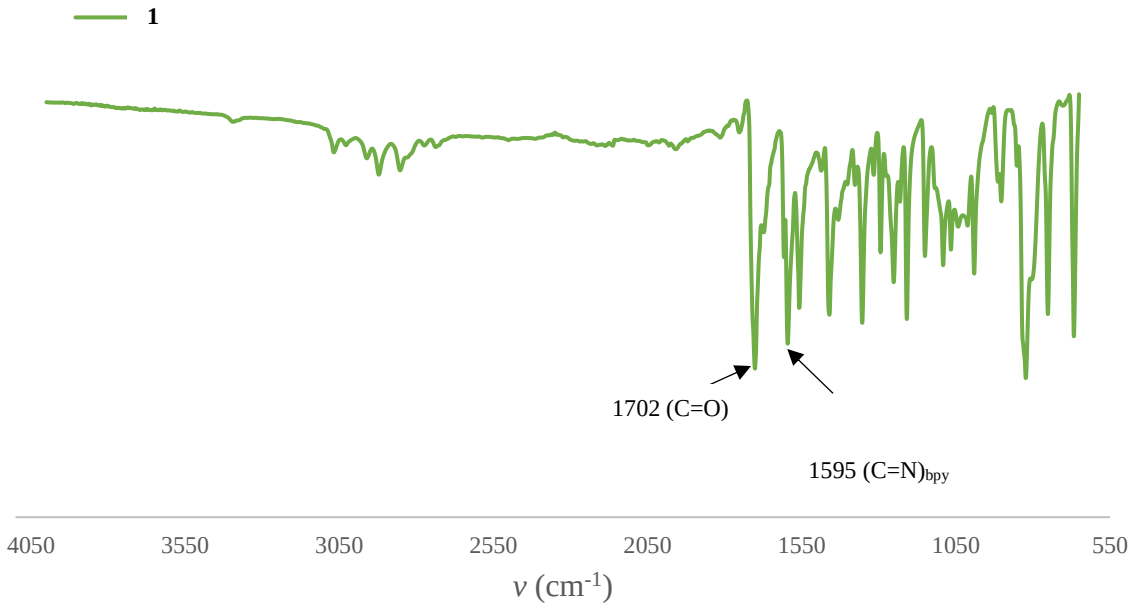

Figure 2.4 Infrared spectrum obtained for aldehyde-functionalised bipyridyl ligand (**1**).

2.2.3 Mass spectrometry

The obtained LC-MS data for ligand **1** further supports the spectral data, confirming the successful oxidation of only one of the methyl groups to a formyl. A base peak was observed at *m/z* = 199.1 in the spectrum, corresponding to the calculated mass of 198.08 g/mol assigned to the $[M+H]^+$ molecular ion.

2.3 Syntheses and characterisation of monomeric bipyridyl ligands (2, 3)

Ligands **2** and **3** were successfully synthesised *via* a Schiff base condensation (**2**) and reductive amination reaction (**3**) of 4'-methyl-2,2'-bipyridine-4-carboxaldehyde (**1**) with *n*-propylamine (Scheme 2.3).[20,21] Ligand **2** and **3** were isolated as yellow oils in low yields of 32% and 36%, respectively. The obtained yields were relatively lower than expected and it is suggested that some of the product was lost during the purification step.

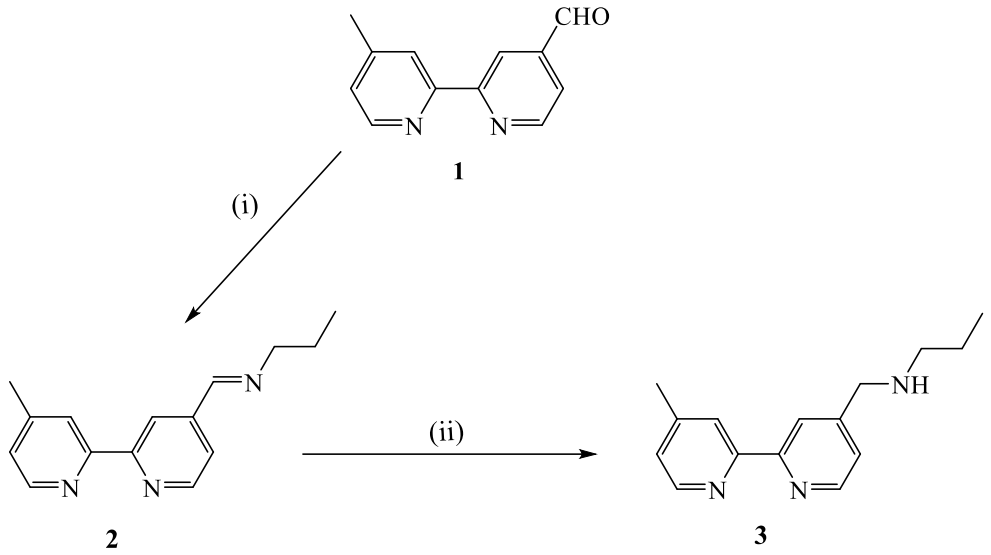

Scheme 2.3 Synthetic outline of reactions affording bipyridyl ligands **2** and **3**, following reaction conditions (i) 1 mol eq. of (**1**), 1 mol eq. *n*-propylamine, CH_2Cl_2, $MgSO_4$, rt, 24 h, and (ii) 2.6 eq. $NaBH_4$, CH_3OH, rt, 24 h.

Scheme 2.4 shows the reaction mechanism for the formation of **2**, where the carbonyl oxygen is protonated thus facilitating the nucleophilic attack by the amine at the electrophilic carbonyl carbon of the aldehyde. A proton transfer to the hydroxyl functionality of the intermediate forms a hydronium cation, which is eliminated as H_2O. The formed iminium intermediate undergoes further proton transfer to form the desired imine (C=N) and hydronium ion, which catalyses the subsequent condensation reaction by protonating the aldehyde.

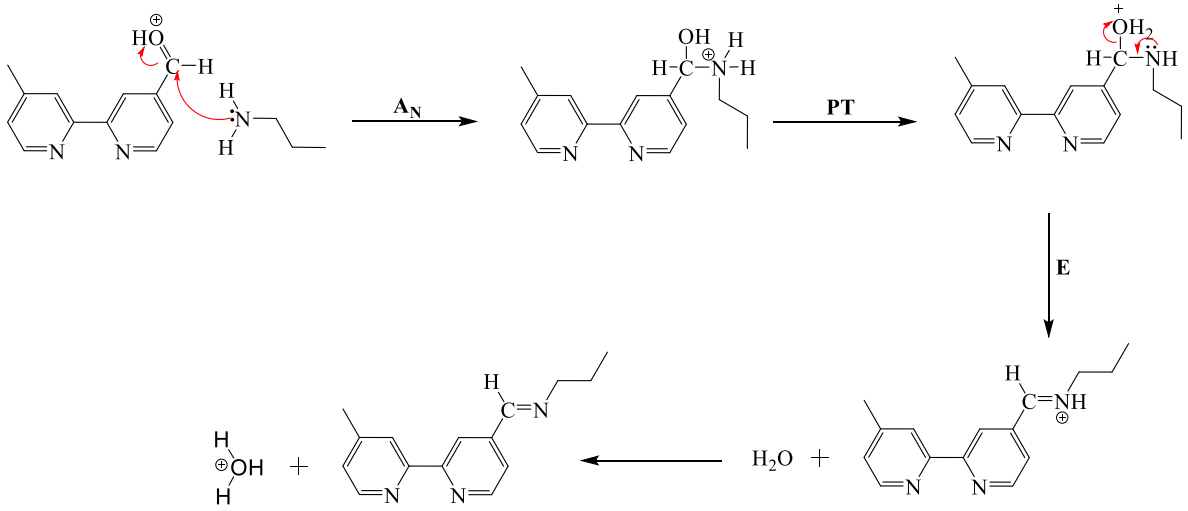

Scheme 2.4 Reaction mechanism illustrating the formation of the monomeric Schiff base condensation product (**2**), where A_N = nucleophilic addition, PT = proton transfer, and E = elimination.[22]

2.3.1 NMR spectroscopy

The ^{1}H NMR spectrum (Figure 2.5a) confirms the successful synthesis of ligand **2**, where a characteristic signal appearing as a singlet assigned to the imine proton H-7 at 8.38 ppm is observed. Comparing the obtained spectrum for **1** (Figure 2.3) with that of **2** (Figure 2.5a), three new signals in the aliphatic region are observed, in the spectrum of **2**, assigned to H-10, H-9 and H-8. The observed multiplicities for these new signals are as expected where H-8 and H-10 split into a triplet, and H-9 into a sextet due to vicinal coupling to H-8 (^{3}J = 6.9 Hz) and H-10 (^{3}J = 7.4 Hz). The observed proton signals collectively integrate for the expected number of protons and the chemical shift values are relatively in accordance with reported literature.[20]

The ^{1}H NMR spectrum for **3** (Figure 2.5b) was assigned following the previously reported literature work of Yao *et al.*[21] Successful reduction of the imine is confirmed by comparing the spectrum of **3** with that of **2**. The singlet at 8.60 ppm, which is assigned to the imine proton in the ^{1}H NMR spectrum of **2** is no longer present in the spectrum of **3**. The presence of a singlet at 3.68 ppm (H-7), integrating for two protons corresponding to benzylic protons (H-7) and the upfield shift of the triplet (H-8) from 3.64 ppm (Figure 2.5a) to 2.69 ppm (Figure 2.5b), further confirms the presence of an amine on the propyl side chain. The observed shift is possibly due to the electron-donating ability of the amine functionality in comparison to the imine. The ^{13}C {^{1}H} NMR for the ligands **2** and **3** has been previously reported and the obtained spectral data is in agreement to that reported in literature.[20,21]

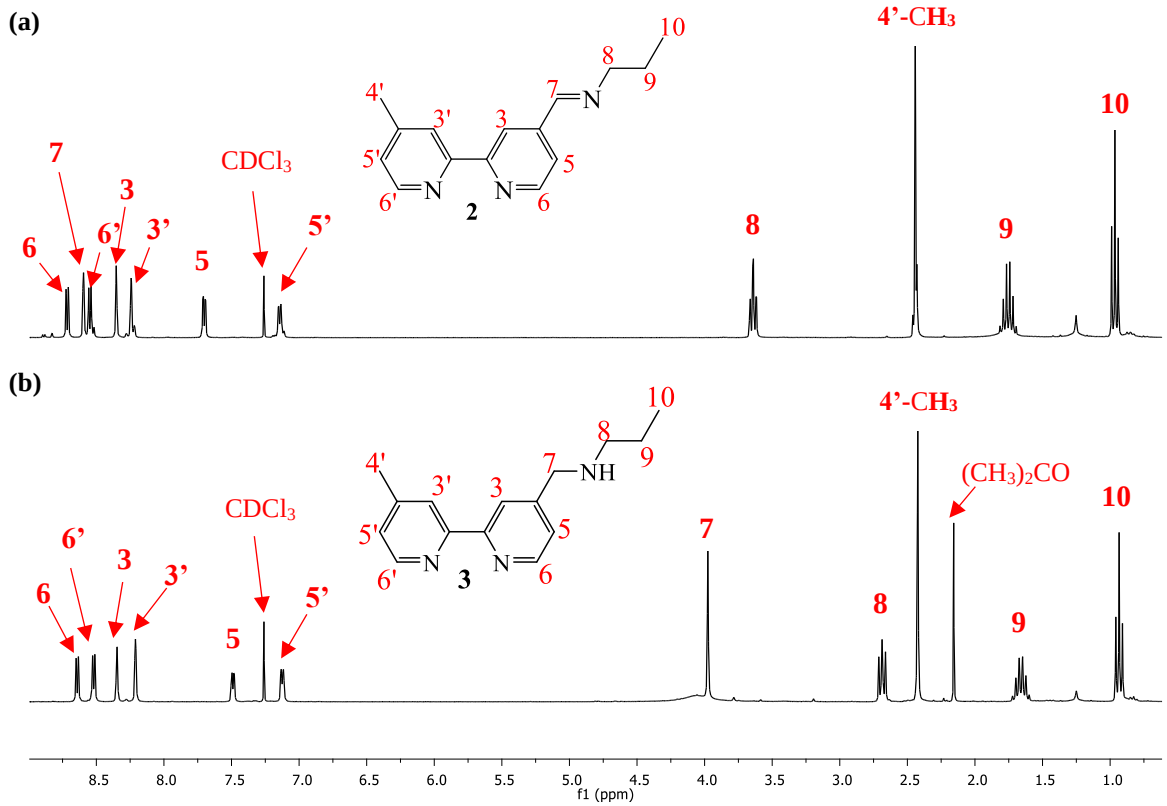

Figure 2.5 Stacked ^{1}H NMR spectra of ligands (a) **2** and (b) **3** in $CDCl_3$.

2.3.2 Infrared (IR) spectroscopy

The stacked infrared spectra of ligands **1**, **2** and **3** (Figure 2.6) shows an absorption band at 1702 cm^{-1} for ligand **1** attributed to the carbonyl functionality of the aldehyde. This absorption band is not observed in the spectrum of ligand **2**, instead the spectrum shows a stretching frequency for the imine (C=N) functionality at 1648 cm^{-1} confirming the successful formation of **2**. Additionally, the spectrum for **3** shows a weak absorption band at 3367 cm^{-1} that is due to the ν(N−H) stretching frequency of the secondary amine and this is not observed in the spectrum for **3** confirming the successful reduction of the imine. Furthermore, the absorption band at 1648 cm^{-1} observed in the spectrum for **2** is no longer present in the spectrum of ligand **3**.

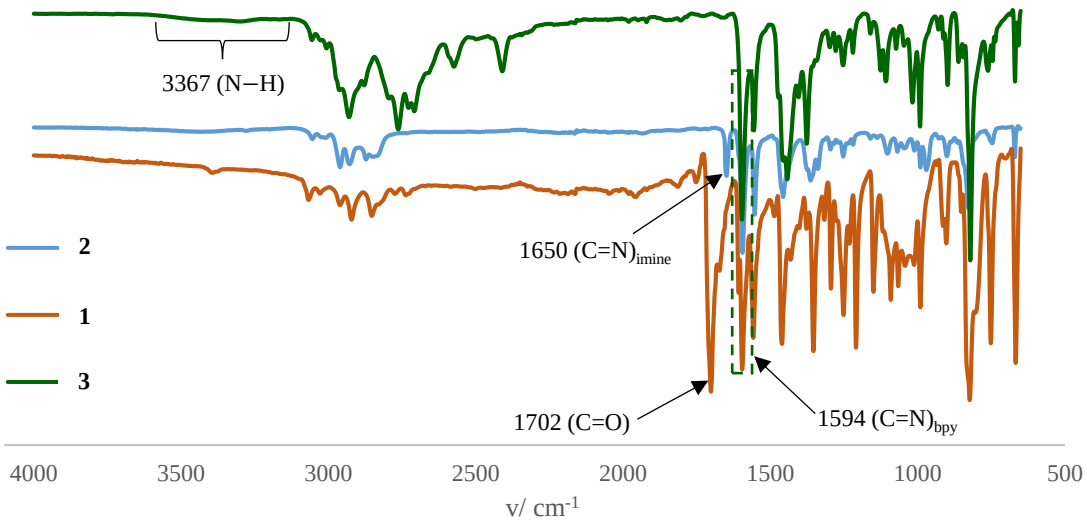

Figure 2.6 Stacked infrared spectra of ligands **1**, **2** and **3**.

2.3.3 Mass spectrometry

The LC-MS data for ligand **3**, which is the reduction product of ligand **2**, shows a peak at *m/z* = 242.1 g/mol corresponding to the calculated mass of 241.2 for the $[M+H]^+$ molecular ion. This further confirm the successful synthesis of **3** and supports the spectral data obtained for this ligand. The LC-MS data **3** also confirm that the previously reported imine functionalised ligand (**2**), which was the precursor to **3**, was successfully synthesised.[20]

2.4 Syntheses and characterisation of trimeric bipyridyl ligands (4, 5)

The trimeric ligands **4** and **5** were synthesised following an analogous procedure outlined in Scheme 2.5.[20,21] Three equivalents of ligand **1** were reacted with one equivalent of tris(2-aminoethyl)amine in dichloromethane to afford ligand **4** as a yellow oil in moderate yield (55%). Ligand **4** was subsequently reduced with sodium borohydride in dry methanol at room temperature to afford ligand **5** as a yellow oil (74%) (Scheme 2.5).

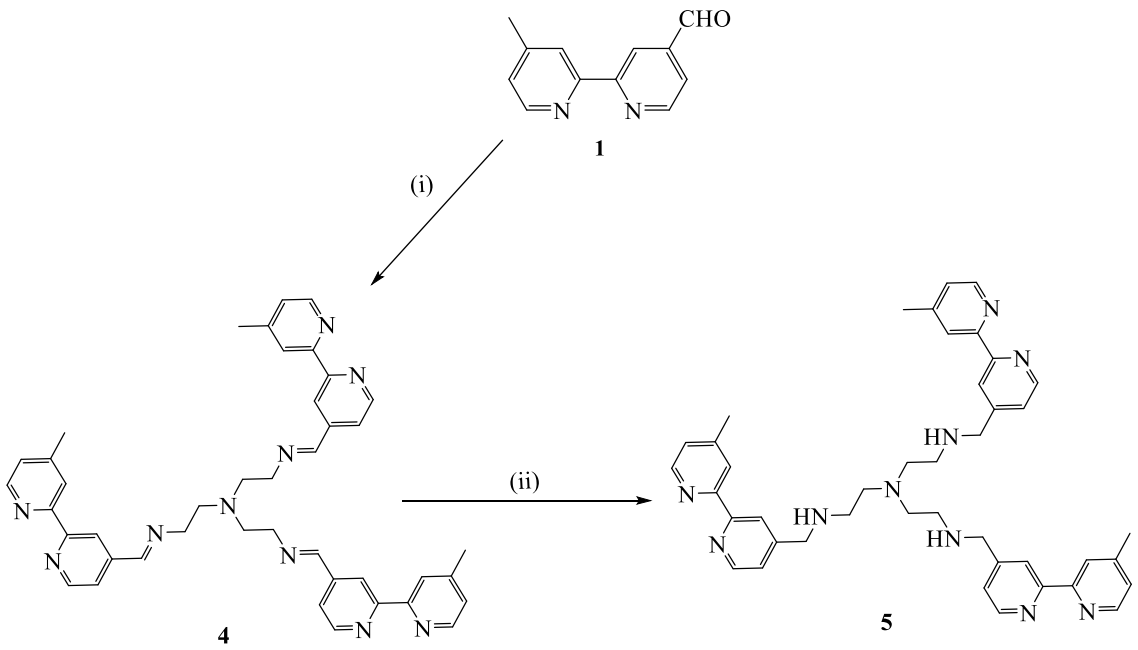

Scheme 2.5 Synthetic outline for the monomeric bipyridyl ligands (**4**, **5**), following reaction conditions (i) 3 mol eq. of (**1)**, 1 mol eq. tris(2-aminoethyl)amine, CH_2Cl_2, $MgSO_4$, rt, 48 h, and (ii) 4.5 mol eq. $NaBH_4$, CH_3OH, rt, 48 h.

2.4.1 NMR spectroscopy

The ^{1}H NMR spectrum (Figure 2.7) shows the diagnostic peak at 8.28 ppm assigned to the imine proton (H-7) integrating for three protons. The proton signal at 10.18 ppm previously assigned to the aldehyde proton (-C**H**O) of **1** is not observed in the spectrum of ligand **4** confirming the successful synthesis of **4**. In the aliphatic region, the two proton signals at 3.01 and 3.77 ppm each integrating for six protons assigned to H-9 and H-8 show the expected splitting pattern due to spin-spin coupling of the ethylene protons of the ligand core (^3J = 6.1 Hz and ^3J = 6.4 Hz). The observed proton signals collectively integrate to the expected number of protons.

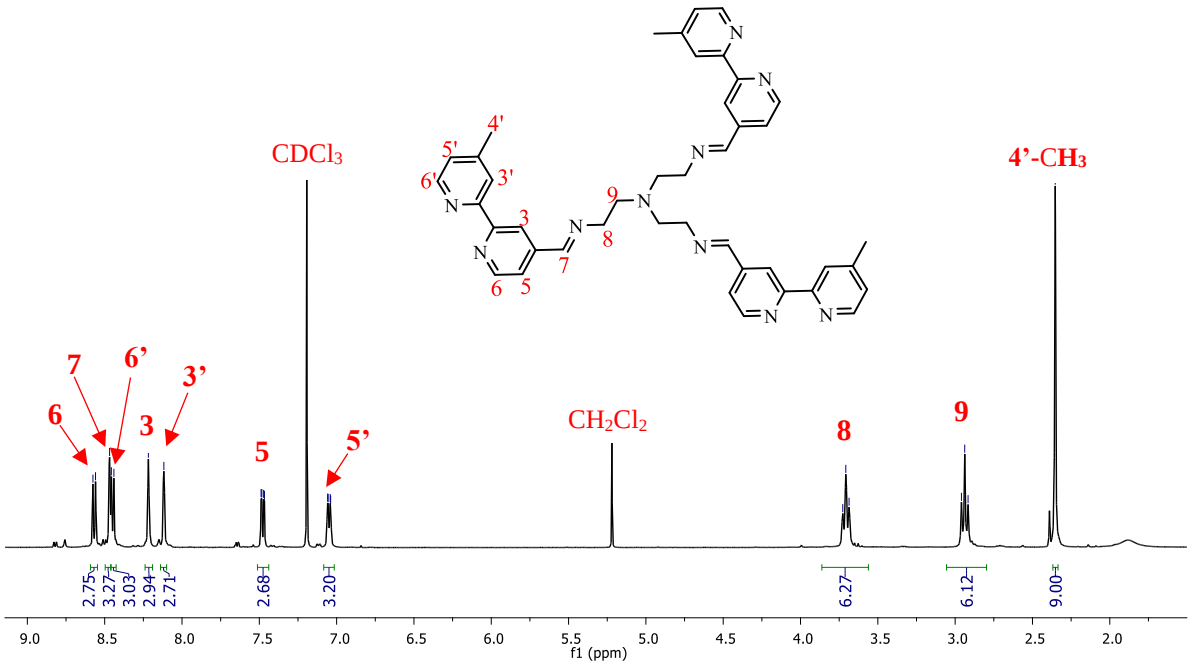

Figure 2.7 ^{1}H NMR spectrum of the trimeric ligand **4** in $CDCl_3$.

The obtained $^{13}C\{^{1}H\}$ NMR spectrum for ligand **4** (Figure 2.8) further confirm the successful synthesis of the trimeric amine-functionalised ligand with the characteristic carbon signal at 160.3 ppm assigned to the imine carbon (C-7). The observed carbon signal (C-7) supports the proton signal observed in the ^{1}H NMR spectrum (Figure 2.7) at 8.28 ppm.

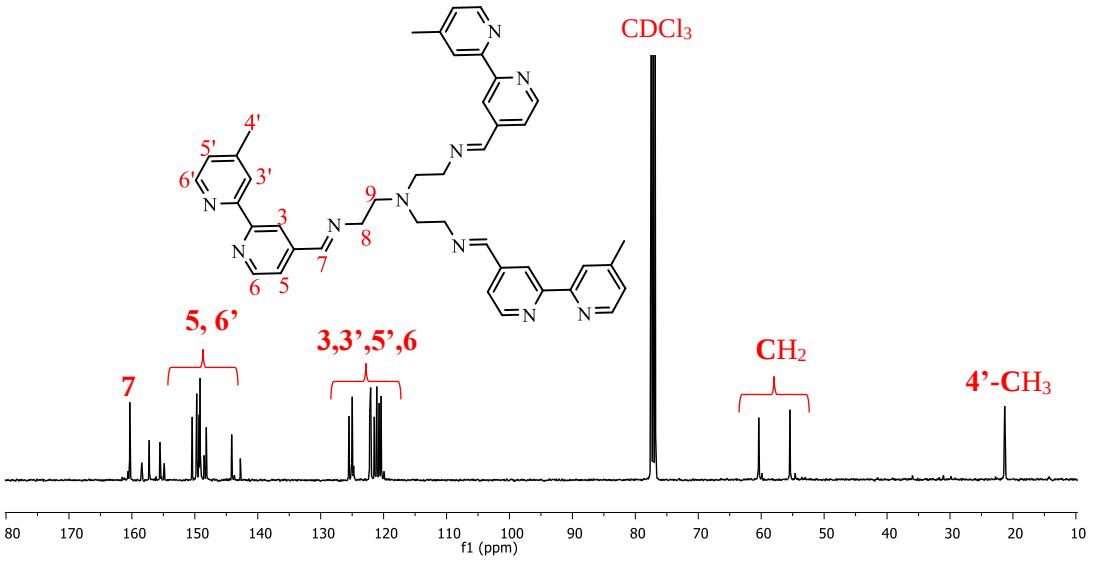

Figure 2.8 $^{13}C\{^{1}H\}$ NMR spectrum of trimeric ligand **4** in $CDCl_3$.

The ^{1}H NMR spectrum of **5** (Figure 2.9) shows a singlet at 3.83 ppm integrating for six protons and assigned to H-7 confirming the successful reduction of the imine (C=N). Furthermore, the stacked ^{1}H NMR spectra of **4** and **5** (Appendix A, Figure A1) shows an upfield shift of the two doublets at 2.73 and 2.68 ppm assigned to protons H-8 and H-9 respectively, due to the different groups affecting the local magnetic environment confirming that the imine has been successfully reduced to an amine. The singlet at 8.38 ppm assigned to the imine proton (H-7) in the spectrum of **4** is not observed in the spectrum of **5** and this is consistent with what is observed in the infrared spectrum of the isolated product. In the aromatic region, the expected signals assigned to protons H-5/5', H-6/6' and H-3/3' are observed with the expected proton ratios and multiplicities.

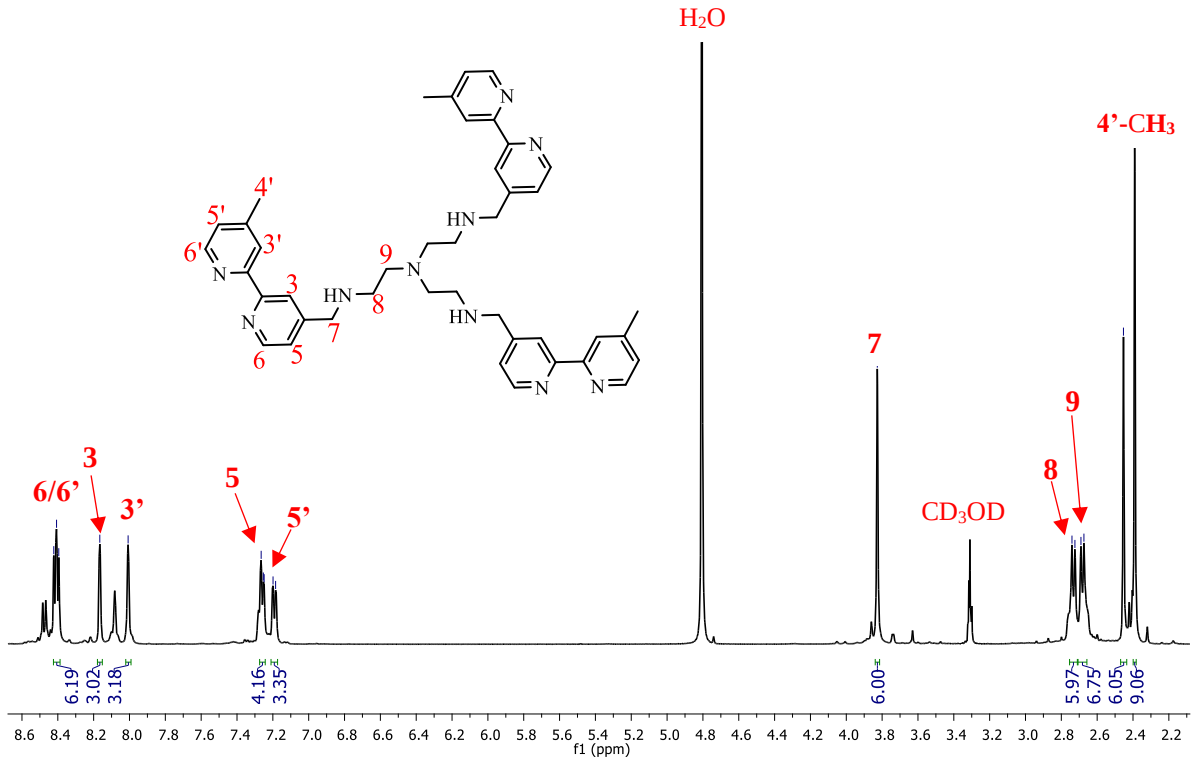

Figure 2.9 ^{1}H NMR spectrum of the trimeric ligand **5** in CD_3OD.

The obtained ^{13}C{^{1}H} NMR spectrum for **5** supports the ^{1}H NMR data (Figure 2.9) with the presence of a characteristic carbon signal at 63.6 ppm assigned to C-7 (Figure 2.10). This observed carbon signal confirms the successful reduction of the imine to the corresponding amine.

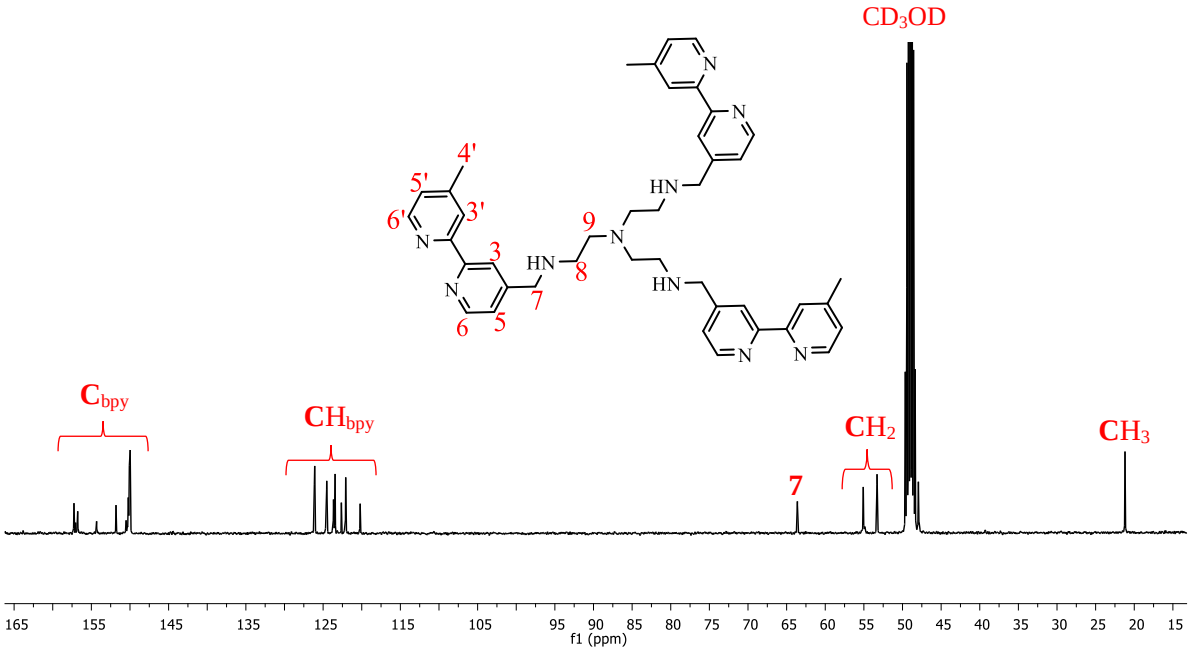

Figure 2.10 $^{13}C\{^{1}H\}$ NMR spectrum of the trimeric ligand **5** in CD_3OD.

2.4.2 Infrared (IR) spectroscopy

The stacked infrared spectra of the ligand precursor (**1**), isolated product (**5**) and the tris-imine ligand (**4**) (Figure 2.11) confirms the successful formation of **5**. The spectrum for **4** shows an absorption band at 1648 cm^{-1} assigned to the ν(C=N) stretching frequency, which is not observed in the spectrum of **5** thereby confirming the reduction of all imine functionalities. The broad absorption band observed at 3294 cm^{-1} assigned to the amine ν(N−H) stretching frequency further supports the spectral data. In addition, no absorption band is observed at 1702 cm^{-1}, which was previously assigned to the C=O functionality (Figure 2.4), confirming the conversion of the starting material to the amine scaffold (**5**).

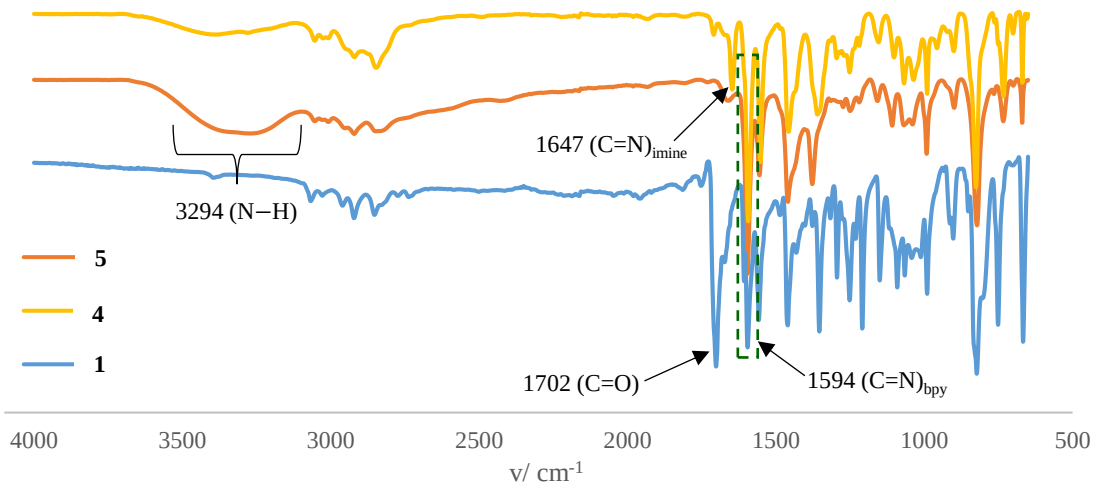

Figure 2.11 Stacked infrared spectra of ligands **1**, **4** and **5**.

2.5 Synthesis and characterisation of ruthenium(II) complex precursor (6)

Complex precursor **6** was synthesised *via* the ligand substitution reaction of ruthenium trichloride with two equivalents of 2,2'-bipyridine in *N*,*N*-dimethylformamide (Scheme 2.6).[23] The product was isolated as a black powder in good yield (82%).

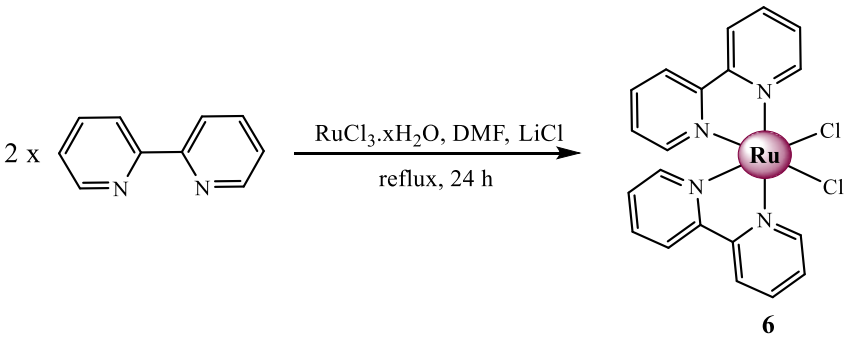

Scheme 2.6 Synthesis of complex precursor **6**.

2.5.1 NMR spectroscopy

The obtained ^{1}H NMR spectrum (Figure 2.12) shows eight signals in the aromatic region collectively integrating for the expected number of protons, in agreement with reported literature for this complex.[23] The most deshielded proton signal at 9.97 ppm (Figure 2.12) appearing as a doublet of doublets is assigned to H-6, which is expected to have less electron density due to its close proximity to the metal centre. Protons H-3 and H-3' are more deshielded than H-4/4' and H-5/5' and this is suggested to be due to steric strain upon them resulting from

cis configuration of the ligand upon coordination to the metal ion as well as the anisotropic effect of the ring current.[24] The proton signals at 7.77 and 7.10 ppm are assigned to H-5 (^3J = 7.2, ^3J = 3.5, ^4J = 0.7 Hz) and H-5' (^3J = 7.2, ^3J = 5.8, ^4J = 1.3 Hz), respectively and they display the expected multiplicity that is due to spin-spin coupling with H-6 and H-4, for H-5, and H-6' and H-4' for H-5' as well as long range coupling to H-3/3'. Moreover, the proton signal assigned to H-4 appears to be more deshielded than H-5, this is suggested to be due to H-4 being in the *ortho* position relative to the nitrogen atom of the pyridyl ring and the dicationic metal ion. Comparing protons H-4 and H-4', it is observed that H-4 is more deshielded and this is due to the deshielded H-4, in comparison to H-4', is suggested to be due to the effects of the ligands *trans* to these protons, where H-4' is *trans* to a chloride while H-4 is *trans* to a bipyridyl ring.[25]

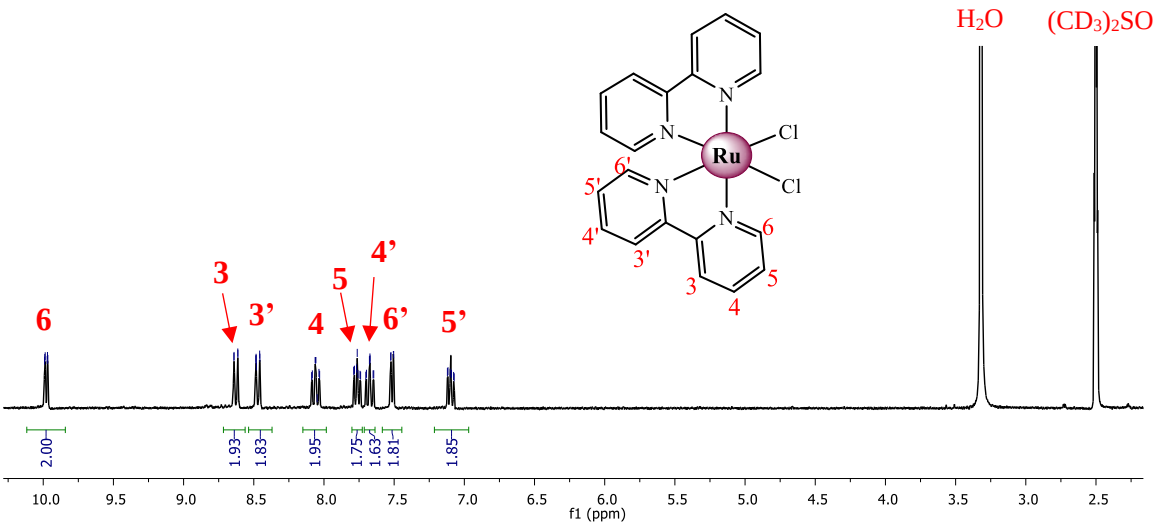

Figure 2.12 ^{1}H NMR spectrum of complex precursor **6** in $(CD_3)_2SO$.

2.5.2 Infrared (IR) spectroscopy

Figure 2.13 shows the stacked infrared spectra of **6** and 2,2'-bipyridine. The stretching frequency for the C=N functional group of the bipyridyl shifts from 1578 to 1585 cm^{-1} upon coordination of the free ligand to the ruthenium metal centre. The broad absorption band at 3462 cm^{-1} is attributed to the O−H functionality of water, which was used in the workup process.

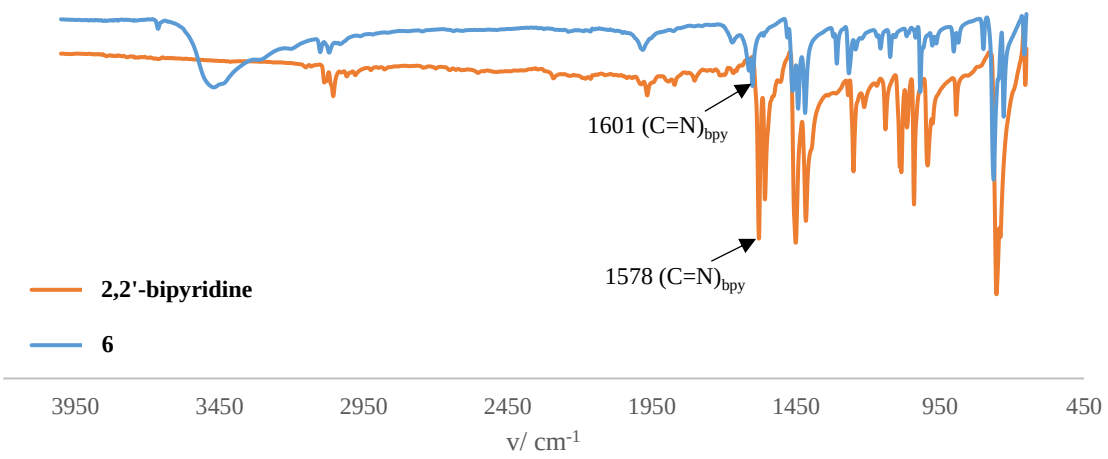

Figure 2.13 Stacked infrared spectra of complex precursor **6** and 2,2'-bipyridine.

2.6 Synthesis and characterisation of ruthenium(II) complex (7)

The ruthenium complex **7** was synthesised *via* modifications to the procedure outlined for complex precursor **6** by reacting three equivalents of bipyridine with ruthenium trichloride in *N*,*N*-dimethylformamide (Scheme 2.7).[23] The product was isolated as an orange powder in good yield (94%).

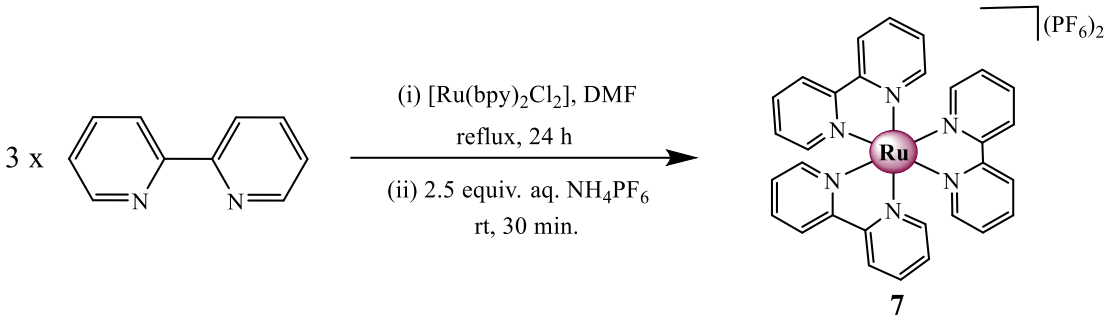

Scheme 2.7 Synthetic route used to obtain complex **7**.

2.6.1 NMR spectroscopy

The ^{1}H NMR spectrum (Figure 2.14) shows four signals in the aromatic region, which is expected for the homoleptic complex (**7**). The splitting patterns observed shows two doublets at 8.83 (H-3) and 7.74 ppm (H-6) and a triplet of doublets assigned to proton H-4 at 8.17 ppm. A similar trend observed for complex **6** (Figure 2.12) is observed in the spectrum for **7** (Figure 2.14), where H-3 is more deshielded upon complexation to the ruthenium metal ion due to steric strain with H-3' of the adjacent aromatic ring. The two deshielded signals (H-3 and H-4)

at 8.83 and 8.17 ppm show similar coupling constants of ^{3}J = 8.1 and ^{3}J = 8.0 Hz respectively, suggesting that the two protons are coupling to each other.

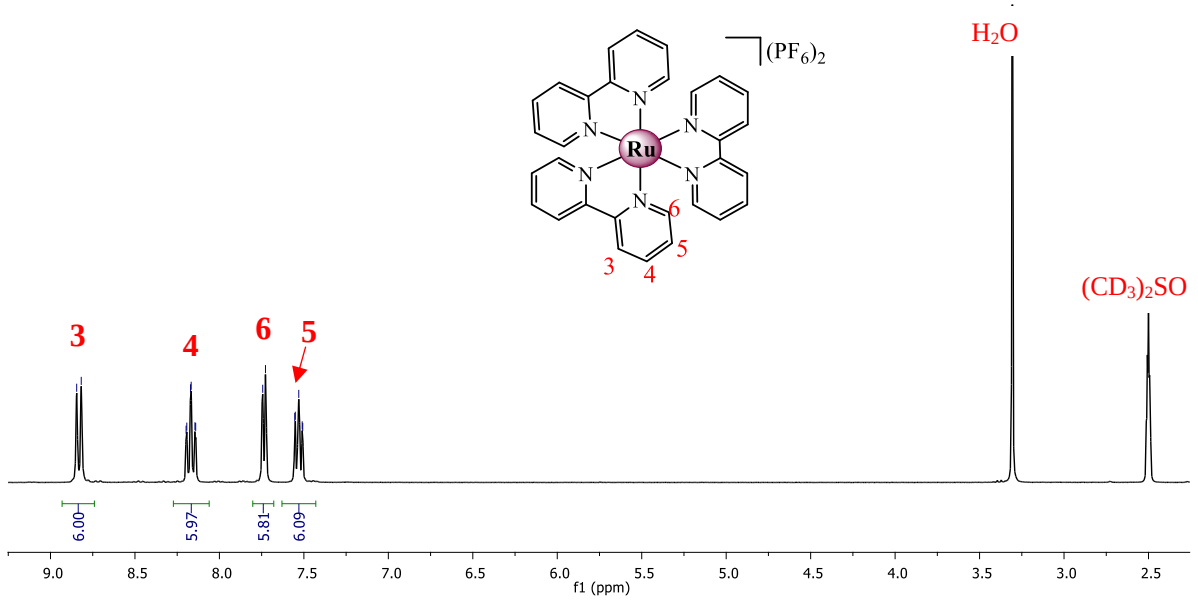

Figure 2.14 ^{1}H NMR spectrum of ruthenium(II) complex **7** in $(CD_3)_2SO$.

2.6.2 Infrared (IR) spectroscopy

The stacked infrared spectra (Figure 2.15) shows similar trends as that observed for complex precursor **6**. Upon coordination of the bipyridine ligand to the ruthenium metal centre, a shift to higher wavenumbers, of the ν(C=N) stretching frequency, is observed from 1578 to 1605 cm^{-1}. The shift of this homoleptic tris(bipyridine)ruthenium complex (**7**) is significant in comparison to that of the bis(bipyridine)ruthenium complex (**6**), likely due to the substitution of the weak field chloride ligands with strong field bidentate bipyridine ligand resulting in strengthened binding of the ligand to the metal ion hence the observed shift.

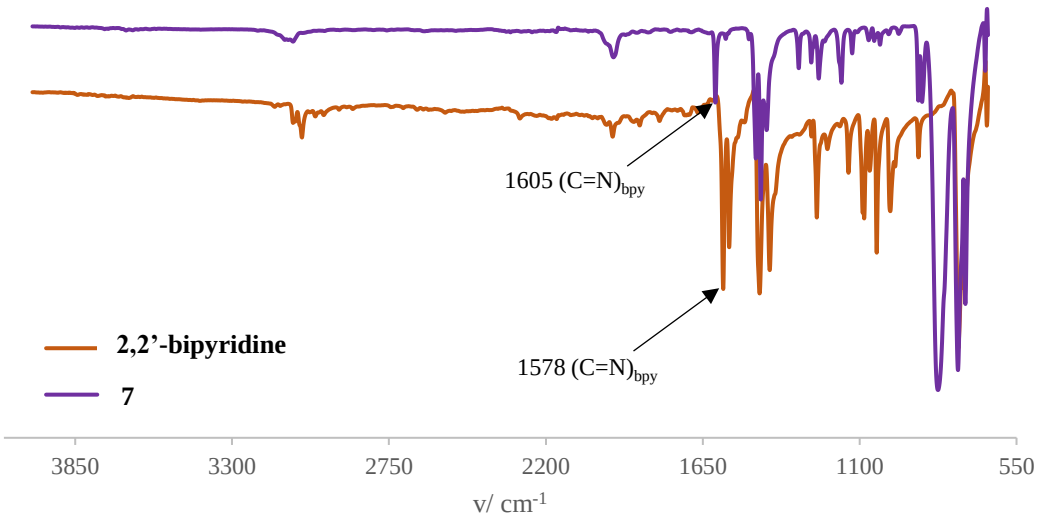

Figure 2.15 Stacked infrared spectra of complex **7** and 2,2'-bipyridine.

2.6.3 Mass spectrometry

The complex was further analysed using high resolution ESI-MS, further confirming the successful synthesis of **7**. A base peak at *m/z* = 285.0564 corresponding to the calculated mass of 285.0550 g/mol was observed and assigned to the presence of the $[M-2PF_6]^{2+}$ ion, that is, the loss of two hexafluorophosphate ions.

2.7 Syntheses and characterisation of ruthenium(II) mononuclear complexes containing an imine (9) and amine (10) functionality

2.7.1 Imine-functionalised ruthenium(II) complex (9)

Our initial attempts towards the synthesis of complex **9** were to first prepare the functionalised bipyridyl ligand (**2**) then perform the reaction of ligand **2** with the complex precursor (**6**) (Scheme 2.8).[26] However, the imine functionality cleaved under the reaction conditions even after reducing either the reaction time or the temperature, and the stacked ^{1}H NMR and infrared spectra (Figure 2.14 and 2.15 respectively) of ligand **1**, complex **8** and the isolated product confirms the imine cleavage of ligand **2** before/during the complexation reaction, suggested to be resulting from the relatively harsh reaction conditions.

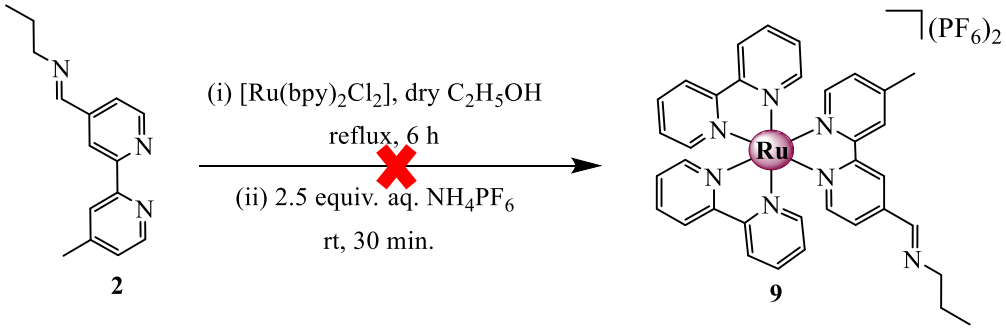

Scheme 2.8 Synthetic route for the mononuclear complex bearing a Schiff-base functionality (**9**).

2.7.1.1 NMR spectroscopy

The ^{1}H NMR spectrum of the isolated product (Figure 2.16c) show a singlet at 10.23 ppm assigned to the proton of the aldehyde functionality (4-C**H**O) which was observed at 10.18 ppm in the ^{1}H NMR spectrum of the aldehyde-functionalised free ligand (**1**) (Figure 2.16a). The corresponding aldehyde-functionalised ruthenium(II) complex was then synthesised and the ^{1}H NMR spectrum (Figure 2.16b) was compared with that of the isolated product (Figure 2.16c), it is observed that the two spectra display similar proton signals.

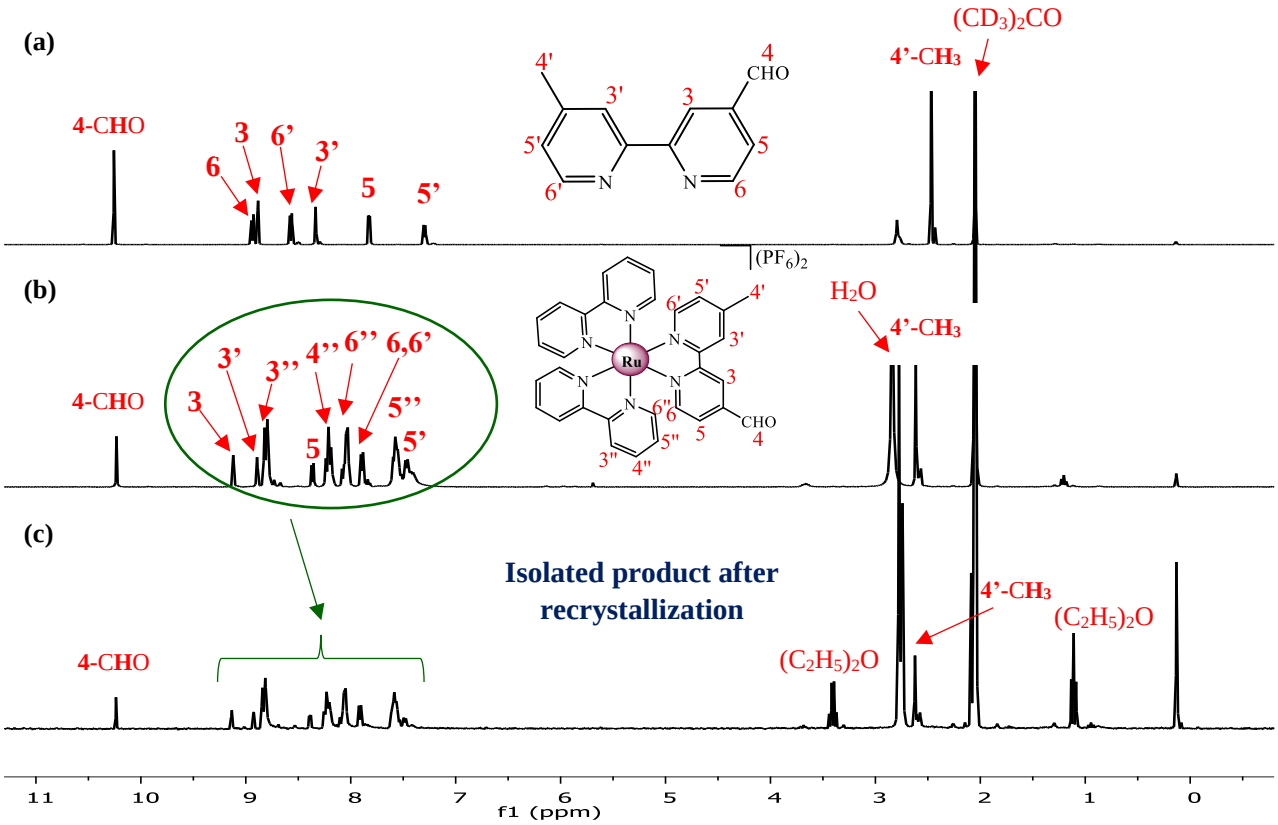

Figure 2.16 Stacked ^{1}H NMR ($(CD_3)_2CO$) spectra of (a) **1**, (b) **8** and (c) isolated product.

Moreover, the ^{1}H NMR spectrum of the isolated product before recrystallization (Figure 2.17) show two proton signals at 10.17 and 10.21 ppm assigned to 4-C**H**O of the free ligand and the complex, respectively. This confirms that the imine bond cleaved either before or during the complexation reaction with the imine-functionalised ligand (**2**).

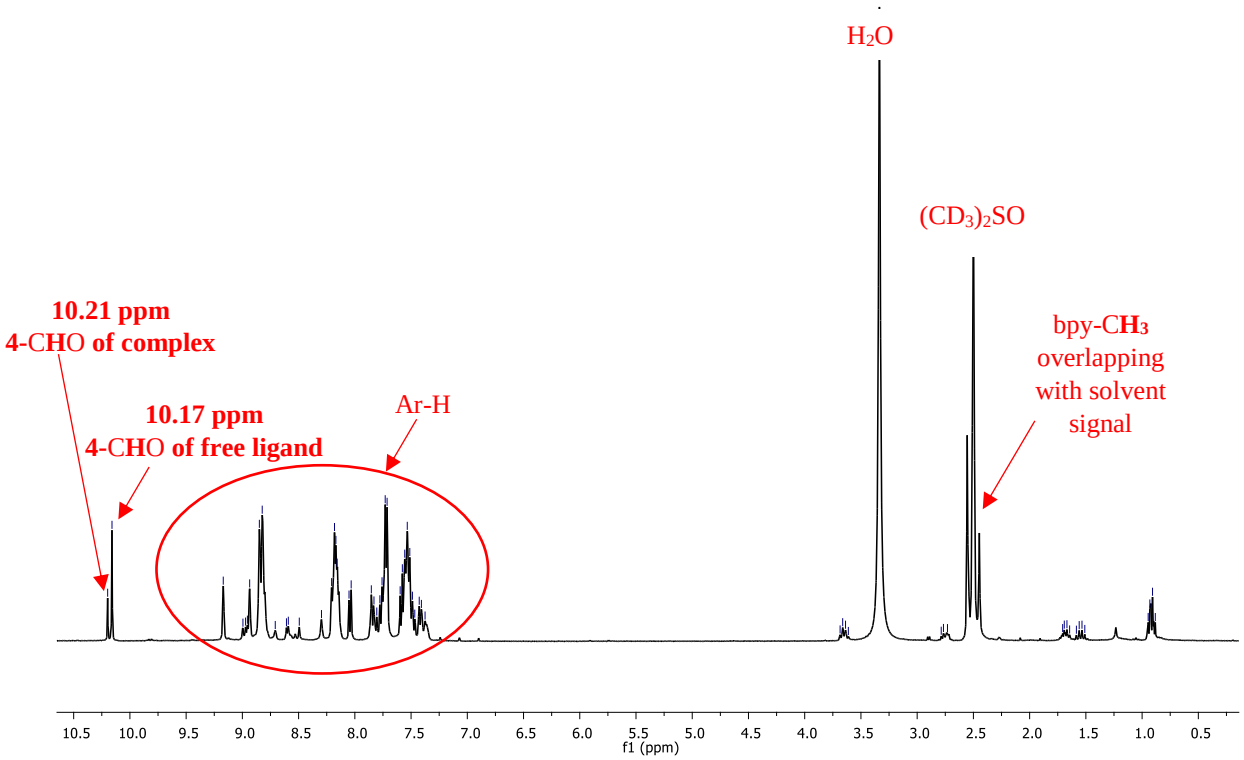

Figure 2.17 ^{1}H NMR spectrum of isolated product before recrystallization in $(CD_3)_2SO$.

2.7.1.2 Infrared (IR) spectroscopy

The infrared spectra (Figure 2.18) of the isolated product further supports the obtained ^{1}H NMR data suggesting the imine bond cleavage with the characteristic absorption band at 1707 cm^{-1} attributed to the carbonyl ν(C=O) stretching frequency. In addition, the spectrum of **2** shows an absorption band at 1650 cm^{-1} assigned to the imine functionality (C=N), which was expected to appear in the spectrum of the isolated product, however, this is not observed.

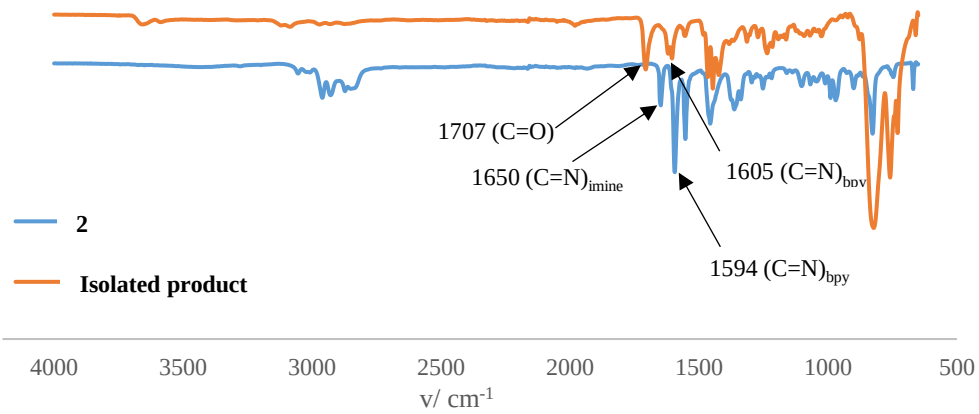

Figure 2.18 Stacked infrared spectra of imine-functionalised ligand (**2**) and isolated product after attempted complexation.

In this regard, complex **8** was successfully prepared *via* a substitution reaction between complex precursor **6** and ligand **1** in ethanol,[27] followed by the counter-ion exchange reaction of the resulting chloride salt using ammonium hexafluorophosphate to afford **8** as the hexafluorophosphate salt (Scheme 2.9) in good yield (85%). Thereafter, complex **9** was synthesised and isolated following a previously reported literature procedure, *via* the Schiff base condensation reaction of **8** with *n*-propylamine in ethanol and the product was isolated as a red powder in low yield (27%) (Scheme 2.9).[28]

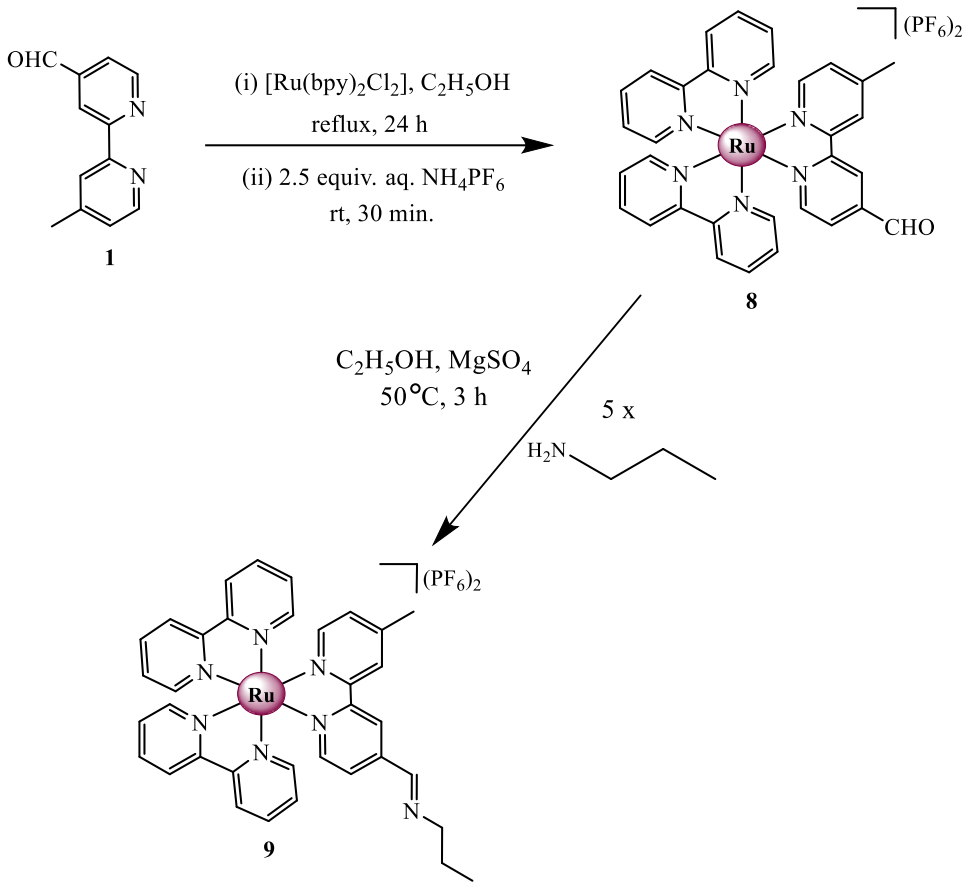

Scheme 2.9 Synthetic outline for the preparation of complex **9** *via* the Schiff base condensation reaction of *n*-propylamine with **8**.

2.7.1.3 NMR spectroscopy

The stacked ^{1}H NMR spectra of **8** (Figure 2.19) was assigned and compared to previously reported literature data.[27,29] The ^{1}H NMR spectrum of **8** (Figure 2.19a) shows a distinct signal at 10.24 ppm, characteristic of the aldehyde signal (4-C**H**O). This signal is not observed in the spectrum of **9**, which shows a new signal at 8.77 ppm integrating for one proton assigned to the imine proton (H-7). By comparison, the proton signals H-3 and H-5 are observed to be slightly deshielded for compound **8** than for **9** and this is attributed to the relatively electron-withdrawing inductive effects of the aldehyde functionality. In the aliphatic region, three signals are observed at 0.94, 1.69 – 1.79 and 3.68 ppm, which correspond to the protons on the *n*-propyl side chain (C**H**$_3$C**H**$_2$C**H**$_2$NCH) (Figure 2.19b), further confirmation of a successful Schiff-base condensation reaction. An upfield shift of proton H-3' is observed from 8.90 ppm (Figure 2.19a) to 8.53 ppm (Figure 2.19b), suggesting possible shielding effects by the propyl side chain. Furthermore, the spectrum (Figure 2.19b) shows a doublet of doublets at 7.81 ppm assigned to H-6. The observed multiplicity of H-6 is due to coupling to the protons H-5 (**^{3}J** =

5.9 Hz) and H-3 (^4J = 1.0 Hz). The doublet of doublets observed for the H-5' is due to a three bond coupling to H-6' (**^3J** = 4.8 Hz) and a four-bond coupling to H-3'(^4J = 0.6 Hz).

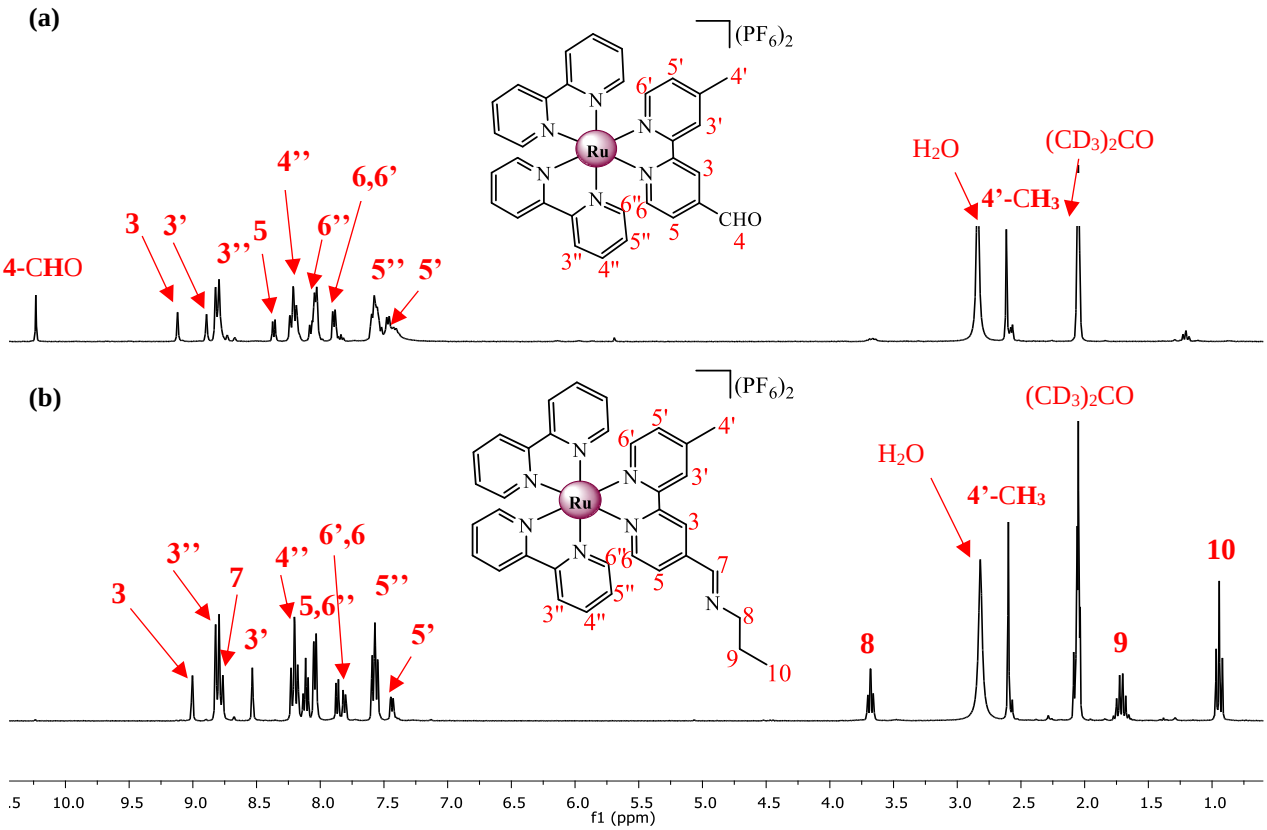

Figure 2.19 ^{1}H NMR spectra of mononuclear complexes (a) **8** and (b) **9** in $(CD_3)_2CO$.

Interestingly, the doubling up of proton signals observed in the ^{1}H NMR spectrum of the free ligand (Figure 2.3) is not observed in the spectrum of the corresponding complex (**8**) (Figure 2.19a). The free bipyridine ligand assumes a *cis*-conformation with respect to its nitrogen atoms and the free rotation 2,2'-carbon single bond does not occur upon complexation (Scheme 2.10) – an observation that has been previously reported.[30,31]

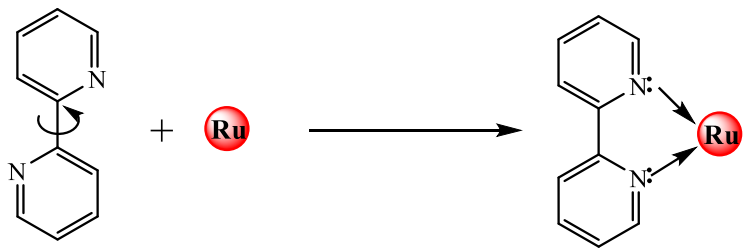

Scheme 2.10 General depiction of the orientation of the bipyridine ligand upon complexation to a ruthenium metal centre.

2.7.1.4 Infrared (IR) spectroscopy

The stacked infrared spectra of **8** and **9** (Figure 2.20) show an absorption band at 1623 cm^{-1} assigned to the imine ν(C=N) stretching vibrational mode. The spectrum of **9** shows no absorption band corresponding to C=O functionality (*ca*. 1707 cm^{-1}) as observed in the spectrum obtained for **8** further supporting the obtained ^{1}H NMR spectrum (Figure 2.19b).

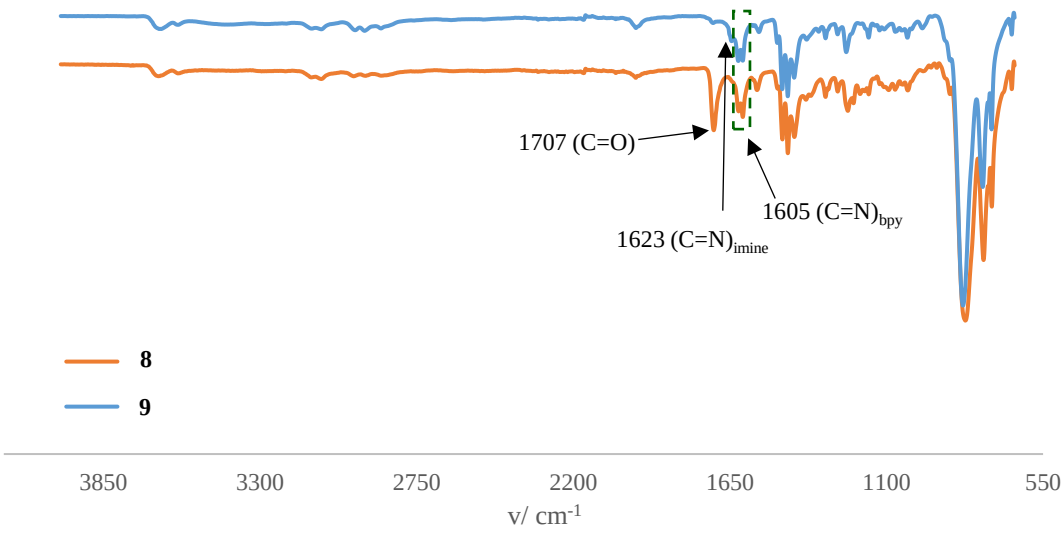

Figure 2.20 Stacked infrared spectra of mononuclear complexes **8** and **9**.

2.7.1.5 Mass spectrometry

The data obtained from high resolution ESI-MS confirm the successful synthesis of complexes **8** and **9**. A base peak for **8** was observed at *m/z* = 306.0609 corresponding to the calculated mass of 306.0600 g/mol assigned to the molecular ion with the loss of two hexafluorophosphate ions, $[M-2PF_6]^{2+}$. A base peak at *m/z* = 757.0843 corresponding to the calculated mass of 757.0800 g/mol assigned to $[M-PF_6]^{+}$ was also observed, which is due to the loss of one of the hexafluorophosphate counter-ion. The obtained mass spectrum for complex **9** shows a molecular ion peak at *m/z* = 315.0670 assigned to the $[M + 3H]^{3+}$ ion, corresponding to the calculated mass of 315.2373 g/mol.

2.7.2 Amine-functionalised ruthenium(II) complex (10)

Complex **10** was synthesised *via* the substitution reaction of the chloride ligands of $[Ru(bpy)_2Cl_2]$ with ligand **3** in a mixture of water/ethanol.[32] This was followed by the counter-ion exchange reaction with ammonium hexafluorophosphate to afford **10** as the hexafluorophosphate salt (Scheme 2.11) in good yield (86%). A recent study conducted by

Farney *et al*. demonstrated the effects of counter-ion identity on the ruthenium(II) cationic complexes. It was found that the counter-ion identity can have an effect on the lifetime of the excited-state and the rate of radical cation reactions initiated by these complexes, which act as photoredox catalysts.[33] Among the counter-anions that were evaluated, the hexafluorophosphate-based ruthenium(II) complex was one of the reactive photocatalysts with an increased triplet excited-state energy and lifetime.[33] Also, the hexafluorophosphate ruthenium salt show superior solubility in common laboratory solvents such as acetonitrile compared to the chlorido anion. In light of these findings, the counter-ion exchange was carried out to afford the hexafluorophosphate ruthenium salt.

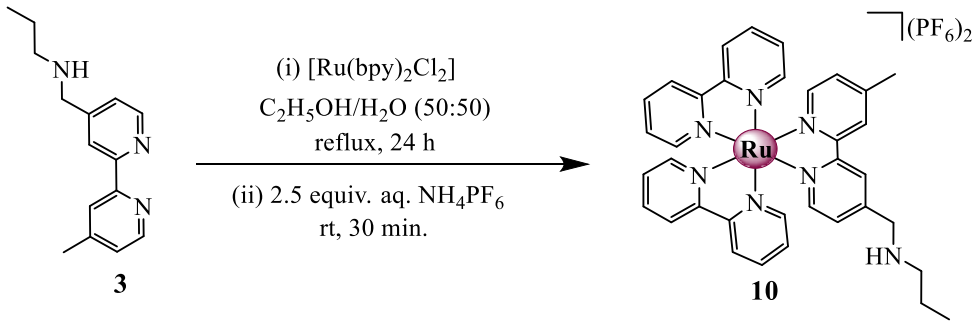

Scheme 2.11 Synthesis of mononuclear ruthenium(II) heteroleptic complex **10**.

2.7.2.1 NMR spectroscopy

The ^{1}H NMR for complex **10** was recorded in CD_3CN because in $(CH_3)_2CO$ signal H-8 was masked by the broad water peak (Appendix A, Figure A2). Figure 2.21 show the obtained ^{1}H NMR spectrum of **10** and from this, a characteristic deshielded singlet at 4.75 ppm is observed, assigned to the proton H-7 confirming the coordination of ligand **3** to the metal centre. In the aliphatic region, three signals are observed at 1.00, 1.82 – 1.94 and 2.84 ppm integrating for the expected number of protons and are assigned to H-10, H-9, and H-8, respectively. The aromatic region shows several multiplets, which are due to the overlapping of signals as a result of the bipyridyl protons being in very similar electronic environments. This presents a challenge in assigning the respective protons, which is common for heteroleptic ruthenium polypyridyl complexes. Irrespectively, the observed proton signals collectively integrate for the expected 35 protons corresponding to the complex **10**.

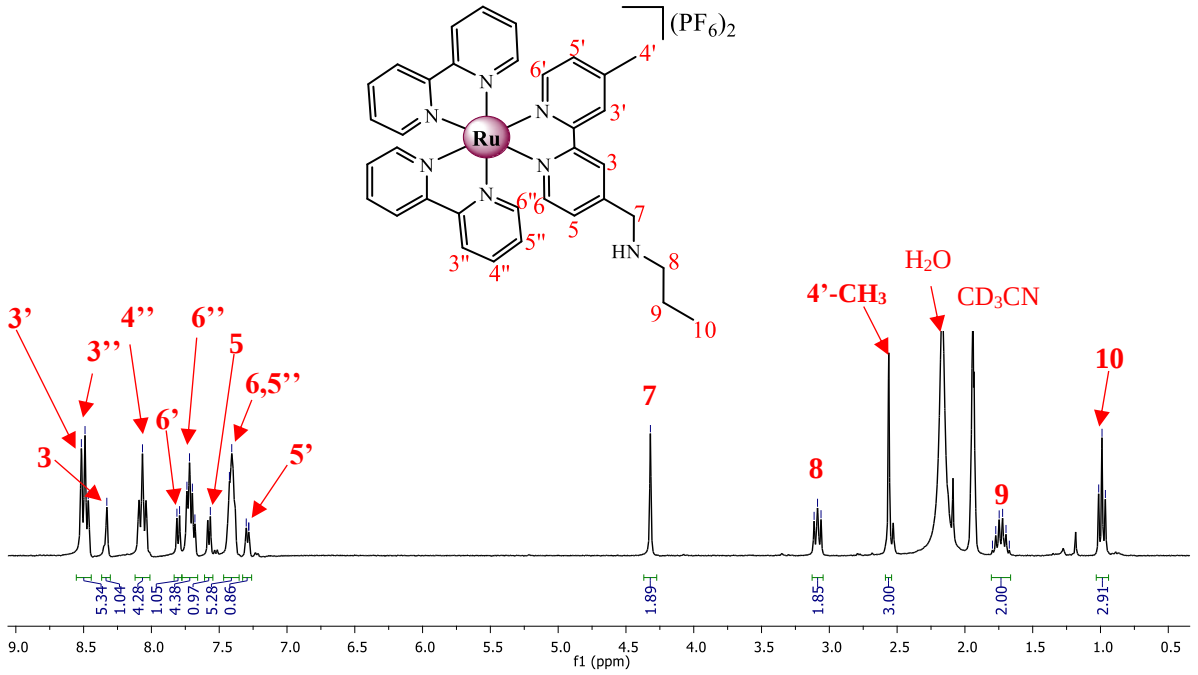

Figure 2.21 ^{1}H NMR spectrum of complex **10** in CD_3CN.

The $^{13}C\{^{1}H\}$ NMR spectra for complexes **9** and **10** further confirm the successful synthesis of the two new mononuclear complexes (Figure 2.22) with the characteristic carbon signal at 50.2 ppm for complex **10**. Five distinct signals in the aliphatic region of the amine-functionalised complex (Figure 2.22a) are observed at 10.0, 19.4, 20.1, 50.2 and 50.7 ppm and assigned to carbons C-10, C-9, 4'-**C**H_3, C-7 and C-8, respectively. Comparing these signals with those of the imine-functionalised complex (**9**) (Figure 2.22b), it is observed that the signals are slightly deshielded for complex **9** and this is attributed to the presence of the imine functionality. The aromatic carbons were observed in the 123 – 159 ppm region and was assigned using HSQC NMR analysis (Figure 2.23).

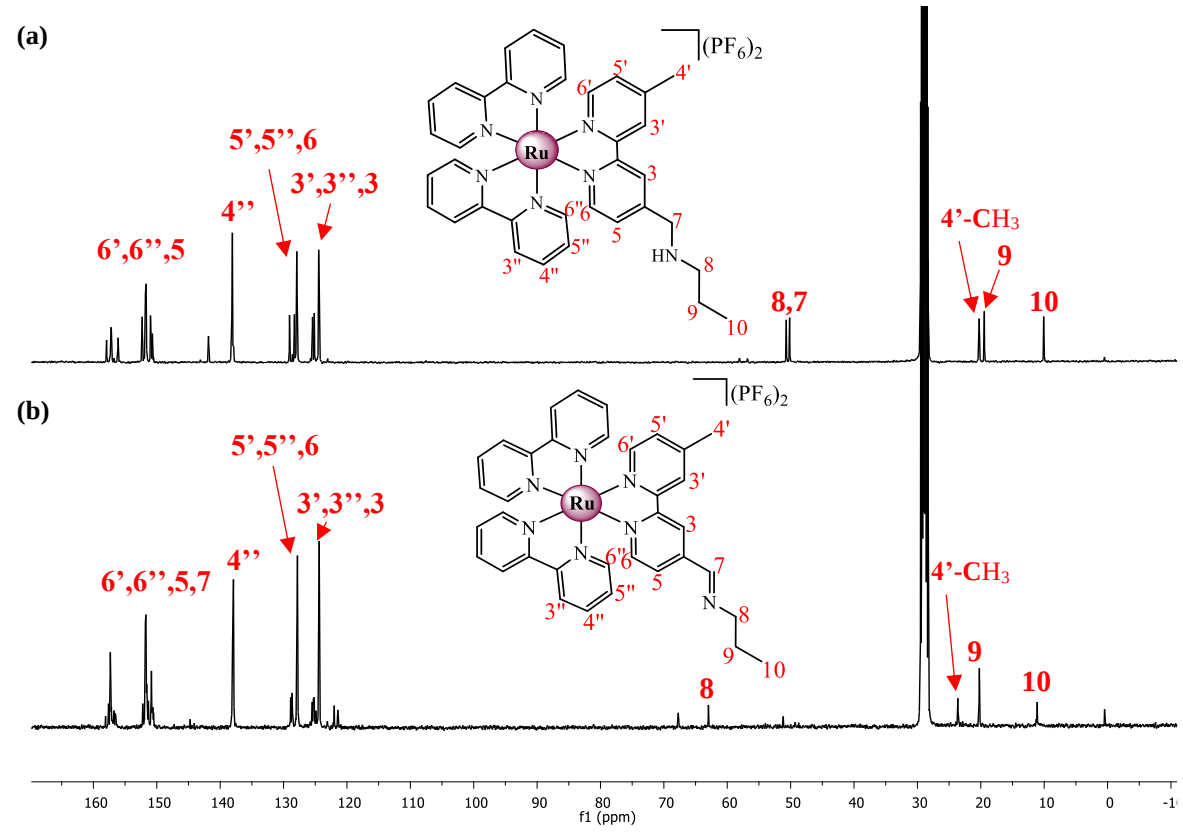

Figure 2.22 Stacked $^{13}C\{^{1}H\}$ NMR spectra of complexes (a) **10** and (b) **9** in $(CD_3)_2CO$.

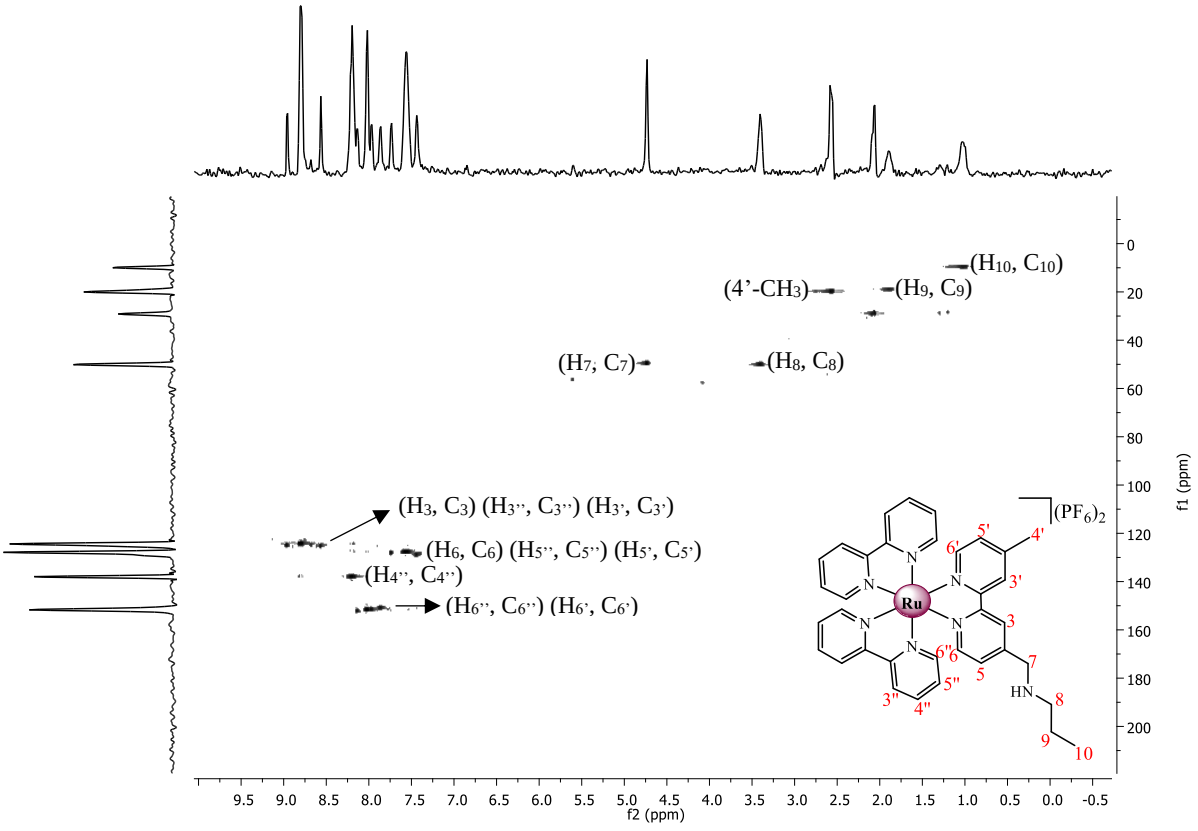

Figure 2.23 HSQC NMR spectra of complex **10** in $(CD_3)_2CO$.

2.7.2.2 Infrared (IR) spectroscopy

The stacked infrared spectra of **3** and **10** (Figure 2.24) shows a shift of the ν(C=N) stretching frequency to a higher frequency upon coordination. This observation suggests a shortening of bond length due to the presence of a dicationic metal ion. Scarborough *et al*. reported similar observations, where the C−N bond length was found to be shorter in comparison to those of the C−C in the bipyridine ring, explaining the observed shift to higher frequencies in the infrared spectrum of the synthesised ruthenium complexes.[34]

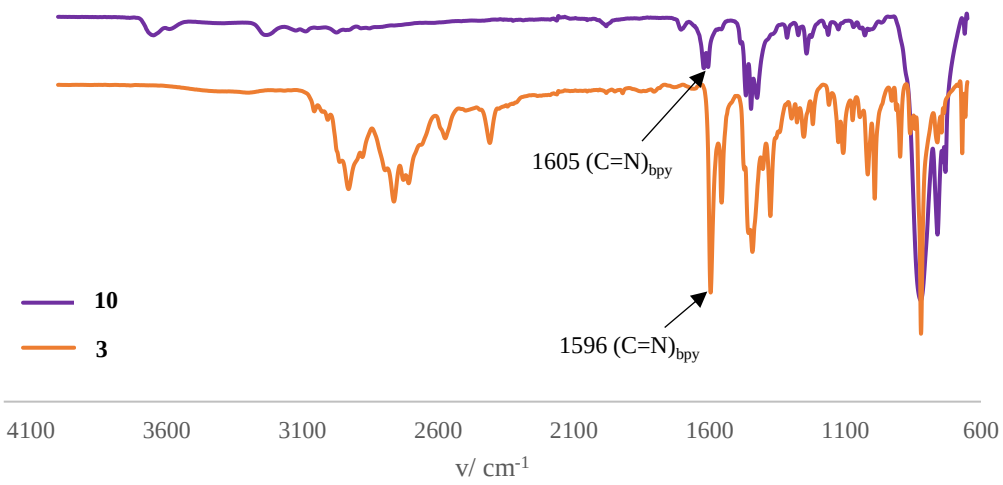

Figure 2.24 Stacked infrared spectra of **3** and **10**.

2.7.2.3 Mass spectrometry

The data obtained from high resolution ESI-MS further confirmed the successful synthesis of complexes **10**. A base peak was observed at *m/z* = 327.6000 corresponding to the $[M-2PF_6]^{2+}$ ion with calculated mass of 327.3900 g/mol. Additionally, a base peak is observed at 946.1381, corresponding to the $[M + H]^+$ molecular ion with a calculated exact mass of 946.1273 g/mol.

2.8 Syntheses and characterisation of ruthenium trinuclear complexes (11, 12)

Complex **11** was synthesised by means of a reaction between tris(2-aminoethyl)amine and three equivalents of complex **8** in ethanol and the product was isolated as a red powder in moderate yield (59 %) (Scheme 2.12).[28]

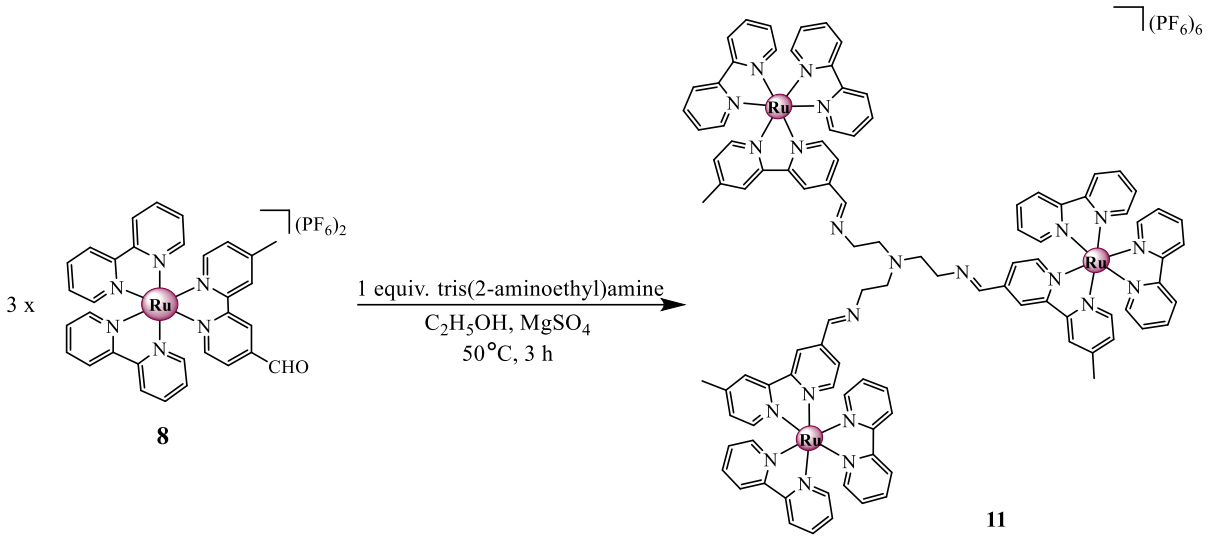

Scheme 2.12 Synthetic outline for the trinuclear complex containing imine functionalities (**11**).

Complex **12** was synthesised by means of a reaction between ligand **5** and three equivalents of complex precursor **6** in a mixture of ethanol/water under reflux for 24 h (Scheme 2.13).[35] The product was isolated as the hexafluorophosphate salt in good yield (81%) after recrystallization from an acetonitrile/diethyl ether mixture.

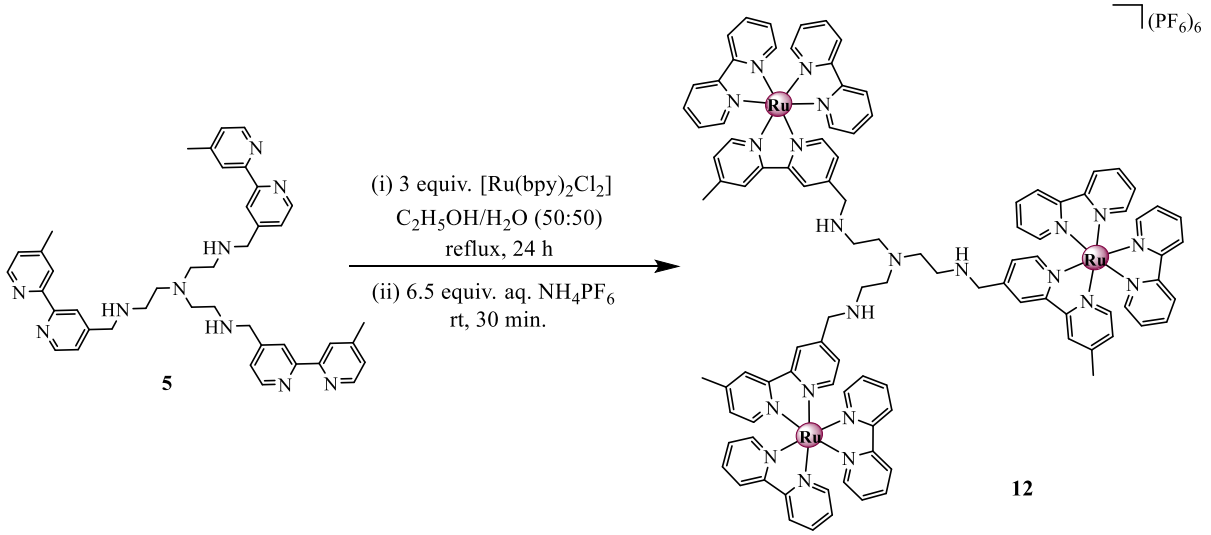

Scheme 2.13 Synthetic outline for the trinuclear complex containing amine functionalities (**12**).

2.8.1 NMR spectroscopy

The stacked ^{1}H NMR spectra for complexes **11** and **12** (Figure 2.25) confirm the successful synthesis of the trinuclear complexes. The spectrum for complex **12** show a distinct singlet at 4.88 ppm assigned to H-7, which is observed in the spectrum of the mononuclear analogue (Figure 2.22a) at 4.75 ppm. Comparing the spectrum of the mononuclear analogues (**9** and **10**),

complexes **11** and **12** respectively were successfully synthesised, however, broadening and overlapping of proton signals in the aromatic region is observed for the trinuclear complexes. This is attributed to the size of the compounds due to slow rotation of these complexes in solution, leading to averaging of similar signals in similar environments on NMR timescale.

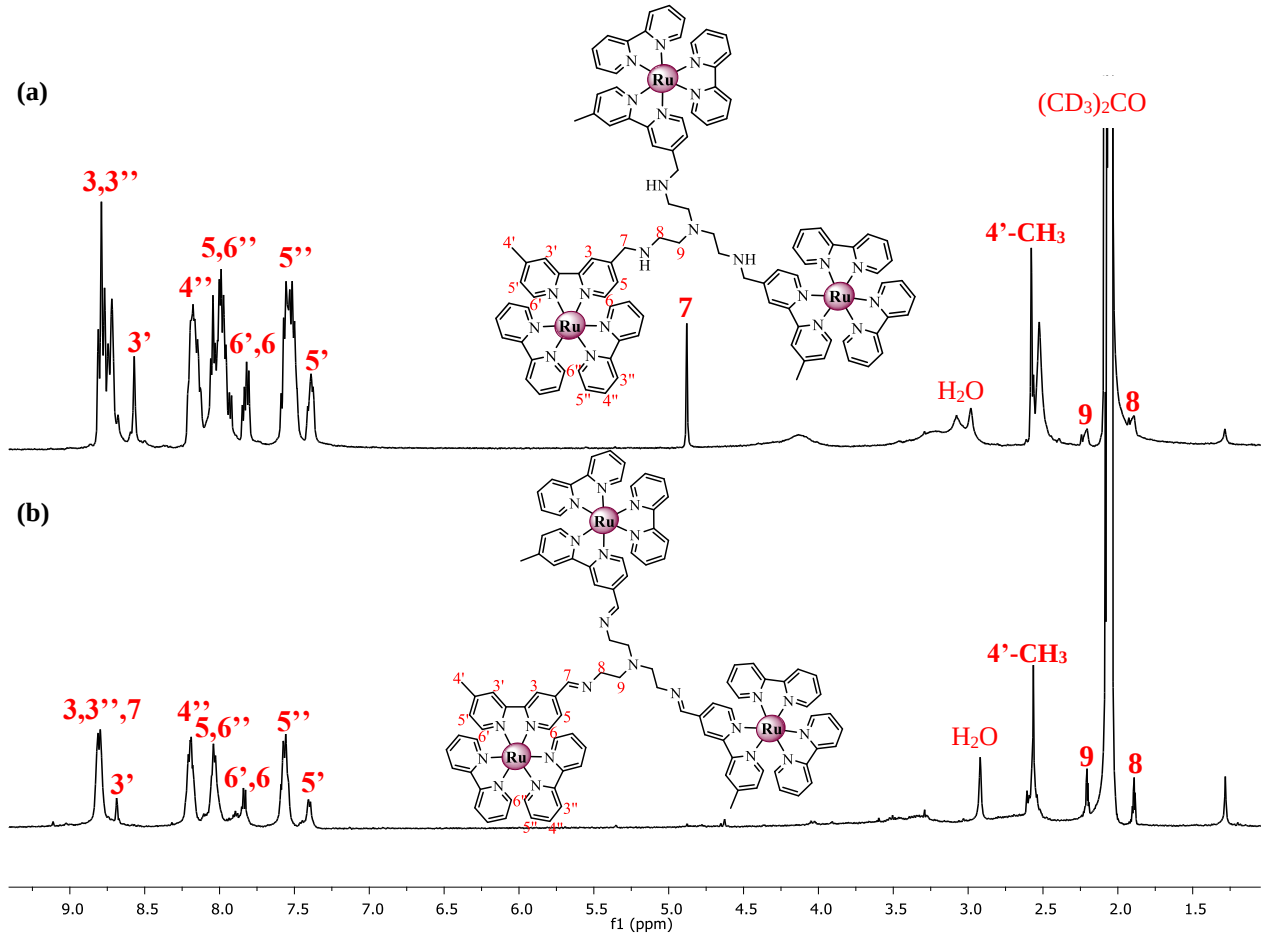

Figure 2.25 Stacked ^{1}H NMR spectra of trinuclear complexes (a) **12** and (b) **11** in $(CD_3)_2CO$.

2.8.2 Infrared (IR) spectroscopy

The obtained infrared spectra for complexes **11** and **12** (Figure 2.26) shows an absorption band at 1623 cm^{-1} for complex **11**, which is attributed to the imine functionality (C=N) of the complex. This absorption band is not observed in the spectrum of **12** further confirming the complete reduction of all imine bonds of ligand **4**.

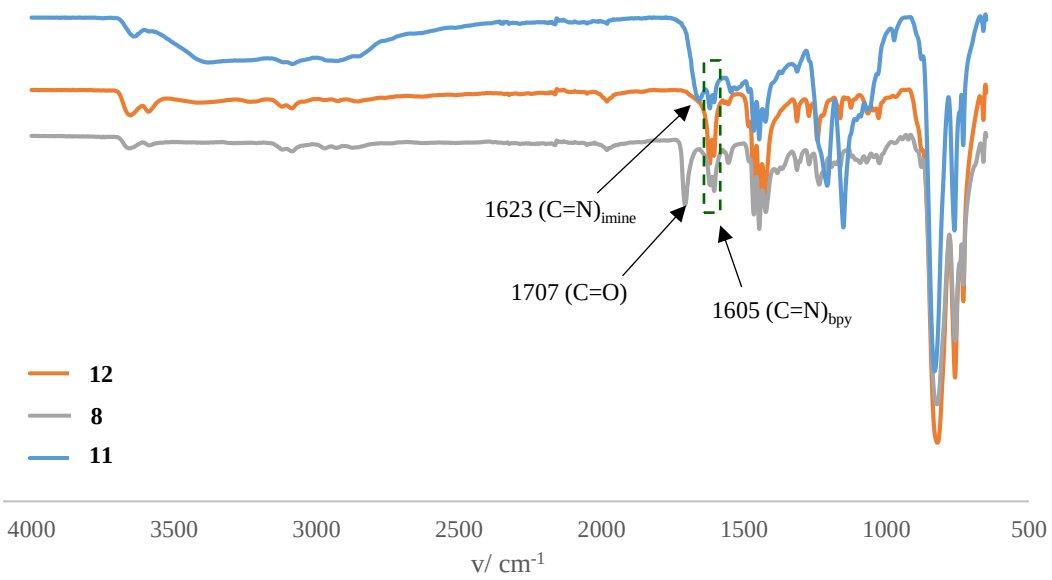

Figure 2.26 Stacked infrared spectra of complexes **8**, **11** and **12**.

2.8.3 Mass spectrometry

The data obtained from high resolution ESI-MS further confirmed the successful synthesis of complexes **11**. A base peak was observed at *m/z* = 306.5714 corresponding to the calculated mass of 306.4133 g/mol assigned to the $[M-6PF_6-CH_3]^{6+}$ ion.

2.9 Electronic absorption and photophysical properties for complexes 7-12

2.9.1 Electronic absorption spectroscopy

In addition to the discussed characterisation techniques used to confirm successful synthesis of the complexes (**7-12**), electronic absorption experiments were conducted to study the effects of ligand substituents on the photophysical properties and to determine the wavelengths of excitation suitable for application in photoredox catalysis for these complexes. The obtained electronic absorption spectra (Figure 2.27) for complexes **8-12** is comparable with that of the $[Ru(bpy)_3]^{2+}$ complex (**7**) and all complexes display an intense ligand centred absorption bands at 290 nm and this is assigned to the spin-allowed $\pi_L \rightarrow \pi_L^*$ transitions of the diimine. The low-energy absorption band at *ca.* 460 nm is assigned to the spin-allowed metal-to-ligand charge-transfer (^{1}MLCT) transitions from the d-orbitals of the metal to the π^* orbitals of the bipyridine. The assignment of this absorption band was made by comparison with the absorption spectrum of 2,2'-bipyridine (Appendix A, Figure A3). Interestingly, a slight red shift is observed for

complexes **9** and **11** relative to the parent $[Ru(bpy)_3]^{2+}$ complex (**7**), suggested to be due to the influence of the imine functionality on these complexes, which slightly lowers the π^* orbital of the ligand in turn decreasing the HOMO-LUMO energy gap hence the shift to longer wavelengths. The observed high-energy absorption bands at 250 nm are attributed to the $\pi_L \rightarrow \pi_L^*$ intraligand transitions (Appendix A, Figure A3).

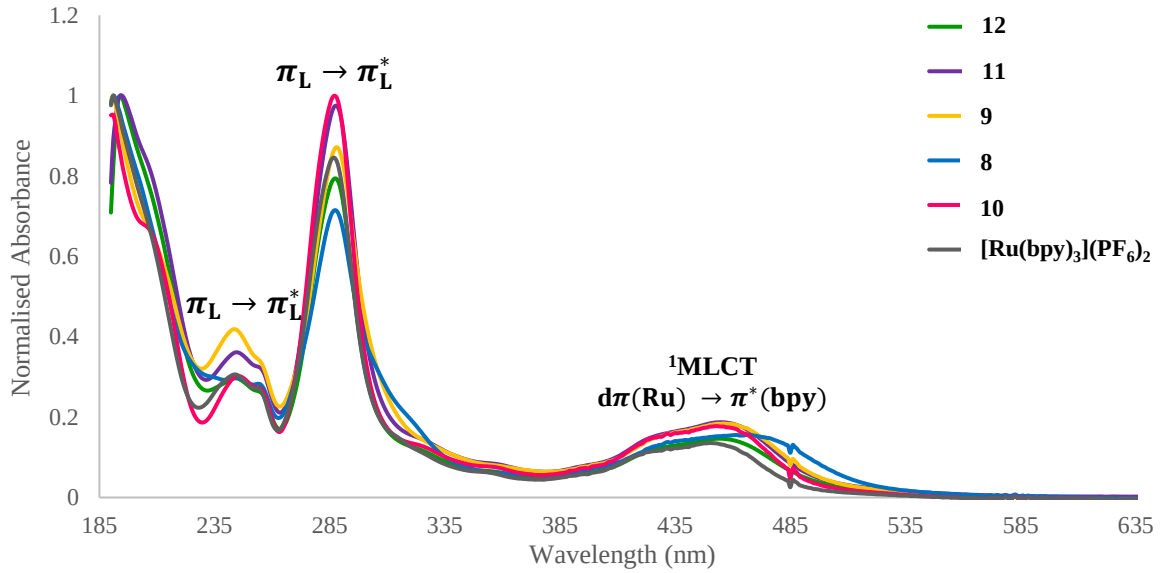

Figure 2.27 Electronic spectra for the ground state Ru(II) complexes (**8-12** and $[Ru(bpy)_3]^{2+}$) (1×10^{-5} *M*) in anhydrous acetonitrile.

2.9.2 Emission spectroscopy

Figure 2.28 show the emission spectra for complexes **8-12** and the prototypical $[Ru(bpy)_3]^{2+}$ complex (**7**) excited at λ_{ex} = 450 nm, a wavelength chosen based on the obtained electronic absorption spectra. In order to allow a direct comparison of the properties of both the mononuclear and trinuclear complexes, the concentrations of the complexes were adjusted to 1.0×10^{-5} *M*, that is, 1.0×10^{-5} *M* for mononuclear and 3.3×10^{-6} *M* for trinuclear complexes. The observed broad emission band in the 614−633 nm range for complexes **8-12** is comparable to that of the $[Ru(bpy)_3]^{2+}$ complex (**7**). This emission band is attributed to the lowest lying ^{3}MLCT excited-states following intersystem crossing from initial ^{1}MLCT excited-states that is observed in the absorption spectra. All ligand-modified complexes (**8-12**) were red shifted relative to the unfunctionalised prototypical complex, $[Ru(bpy)_3]^{2+}$ (**7**), with complex **9** containing an imine functionality being the most red shifted. The observed shift is consistent with that displayed in the absorption spectrum for this complex and is attributed to a lowered LUMO energy of the excited-state. This demonstrates the effects of introducing small

modifications on the ligands on the photophysical properties of these complexes, which was hypothesised earlier in this Chapter.

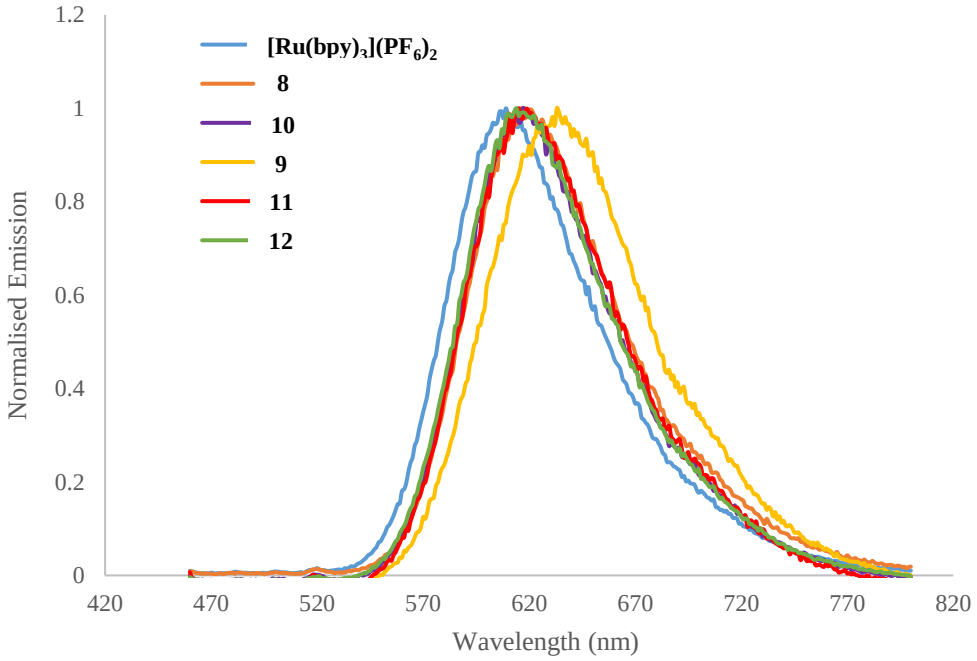

Figure 2.28 Emission spectra of Ru(II) complexes (**8**-**12** and $[Ru(bpy)_3]^{2+}$) (1×10^{-5} *M*) in anhydrous acetonitrile at room temperature. Excitation wavelength is 450 nm.

The Gibbs free energy was estimated by the difference in energy between the triplet excited-state (^{3}MLCT) and the ground-state of the complexes using the obtained emission data (Figure 2.29).[36]

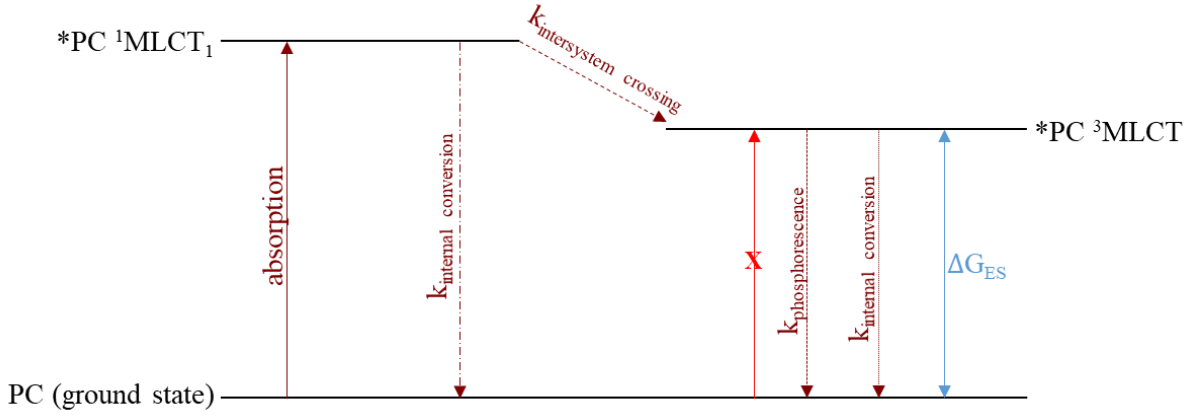

Figure 2.29 General depiction of a Jablonski diagram with the respective rate constants for the possible decay pathways.[36]

Table 2.1 summarises the photophysical data and the Gibbs free energy of the excited-state above the ground-state (ΔG_{ES}) for complexes **8-12** and $[Ru(bpy)_3]^{2+}$ (**7**). Comparing the obtained Gibbs free energy of complex **9** with $[Ru(bpy)_3]^{2+}$ (**7**) (Table 2.1), a decrease in energy is observed, which corresponds to a small energy gap between the ^{3}MLCT excited- and ground-state.

Table 2.1 Photophysical properties for Ru(II) complexes (**8-12** and $[Ru(bpy)_3]^{2+}$).[a]

Complexes	$\lambda_{abs(MLCT)}$ (nm) (ε_{MLCT}/M^{-1} cm^{-1})	λ_{em} (nm)	ΔG_{ES} (eV)
$[Ru(bpy)_3]^{2+}$	454 (18 691)	609	2.04
8	459 (19 181)	616	2.02
9	460 (27 292)	633	1.96
10	457 (16 313)	616	2.02
11	460 (19 151)	615	2.02
12	458 (20 230)	614	2.02

[a]Data acquired in CH_3CN.

2.10 Electrochemical studies of mono- and tri-nuclear complexes (7-12)

The electrochemical properties for complexes **8-12** and $[Ru(bpy)_3]^{2+}$ (**7**) in a 0.2M $TBAPF_6$ / CH_3CN solution were examined by cyclic voltammetry (Figure 2.30). The voltammograms display reversible $Ru^{3+/2+}$ redox couples at positive potential with $E_{1/2}$ values ranging from 0.878 to 0.956 V (vs Ag/Ag^+) and three ligand-base reductions at negative potentials. The reversibility of these redox processes plays an important role in photoredox catalysis since the catalyst must be stable enough in its oxidised or reduced form in order to be regenerated over the course of the catalytic process.

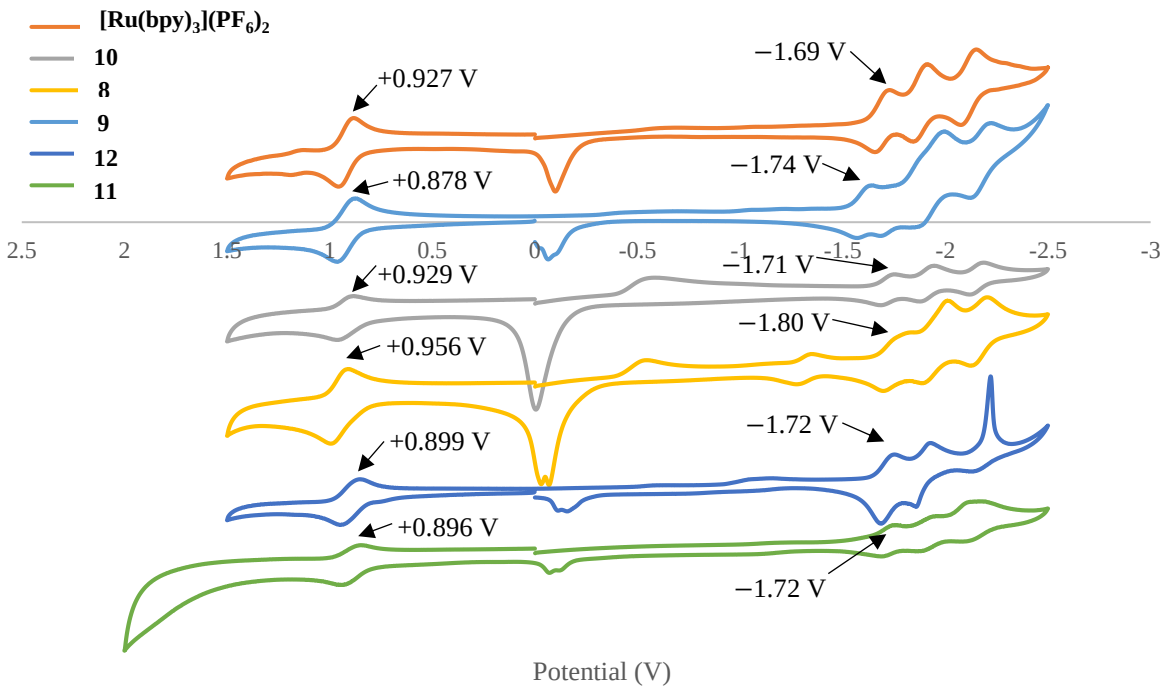

Figure 2.30 Cyclic voltammograms for complexes **8-12** and $[Ru(bpy)_3]^{2+}$ $TBAPF_6/CH_3CN$ electrolyte at 25℃ with a glassy carbon working electrode, Pt-wire counter electrode, $Ag/AgNO_3$ reference electrode at a scan rate of 100mV/s.

The prototypical $[Ru(bpy)_3]^{2+}$ complex (**7**) produced an oxidation potential of +0.927 V (vs Ag/Ag^+) (Figure 2.30). Upon substitution at the 4-position with an aldehyde group (**8**), a cathodic shift of 29 mV is observed (Figure 2.30). This can be attributed to a relatively stronger electron-withdrawing effect of the aldehyde group compared to the unsubstituted $[Ru(bpy)_3]^{2+}$ complex (**7**). Upon functionalization of the aldehyde to an imine bearing a propyl chain (**9**), an anodic shift is observed (Figure 2.30), relative to the parent complex $[Ru(bpy)_3]^{2+}$, at a potential of +0.878 V vs Ag/Ag^+ suggesting a stronger electron-donating strength of the imine relative to the aldehyde functionality. Furthermore, the voltammogram obtained for **10** show a larger anodic shift of 51 mV relative to complex **9** (Figure 2.30). This shift is due to the stronger electron-donating ability of the imine relative to the amine functionality on the ligand, resulting in an easier oxidation on this complex (**9**).

Three reduction potentials (−1.69 V, −1.87 and −2.10 V vs Ag/Ag^+) for $[Ru(bpy)_3]^{2+}$ (**7**) are observed (Table 2.2), suggesting that consecutive one-electron reduction events occur for the three ligands.[37] Interestingly, the voltammograms obtained for complexes **8** and **9** display

additional reduction peaks at −1.32 V and *ca.* −1.59 V vs Ag/Ag^+, respectively. This is likely due to the reduction of the aldehyde and imine functionality of the ligands. The observed redox potentials for the prototypical $[Ru(bpy)_3]^{2+}$ complex (**7**) are comparable with those reported in literature with a difference of only 0.01V for the $Ru^{3+/2+}$ redox couple.[4]

Furthermore, the excited-state redox potentials were determined by relating the Gibbs free excitation energy with the energy corresponding to the to the photoluminescence maximum of the complexes using equation 2.1 and 2.2 shown earlier.[12,33] The excited-state reduction potential for the complexes ($Ru^{2+*/+}$) was determined using the first reduction event, which is the catalytically relevant reduction potential for single-electron transfer (SET). From the obtained data (Table 2.2), the photoexcited $[Ru(bpy)_3]^{2+*}$ complex (**7**) has the most positive reduction potential +0.350 V vs Ag/Ag^+ suggesting that this complex is a stronger oxidant than complexes **8-12**. Complex **8**, containing a relatively electron-withdrawing aldehyde substituent, exhibit the least positive excited state reduction potential thus will require a stronger reducing agent to quench.

Table 2.2 Half-wave potentials for the ground- and excited-state Ru(II) complexes (**8-12** and $[Ru(bpy)_3]^{2+}$).[a]

Complex	$E_{1/2}$ **(V) vs** Ag/Ag^+					
	E_{Ox}	$^*E_{Ox}$[b]	E_{Red1}	E_{Red2}	E_{Red3}	$^*E_{Red}$[c]
$[Ru(bpy)_3]^{2+}$	+0.927	−1.11	−1.69	−1.87	−2.10	+0.350
8	+0.956	−1.06	−1.80	−1.98	−2.20	+0.220
9	+0.878	−1.08	−1.74	−1.91	−2.15	+0.220
10	+0.929	−1.08	−1.71	−1.90	−2.10	+0.310
11	+0.896	−1.12	−1.72	−1.91	−2.12	+0.300
12	+0.899	−1.12	−1.72	−1.89	−2.17	+0.300

[a] A $TBAPF_6/CH_3CN$ solution matching the complex counter-anion was used as a supporting electrolyte. [b] $Ru^{3+/2+*} = Ru^{3+/2+} - \Delta G_{ES}$. [c] $Ru^{2+*/+} = Ru^{3+/2+} - \Delta G_{ES}$. Potentials were corrected to Ag/Ag^+ through an external ferrocene reference.

2.11 Summary

Bipyridyl monomeric and trimeric ligands **1-5** and their corresponding ruthenium(II) bipyridyl complexes (**8-12**) were successfully synthesised and characterised by ^{1}H NMR, ^{13}C{^{1}H} NMR, infrared spectroscopy and mass spectrometry. The spectral data displayed interesting signals for protons H-3/3' and H-6/6', where the signals assigned to H-3/3' appeared upfield relative to H-6/6' for the free ligands. However, upon coordination of the ligands to the ruthenium metal ion, protons H-3/3' were shifted downfield relative to signals assigned to H-6/6' and this was attributed to the steric strain experienced by protons H-3/3' since the ligand assumes a *cis* conformation upon complexation. The infrared spectra displayed a shift to higher frequency for all complexes upon coordination of the bipyridyl ligands to the ruthenium metal ion, which is suggested to be due to the presence of a dicationic metal ion. Furthermore, electrochemical, electronic absorption and emission studies for the complexes were conducted and the collected data displayed the effects of the substituents on the bipyridine ligands. All the ligand-modified complexes (**8-12**) exhibited red shifted emission spectra relative to the prototypical complex and this emission band is attributed to the transition from the ^{3}MLCT to the ground state. Complex **9** was the most red shifted and this is attributed to the effects of the imine substituent on the ligand of this complex, which lowered the LUMO energy level of the excited-state. The obtained ground-state electrochemical data revealed the effects of ligand modifications on the complexes, where the complex containing a relatively electron-withdrawing substituent (**8**) displayed a cathodic shift while complexes **9, 11** and **12** displayed the greatest anodic shift relative to **8**. The known complex, $[Ru(bpy)_3]^{2+}$, displayed the most positive excited-state reduction potential, therefore, it is expected to be a more powerful oxidant for the photocatalytic reactions. The obtained excited-state reduction potentials for complexes **10-12** were comparable to that of the known complex thus displaying promising photocatalytic activity. The complexes (**8-12**) will then be evaluated as photoredox catalysts in the hydrothiolation reaction of olefins and the catalytic performance of these complexes will be compared to that of the prototypical $[Ru(bpy)_3]^{2+}$ complex (**7**), and the results of these studies are discussed in the following Chapter of this thesis.

2.12 References

1. V. Balzani, A. Juris, M. Venturi, S. Campagna and S. Serroni, *Chem. Rev.*, 1996, **96**, 759-834.
2. A. Juris, V. Balzani, F. Barigelletti, S. Campagna, P. L. Belser and A. V. von Zelewsky, *Coord. Chem. Rev.*, 1988, **84**, 85-277.
3. P. A. Anderson, G. F. Strouse, J. A. Treadway, F. R. Keene and T. J. Meyer, *Inorg. Chem.*, 1994, **33**, 3863-3864.
4. D. M. Arias-Rotondo and J. K. McCusker, *Chem. Soc. Rev.*, 2016, **45**, 5803-5820.
5. C. Lopez, J. C. Moutet and E. Saint-Aman, *J. Chem. Soc. Faraday Trans.*, 1996, **92**, 1527-1532.
6. F. Szemes, D. Hesek, Z. Chen, S. W. Dent, M. G. Drew, A. J. Goulden and J. S. Weightman, *Inorg. Chem.*, 1996, **35**, 5868-5879.
7. S. Verma, P. N. Tripathi and R. P. Singh, *Int. Multidiscip. Res. J.*, 2012, **2**.
8. K. Nakamaru, *Bull. Chem. Soc. Jpn.*, 1982, **55**, 2697-2705.
9. M. Waki, S. Shirai, K. I. Yamanaka, Y. Maegawa and S. Inagaki, *RSC Adv.*, 2020, **10**, 13960-13967.
10. K. Kalyanasundaram and M. K. Nazeeruddin, *Chem. Phys. Lett.*, 1992, **193**, 292-297.
11. G. J. Barbante, C. F. Hogan, D. J. Wilson, N. A. Lewcenko, F. M. Pfeffer, N. W. Barnett and P. S. Francis, *Analyst*, 2011, **136**, 1329-1338.
12. D. L. Ashford, M. K. Brennaman, R. J. Brown, S. Keinan, J. J. Concepcion, J. M. Papanikolas and T. J. Meyer, *Inorg. Chem.*, 2015, **54**, 460-469.
13. M. Sun, C. Wang, C. Y. Sun, M. Zhang, X. L. Wang and Z. M. Su, *J. Catal.*, 2020, **385**, 70-75.
14. C. He, S. Yu, S. Ma and F. Cheng, *Transit. Met. Chem.*, 2019, **44**, 515-524.
15. T. C. Motley, L. Troian-Gautier, M. K. Brennaman and G. J. Meyer, *Inorg. Chem.*, 2017, **56**, 13579-13592.
16. D. Hesek, Y. Inoue, S. R. Everitt, H. Ishida, M. Kunieda and M. G. Drew, *Inorg. Chem.*, 2000, **39**, 308-316.
17. B. M. Peek, G. T. Ross, S. W. Edwards, G. J. Meyer, T. J. Meyer and B. W. Erickson, *Int. J. of Pept. Protein Res.*, 1991, **38**, 114-123.
18. D. P. Kjell, B. J. Slattery and M. J. Semo, *J. Org. Chem.*, 1999, **64**, 5722-5724.
19. F. Elytle, L. M. Petrosky and L. R. Carlson, L. R., *Anal. Chim. Acta*, 1971, **57**, 239-247.

20. P. Govender, S. Pai, U. Schatzschneider and G. S Smith, *Inorg. Chem.*, 2013, **52**, 5470-5478.
21. S. Yao, A. M. Jones, J. Du, R. K. Jackson, J. O. Massing, D. P. Kennedy and W. R. Seitz, *Analyst*, 2012, **137**, 4734-4741.
22. N. E. Borisova, M. D. Reshetova and Y. A. Ustynyuk, *Chem. Rev.*, 2007, **107**, 46-79.
23. C. H. Lin, H. C. Kao, C. J. Hsu and W. J. Wang, *J. Chin. Chem. Soc.*, 2010, **57**, 1167-1171.
24. S. Castellano, H. Günther and S. Ebersole, *J. Phys. Chem.*, 1965, **69**, 4166-4176.
25. Y. Z. Yousif and J. M. Al-Rawi, *Polyhedron*, 1992, **11**, 1411-1418.
26. B. Z. Shan, Q. Zhao, N. Goswami, D. M. Eichhorn and D. P. Rillema, *Coord. Chem. Rev.*, 2001, **211**, 117-144.
27. M. J. Li, C. Q. Zhan, M. J. Nie, G. N. Chen and X. Chen, *J. Inorg. Biochem.*, 2011, **105**, 420-425.
28. J. Karges, F. Heinemann, F. Maschietto, M. Patra, O. Blacque, I. Ciofini and G. Gasser, *Bioorg. Med. Chem.*, 2019, **27**, 2666-2675.
29. K. O. Hwang, Y. Yakura, F. S. Ohuchi and T. Sasaki, *Mater. Sci. Eng. C*, 1995, **3**, 137-141.
30. S. T. Howard, *J. Am. Chem. Soc.*, 1996, **118**, 10269-10274.
31. S. Zahn, W. Reckien, B. Kirchner, H. Staats, J. Matthey and A. Lützen, *Chem. Eur. J.*, 2009, **15**, 2572-2580.
32. M. D. Pratt and P. D. Beer, *Tetrahedron*, 2004, **60**, 11227-11238.
33. E. P. Farney, S. J. Chapman, W. B. Swords, M. D. Torelli, R. J. Hamers and T. P. Yoon, *J. Am. Chem. Soc.*, 2019, **141**, 6385-6391.
34. C. C. Scarborough and K. Wieghardt, *Inorg. Chem.*, 2011, **50**, 9773-9793.
35. A. M. Cancelliere, F. Puntoriero, S. Serroni, S. Campagna, Y. Tamaki, D. Saito and O. Ishitani, *Chem. Sci.*, 2020, **11**, 1556-1563.
36. J. W. Tucker and C. R. Stephenson, *J. Org. Chem.*,2012, **77**, 1617-1622.
37. A. Ito, N. Kobayashi and Y. Teki, *Inorg. Chem.*, 2017, **56**, 3794-3808.

Chapter 3

Evaluation of ligand-modified ruthenium(II) complexes as visible-light photoredox catalysts for the hydrothiolation reaction of olefins

3.1 Introduction

The hydrothiolation reaction of alkenes is a coupling reaction between an alkene and a thiol in the presence of a photocatalyst or initiator to afford thioethers as hydrothiolated products. (Scheme 3.1).[1,2] Alkene hydrothiolation (thiol-ene) reactions have been extensively studied over the last century.[3-6] However, it is only recently that the efficient and selective transformation of alkenes into sulfur-containing compounds through transition-metal catalysis has been developed.[7-10] This development has been driven by the increasing prevalence of C–S bond-containing compounds within the pharmaceutical industry, natural products, bioconjugate and polymer chemistry.[11-14]

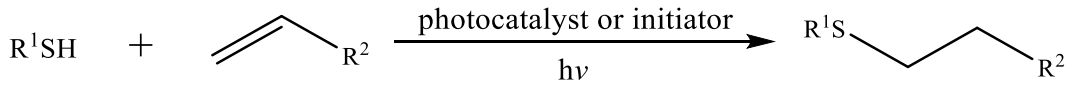

Scheme 3.1 Outline for the radical-mediated thiol-ene reaction with anti-Markovnikov selectivity.[15]

This organic transformation can result in two types of products namely, branched and/or linear hydrothiolated products formed *via* the Markovnikov and anti-Markovnikov addition with respect to the C–S bond formation, respectively.[13] The radical-mediated thiol-ene reaction has been reported to proceed *via* the anti-Markovnikov addition of the thiol to the alkene resulting in the regioselective formation of the linear product.[16,17] Arnold and co-workers rationalised this observation by means of the radical stability of the resultant distonic radical cation.[16,17] The authors proposed that the more substituted radical is likely to be more sterically crowded and the thiol radical adds to the less substituted position of the alkene resulting in the anti-Markovnikov product.[16,17]

Although thiols and alkenes are typically unreactive toward each other, their interaction can be brought about by various organic or organometallic initiators leading to a radical addition

reaction.[18] However, traditional methods of initiating this type of reaction utilised harsh reaction conditions such as thermal or UV light and often the thiol would rapidly deactivate the transition metal catalysts.[19-22] In efforts to circumvent these drawbacks, Yoon and co-workers designed a photoredox-catalysed hydrothiolation reaction of alkenes that is initiated by visible-light (blue LED) and $[Ru(bpz)_3](PF_6)_2$ as a photocatalyst.[15] This photocatalytic reaction proceeded efficiently under comparably mild reaction conditions, generating reactive thiyl radicals that can add to an alkene with anti-Markovnikov selectivity.[15,23] However, when the reaction was conducted with the well-known $[Ru(bpy)_3]^{2+}$ complex, it was found to be an inefficient photoredox catalyst under these conditions. Matsuda *et al*. investigated the quenching step of this complex by thiols and observed that the photoexcited $[Ru(bpy)_3]^{2+}$ complex is not significantly quenched upon treatment with thiols, particularly with aliphatic thiols, due to a kinetic barrier.[24,25] Therefore, Tyson *et al*. later explored the use of a redox mediator, which improved the photocatalytic efficiency by mediating the electron transfer between the photoexcited catalyst and the thiol.[25] For this reason, a redox mediator was utilised for this study since the ruthenium(II) complexes evaluated were based on the bipyridyl ligand.

Scheme 3.2 illustrates the reaction mechanism proposed by Tyson *et al.* for the photocatalytic thiol-ene coupling reaction conducted in the presence of a redox mediator, *p*-toluidine.[25,26] Upon photoexcitation of the ruthenium(II) complex, the redox mediator undergoes single-electron transfer (SET) with the excited photocatalyst thus quenching the excited-state and subsequently resulting in an aniline radical cation that is capable of activating a thiol. The aniline radical cation then reacts with the thiol substrate to form the chain-propagating thiyl radical intermediate that consequently adds to the alkene with an anti-Markovnikov selectivity.[25] The formed thiyl radical species can also undergo a competing radical termination step resulting in the disulfide product (Scheme 3.2, RSSR).[27] The formation of the disulfide product consumes the generated thiyl radical needed for the thiol-ene addition step, leading to lower yield. From the reaction mechanism, it is observed that the ground-state redox potentials relate to the catalyst regeneration while the excited-state redox potentials are related to the reductive quenching step of the photoexcited catalyst.

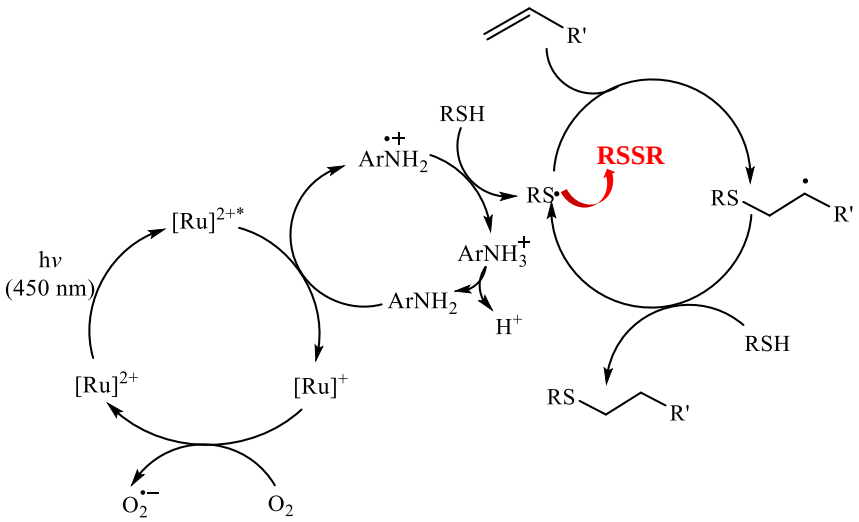

Scheme 3.2 Proposed reaction mechanism for the formation of radical species in the photocatalytic addition of thiols to alkenes.[25,26]

Despite previous reports on radical-mediated thiol-ene reaction under irradiation of visible light, few examples of ligand-modified multinuclear photoredox catalysts, for this reaction, have been reported. This has motivated the evaluation of ligand-modified trinuclear ruthenium bipyridyl complexes as potential photoredox catalysts for this olefin transformation reaction.

3.2 Results and discussion

We initiated our photocatalytic studies by examining the reaction between thiophenol and styrene using the prototypical $[Ru(bpy)_3](PF_6)_2$ complex (Figure 3.1, **7**) as a photoredox catalyst and *p*-toluidine as a redox mediator. All the other photocatalytic thiol-ene reactions carried out in the presence of the ligand-modified complexes (Figure 3.1, **8-12**) were benchmarked against this prototypical complex (**7**). The obtained yields varied depending on the substrates used. The $[Ru(bpy)_3](PF_6)_2$ complex (Figure 3.1, **7**) performed better in the presence of an aromatic thiol relative to the modified mononuclear complexes (**8-10**). In the presence of an aliphatic thiol, the yields generally improved upon using the modified complexes **8-12** (Figure 3.1). The conditions used in this study were based on previously reported conditions for the photoredox-catalysed radical thiol-ene reaction, where the reaction mixture was irradiated under blue LED light at room temperature.[15] Furthermore, this reaction was chosen as a model reaction since it has been shown to proceed fairly efficiently under similar photocatalytic conditions.

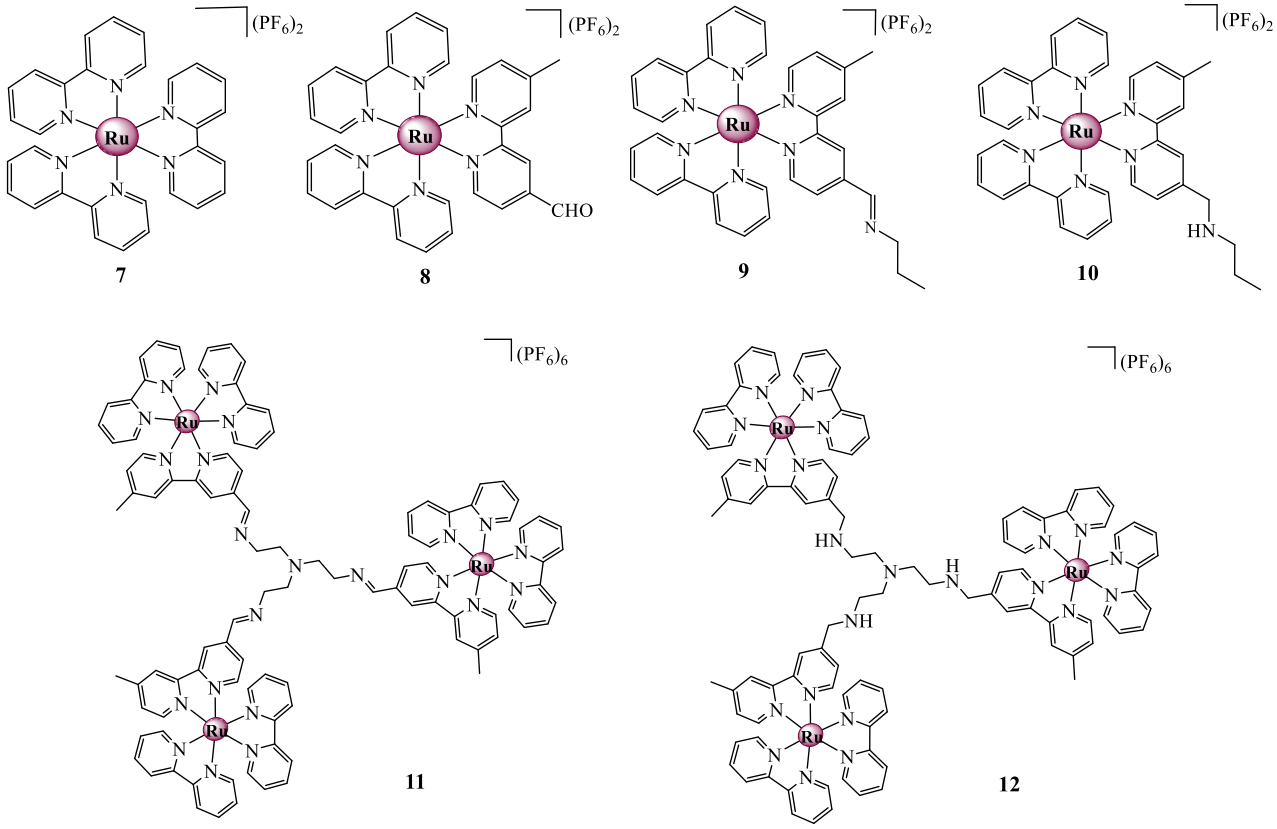

Figure 3.1 Ru(II) complexes evaluated as photoredox catalysts for thiol-ene coupling reactions.

3.2.1 Visible light-mediated photoredox catalysed reaction of thiophenol with styrene

Scheme 3.3 outlines the reaction and associated conditions for the photoredox-catalysed radical thiol-ene reaction of thiophenol with styrene under blue LED irradiation at room temperature (Figure 3.2). The reactions were monitored by thin layer chromatography (TLC) and the isolated product for complex **7** was obtained in moderate yield (54%). The reaction was successfully carried out in duplicate and the product was purified by column chromatography, dried *in vacuo* and confirmed by ^{1}H NMR spectroscopy.

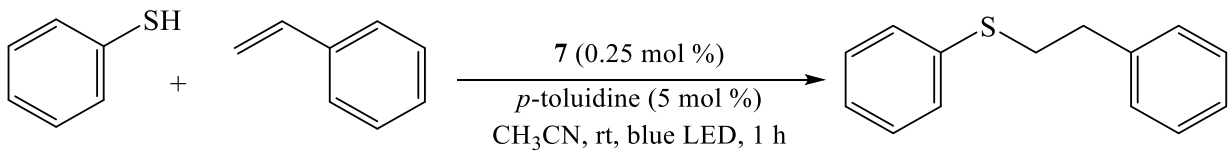

Scheme 3.3 Reaction scheme for the photoredox catalytic reaction of thiophenol with styrene.

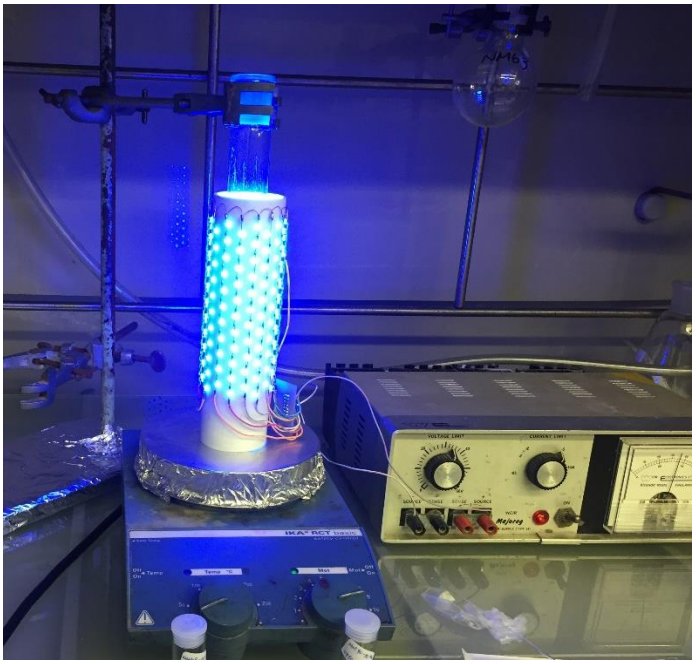

Figure 3.2 Pictorial representation of the photoredox catalysis experimental setup.

The stacked ^{1}H NMR spectra (Figure 3.3) show the substrates and thioether product and confirm the success of the photocatalytic reaction. The singlet at 3.45 ppm assigned to H-1 of thiophenol (Figure 3.3b) as well as the doublet of doublets at 6.71 ppm (^{3}J = 17.6 Hz, ^{3}J = 10.9 Hz) assigned to H-3 in the spectrum of styrene (Figure 3.3c), are not observed in the spectrum of the isolated product (Figure 3.3a). Additionally, the two doublets at 5.74 (^{3}J = 17.6 Hz) and 5.23 ppm (^{3}J = 10.9 Hz) assigned to H-1 and H-2 of styrene respectively, are not observed in the spectrum of the product (Figure 3.3a), confirming the successful coupling of the substrates. The two new signals at 3.19 and 2.94 ppm assigned to H-5 and H-4 each integrating for two protons suggests that the addition step of the thiyl radical to the styrene took place and the obtained spectrum is for the anti-Markovnikov thioether product. The observed chemical shift values are in agreement with those previously reported in the literature.[15]

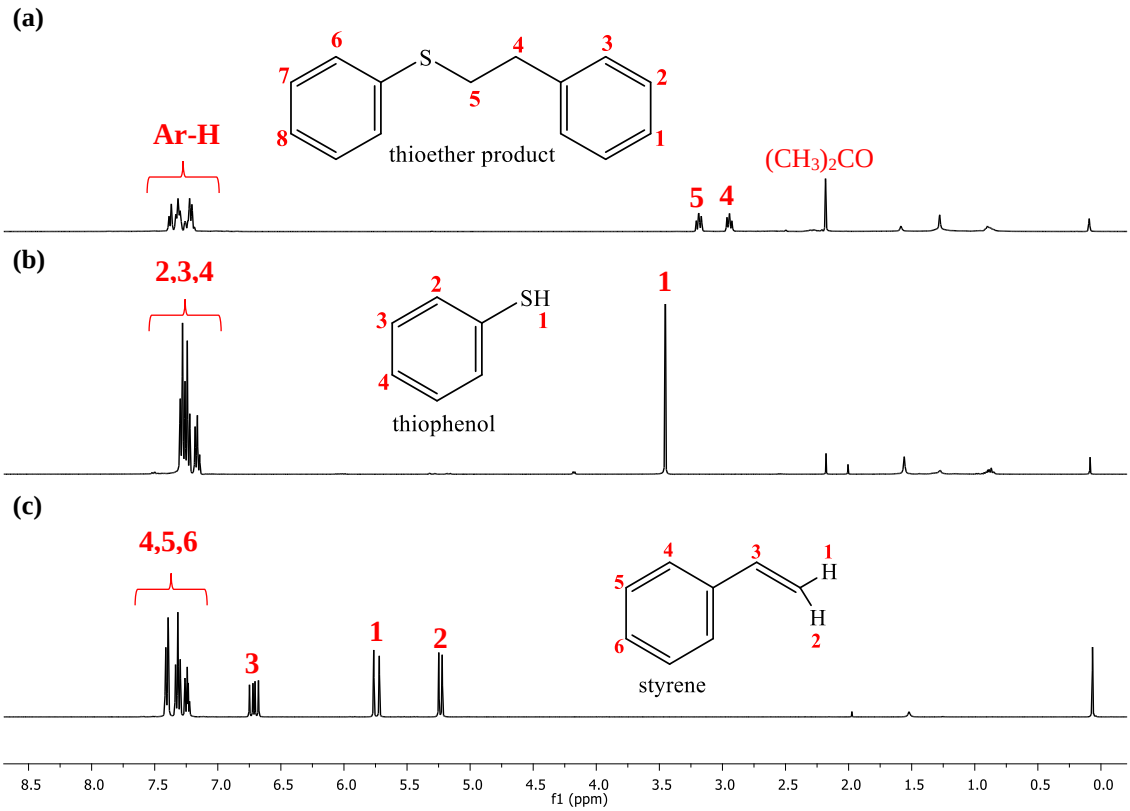

Figure 3.3 Stacked ^{1}H NMR spectra of (a) isolated product (b) thiophenol and (c) styrene in $CDCl_3$.

The photocatalysed reaction between thiophenol and styrene was successfully carried out with the $[Ru(bpy)_3](PF_6)_2$ complex (**7**), resulting in a moderate yield (54%) of the thioether product (Table 3.1, entry 1). The remaining synthesised complexes (**8-12**) were also evaluated as photoredox catalysts in this thiol-ene coupling reaction under analogous conditions previously described, resulting in low to good yields.[15] Table 3.1 show the percentage yields of the isolated anti-Markovnikov thioether product for each evaluated photoredox catalyst (**7-12**). It is observed that the yields, for complexes **7-12**, ranged from low to good and this can be attributed to the competing radical-radical thiyl homocoupling leading to the disulfide product, which is common for more acidic thiols.[1,27,28] The reaction conducted with complex **7** resulted in the highest yield (entry 1) of the product relative to those carried out in the presence of ligand-modified mononuclear complexes **8-10** (entries 5-7). Modifying the properties of the complexes by introducing relatively electron-withdrawing or electron-donating substituents on the bipyridine ligands is expected to modify the reactivity of the photocatalyst. However, the functionalised mononuclear complexes (**8-10**) resulted in lower yields for this reaction (Table 3.1, entries 5-7). This was likely due to the weaker oxidising ability of the ligand-modified

mononuclear complexes (**8-10**) (ranging from $E_{red\ (2+*/+)}$ = +0.220 V vs Ag/Ag^+ to $E_{red\ (2+*/+)}$ = +0.310 V vs Ag/Ag^+) relative to complex **7** ($E_{red\ (2+*/+)}$ = +0.350 V vs Ag/Ag^+), resulting in complex **7** being a more potent oxidising mononuclear catalyst and readily quenched by the thiophenol.

Control reactions were also carried out (entries 2-4) and it was observed that a background thiol-ene reaction occurred in the absence of the photoredox catalyst (entry 2). However, the obtained yield was significantly lower (6%) in the absence of the photocatalyst (entry 2) than in the presence of catalyst **7** (54%). In the absence of the redox mediator (entry 3), the isolated yield was slightly higher (11%) than that carried out in the absence of the photocatalyst (entry 2) but lower in comparison to the yield obtained in the presence of the prototypical photocatalyst precursor **7** (entry 1). A similar trend was observed in the absence of the light source (entry 4), where the isolated yield was significantly lower than for photocatalyst **7** (entry 1). These control reactions (entries 1-4) confirm that the redox mediator, the photocatalyst and the light source all play an important role in promoting the reaction, and that the reaction is not independently promoted by the photocatalyst or by irradiation with blue LED light or the *p*-toluidine alone.

Table 3.1 Isolated yields from the visible-light photoredox-catalysed thiol-ene reaction of thiophenol with styrene using complexes **7-12**.

Entry	Photoredox catalyst	% Yield[a]
1	**7**	54
2	No catalyst	6
3	**7** (no *p*-toluidine)	11
4	**7** (no light source)	12
5	**8**	24
6	**9**	8
7	**10**	22
8	**11**	26
9	**12**	73

[a]Isolated yields are the average of two reproducible experiments, which were comparable with known compound.

The mononuclear complex containing an imine functional group (**9**) gave the lowest yield (8%) of coupled product (Table 3.1, entry 6) and this is suggested to be due to various factors such as compatibility of the redox potentials of the thiophenol with the photoexcited complex **9**, consequently resulting in poor quenching of the excited-state. The relatively small energy gap of complex **9** (1.96 eV) is possibly leading to rapid decay of the excited-state back to the ground-state and causing the catalyst to have less time to engage in SET with the thiol. Comparing the obtained yield for complex **9** (entry 6) with that of complex **10** (entry 7), it is observed that the yield for the thioether product improved upon reducing the imine on the bipyridyl ligand (8%) to an amine (22%). This is attributed to the oxidising strength of the photoexcited catalyst **10** which is more positive ($E_{red\ (2+*/+)}$ = +0.310 V vs Ag/Ag^+) than that of the photoexcited catalyst **9** ($E_{red\ (2+*/+)}$ = +0.220 V vs Ag/Ag^+), making the amine-functionalised complex (**10**) a better photoredox catalyst for this reaction than the imine-functionalised complex (**9**). Moreover, the excited-state reduction potentials for complexes **8** and **9** are comparable ($E_{red\ (2+*/+)}$ = +0.220 V vs Ag/Ag^+ for both complexes) so the reactivity for these complexes is expected to be similar since their oxidising potential is comparable. Therefore, the low yield for photocatalyst **9** (entry 6) can also be due to a short-lived excited-state lifetime.

Remarkably, the reactions carried out in the presence of the trinuclear complexes (**11** and **12**) ($E_{red\ (2+*/+)}$ = +0.300 V vs Ag/Ag^+) resulted in almost a 3-fold increase in isolated yields (Table 3.1, entries 8 and 9) in comparison with their respective mononuclear analogues (**9** and **10**). The catalyst loading for these complexes was adjusted accordingly to allow direct comparison with their mononuclear analogues. Comparing the obtained yields for the mononuclear imine-containing catalyst **9** and the trinuclear catalyst **11** (entries 6 and 8), an increase from 8% to 26% is observed. A similar trend is observed between the obtained yields for the amine-containing mononuclear catalyst **10** and trinuclear catalyst **12** (entries 7 and 9), demonstrating the advantages of a multinuclear photocatalyst. This observed increase is potentially due to the presence of several photoactive centres causing a multi-electron transfer in a single step, which is common for ruthenium(II) multinuclear complexes.[29,30]

Similarly, the trend observed between the mononuclear complexes **9** and **10** (Table 3.1, entries 6 and 7) is also observed between the trinuclear complexes **11** and **12** (entries 8 and 9). The complex containing imine functionalities (**11**) resulted in lower yield (26%) than the complex containing amine functionalities (**12**) (73%). The excited-state reduction potential ($E_{red\ (2+*/+)}$ =

+0.300 V vs Ag/Ag^+) and energy gap between the triplet excited-state and the ground-state for this complex (2.02 eV) is comparable to that of **12**. Therefore, the lower yield obtained using complex **11** may be ascribed to decomposition of complex **11** under the catalytic conditions, which creates a relatively acidic environment due to the presence of thiophenol, resulting in the imine bond cleavage of the complex and breaking the multinuclearity of the complex. Imine bond cleavage results in the formation of the aldehyde-functionalised complex (**8**) and this could possibly promote the reaction. This becomes evident by the similar yields for the reaction carried out in the presence of the aldehyde-functionalised photocatalyst **8** (Table 3.1, entry 5) and the reaction conducted with complex **11** (Table 3.1, entry 8).

3.2.2 Visible light-mediated photoredox catalysed reaction of 1-butanethiol with styrene

The effect of substrate compatibility in the thiol-ene reaction was examined by replacing the aromatic thiol with an aliphatic thiol, 1-butanethiol (Scheme 3.4). The reaction was carried out using similar conditions as reported for the reaction between thiophenol and styrene (Scheme 3.3). The product of this reaction was purified by column chromatography, dried *in vacuo* and confirmed by ^{1}H NMR spectroscopy.

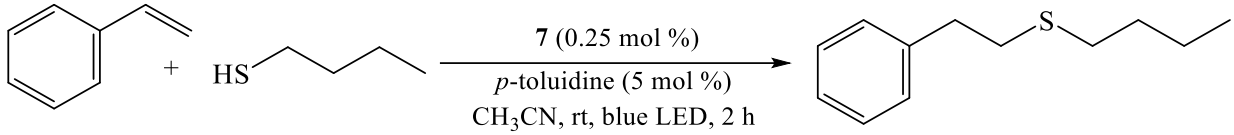

Scheme 3.4 Reaction scheme for the photoredox catalytic reaction of 1-butanethiol with styrene.

The stacked ^{1}H NMR spectra (Figure 3.4) of the isolated product and starting materials confirm the success of the radical coupling reaction between styrene and 1-butanethiol to afford the anti-Markovnikov product. The observed aliphatic proton signals at 0.91 (^3J = 7.3 Hz), 1.39 (^3J = 14.5 Hz, ^3J = 7.3 Hz) and 1.58 ppm (^3J = 15.1 Hz, ^3J = 7.5 Hz) assigned to H-1, H-2 and H-3 respectively (Figure 3.4b) as well as the absence of the signal at 1.31 ppm previously assigned to H-5 of 1-butanethiol, confirms the formation of the linear thioether. Furthermore, the proton signals assigned to the vinyl protons (H-1, H-2, H-3) of styrene (Figure 3.4c) at 5.74, 5.23 and 6.71 ppm are not observed in the spectrum of the isolated product. The relative proton ratios in the aliphatic and aromatic region suggests that the alkene was successfully coupled with the thiol.

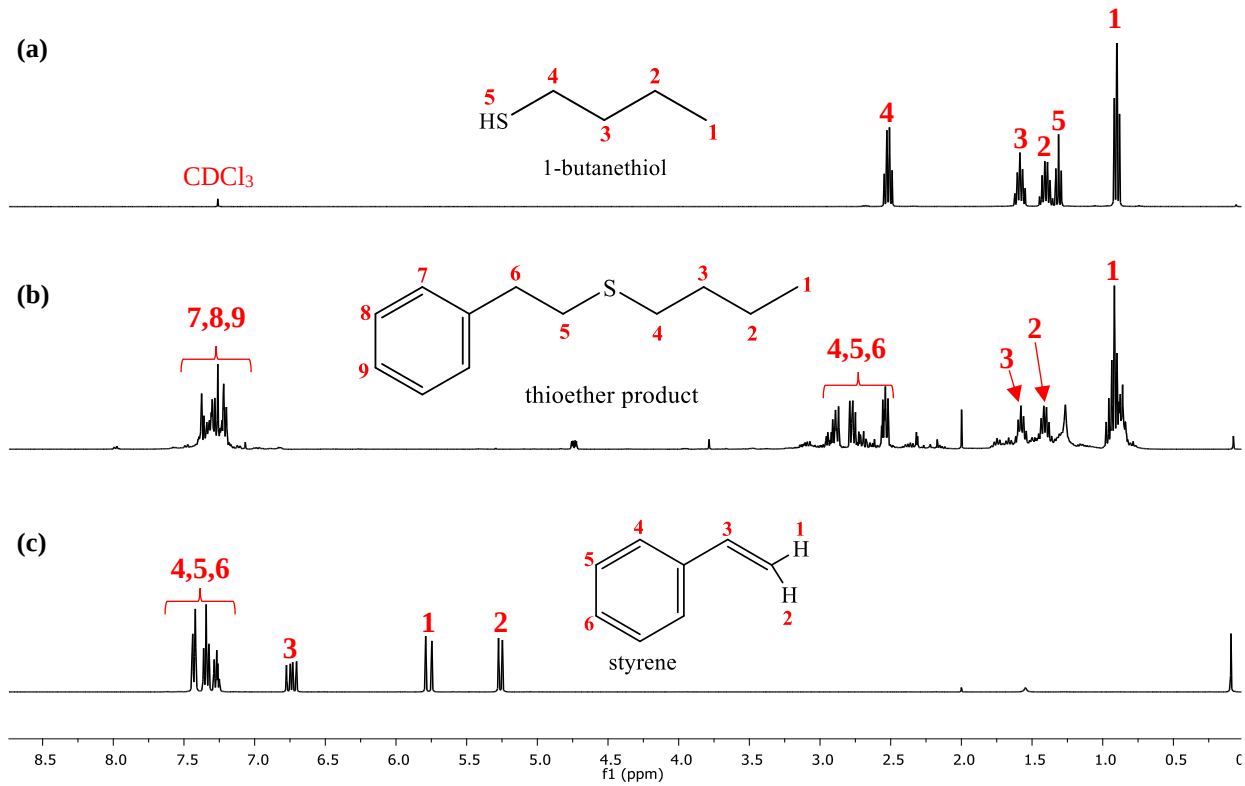

Figure 3.4 Stacked ^{1}H NMR spectra of (a) 1-butanethiol, (b) isolated product and (c) styrene in $CDCl_3$.

Table 3.2 summarises the obtained percentage yields of the isolated product ranging from moderate to good yields (37-76%). The radical thiol-ene reaction conducted with the unmodified ruthenium(II) complex **7** (Table 3.2, entry 1) resulted in lower yield (39%) in this reaction in comparison to the ligand-modified mononuclear complexes **8-10** (entries 3-5). The $[Ru(bpy)_3](PF_6)_2$ complex (**7**) exhibits the most positive excited-state reduction potential (E_{red} $_{(2+*/+)}$ = +0.350 V vs Ag/Ag^+) and was expected to undergo reductive quenching more readily than the photoexcited states of mononuclear complexes **8-10**. The possibility of a short-lived excited-state for this complex (**7**) cannot be ruled out, giving this complex less time to engage in SET with the less reactive 1-butanethiol. Therefore, the photophysical properties may be dominating in this reaction (Scheme 3.4) over electrochemical properties due to the potentially slow reductive quenching step. The lower yield for complex **7** (entry 1) can also be due to a slow addition of the generated thiyl radical to the styrene, which was faster in the case of thiophenol (Scheme 3.3) and this is common for aliphatic thiols.[25] This finding demonstrates the importance of substrate choice when designing a photocatalytic system as well as photocatalyst compatibility with substrates.

A control reaction in the absence of complex **7** (entry 2) verified that the reaction between 1-butanethiol and styrene is promoted by the photocatalyst and not by the *p*-toluidine or blue LED alone, since no background thiol-ene reaction was observed after the 2 h reaction period. The thiol-ene coupling reaction conducted with complex **9** resulted in lower yield (37%, entry 4) in comparison with that conducted with the mononuclear complex **10** (64%, entry 5). This trend is similar to that observed in the reaction with thiophenol (Table 3.1, entries 6 and 7). This suggests that complex **9** is a less reactive photoredox catalyst for the evaluated radical thiol-ene reactions than the amine-containing complex (**10**).

Comparing the reactions carried out with the mononuclear complexes **9** and **10** (entries 4 and 5) with that of the trinuclear complexes **11** and **12** (entries 6 and 7), an increase in isolated yield is observed, particularly when comparing complex **9** with **11**. This is again attributed to the presence of several photoactive centres and possibly multi-electron transfer processes in a single step resulting in enhanced reactivity of the complexes as visible-light photoredox catalysts. The obtained yields for the reactions carried out using complexes **11** (Table 3.2, entry 6) and **12** (Table 3.2, entry 7) are comparable, in stark contrast to those in the reaction carried out with thiophenol (Scheme 3.3). This supports our assertion in the previous section (Section 3.2.1), that the thiophenol creates an acidic environment resulting in the imine bond cleavage, hence the lower yield for the trinuclear complex **11** (Table 3.1, entry 8).

Table 3.2 Isolated yields from the visible-light photoredox-catalysed thiol-ene reaction of 1-butanethiol with styrene using complexes **7**-**12**.

Entry	Photoredox catalyst	% Yield[a]
1	**7**	39
2	No catalyst	–
3	**8**	63
4	**9**	37
5	**10**	64
6	**11**	68
7	**12**	76

[a]Isolated yields are the average of two reproducible experiments.

3.2.3 Visible light-mediated photoredox catalysed reaction of thiophenol with allyl alcohol

The reaction between thiophenol and allyl alcohol was carried out under blue LED irradiation in acetonitrile (Scheme 3.5). The anticipated anti-Markovnikov hydrothiolated product was not observed after the 2 h reaction period. However, it was found that disulfide formation was favoured above the anti-Markovnikov product. The disulfide product (Figure 3.5) was isolated by column chromatography, quantified and confirmed by ^{1}H NMR spectroscopy.

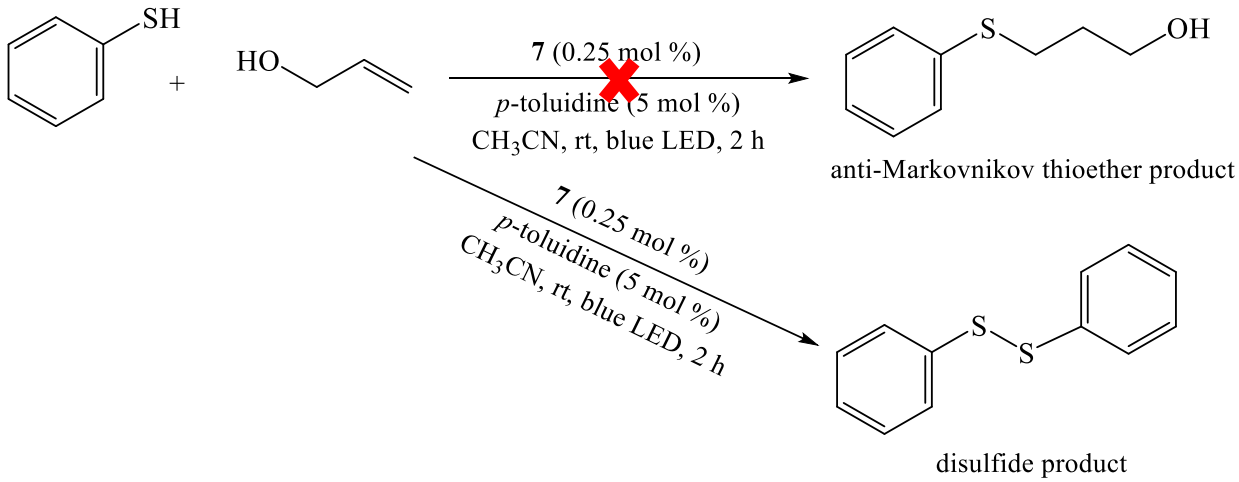

Scheme 3.5 Reaction scheme for the photoredox catalytic reaction of thiophenol with allyl alcohol under blue LED irradiation.

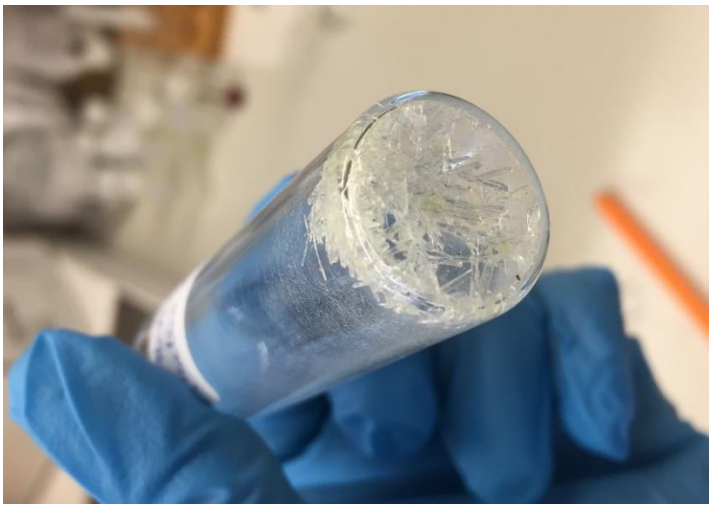

Figure 3.5 Isolated disulfide product.

The stacked ^{1}H NMR spectra (Figure 3.6) of the isolated disulfide product and the substrates show three signals in the aromatic region at 7.52 (^{3}J = 7.7 Hz), 7.32 (^{3}J = 7.4 Hz) and 7.24 ppm (^{3}J = 7.3 Hz) (H-1, H-2, H-3) but the expected aliphatic protons of the anti-Markovnikov hydrothiolated product are not observed. In comparison, the spectrum for thiophenol show a singlet at 3.45 ppm assigned to H-1 and this signal is not observed in the spectrum of the isolated product, suggesting that a reaction took place and that the thiyl radical intermediate was formed. However, the obtained spectrum for the isolated product (Figure 3.6c) suggests that the disulfide product was formed through radical-radical coupling of the generated thiyl radical. To further support this, a slight downfield shift of the aromatic protons (Figure 3.6c) is observed, which attests to the substitution of the thiophenol proton (H-1) with an aromatic sulfide.

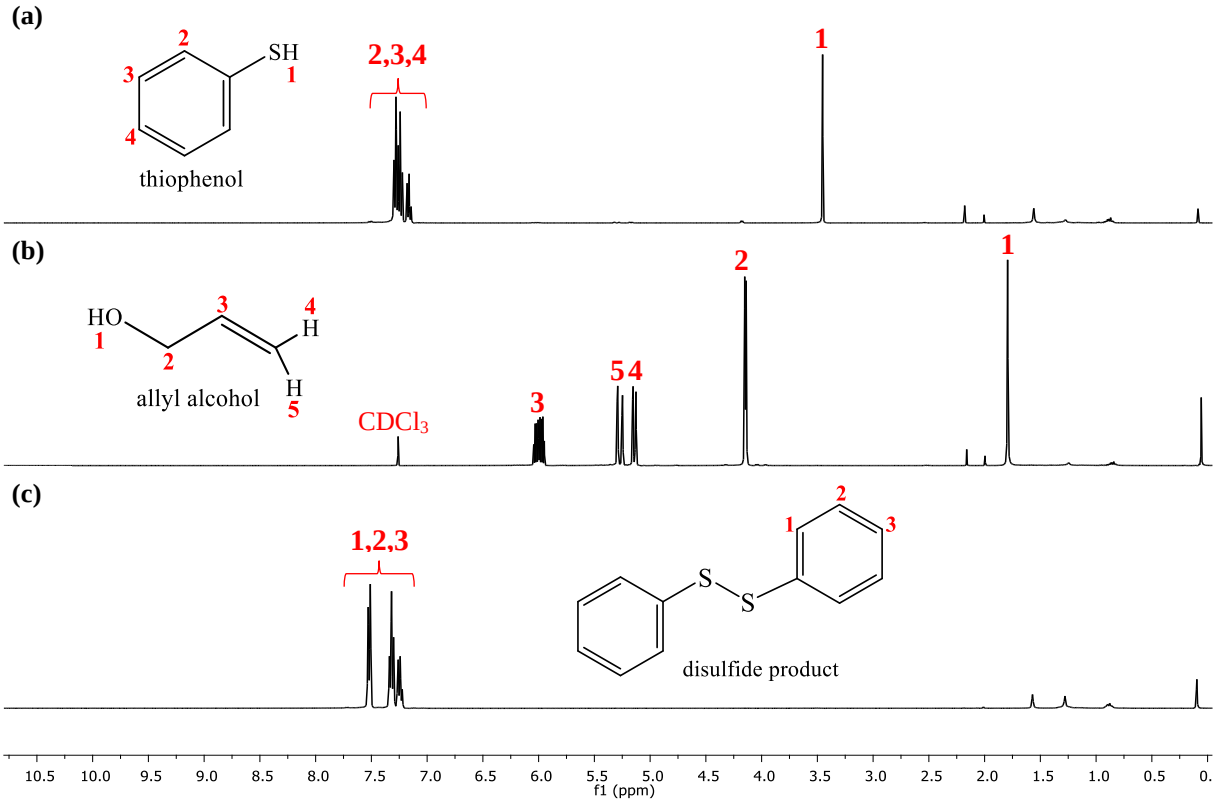

Figure 3.6 Stacked ^{1}H NMR spectra of (a) thiophenol, (b) allyl alcohol and (c) isolated product in $CDCl_3$.

Table 3.3 show the percentage yields for the isolated disulfide products, which were obtained in low yields (8-39%). The reactivity of the thiophenol is once again demonstrated in the obtained yields, where the control reaction in the absence of the photocatalyst resulted in 8% of the disulfide product (Table 3.3, entry 2). Although a reaction took place in the absence of

the photoredox catalyst, the obtained yields for the disulfide were significantly lower in comparison to those carried out in the presence of a photocatalyst (Table 3.3, entries 1 and 2-7), displaying the role of the photocatalyst in the generation of the thiyl radical. No general trend was observed in changing the substituents on the ligands of the ruthenium(II) complexes. However, it was observed that the isolated yield for the reaction conducted with complex **9** (entry 4) was comparable with that of complex **10** (entry 5). This explains the lower yield obtained for the reaction between thiophenol and styrene (Table 3.1, entry 6) and suggests that complex **9** is not an effective photocatalyst for the formation of the hydrothiolated product but favours the formation of the competing disulfide product. In a study conducted by Zhao *et al*. where the radical thiol-ene coupling reaction between allyl alcohol and thiophenol was investigated under photocatalytic conditions, the reaction required longer reaction times (6 h) with 1 mol % of an organic photoredox catalyst.[31] It is therefore, possible that the reaction in our study required longer reaction times in order for the hydrothiolated product to form. This indicates that the coupling of allyl alcohol with thiophenol is much slower than that of styrene and thiophenol.

Table 3.3 Isolated yields from the visible-light photoredox-catalysed thiol-ene reaction of thiophenol with allyl alcohol using complexes **7-12**.

Entry	Photoredox catalyst	% Yield[a,b]
1	**7**	18
2	No catalyst	8
3	**8**	26
4	**9**	28
5	**10**	27
6	**11**	29
7	**12**	39

[a]Isolated yields are the average of two reproducible experiments. [b]Isolated yields are for the disulfide product.

Comparing the reactions carried out in the presence of the mononuclear complex **9** and trinuclear complex **11**, no significant increase was observed. This further supports the observed lower yield (26%) for reaction conducted with complex **11** (entry 8) in comparison to that carried out in the presence of complex **12** (73%, entry 9) in Table 3.1. This suggests that

complex **9** decays back to the ground-state much faster or generates the thiyl radical at a much slower rate than complex **10**. This however, can only be confirmed by conducting excited-state lifetime experiments and excited-state kinetic studies.

These experimental findings indicate that poor substrate compatibility can lead to slower rate of thiol addition to the alkene, resulting in thiyl radical species build-up that promotes the radical-radical termination step, which forms the disulfide. These possible factors need to be taken into consideration when designing a photocatalyst best-suited for the visible-light radical thiol-ene reactions. To further understand the reactivity of aliphatic alkenes and substrate compatibility, photocatalytic studies using aliphatic substrates were conducted.

3.2.4 Visible light-mediated photoredox catalysed reaction of 1-butanethiol with allyl alcohol

The obtained disulfide product from the previous reaction (Scheme 3.5) indicated that the thiyl radical was successfully generated during the reaction, and the problem was not at the photoexcitation or quenching stage of the photocatalyst but by the addition of the thiyl radical to the alkene. In view of this, the thiophenol was replaced with 1-butanethiol and it was observed that the desired thioether product formed within 30 minutes of running the reaction (Scheme 3.6). The thiol-ene coupling reaction was confirmed by ^{1}H NMR spectroscopy. However, the aliphatic thioether product could not be isolated and quantified due to difficulties encountered in the purification steps of the product from the unreacted starting material.

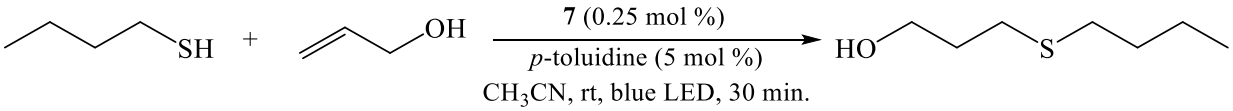

Scheme 3.6 Reaction scheme for the photoredox catalytic reaction of 1-butanethiol with allyl alcohol.

Figure 3.7 show the ^{1}H NMR of the substrates and the desired product, where the expected seven proton signals are observed. The most deshielded proton signals at 3.75, 2.62 and 2.52 ppm are assigned to H-7, H-5 and H-4 respectively. These signals are deshielded by the sulfur and oxygen atom of the –OH group. Comparing the spectrum of the product (Figure 3.7c) with that of the starting materials (Figure 3.7a and 3.7b), two new signals are observed at 2.62 and 1.84 ppm assigned to H-5 (^{3}J = 7.1 Hz) and H-4, respectively. Furthermore, an upfield shift

from 4.15 ppm (Figure 3.7b) to 3.75 ppm (Figure 3.7c) of the signal assigned to H-7 is observed upon breaking the double bond to form the thioether product, further confirmation that the reaction was successfully carried out.

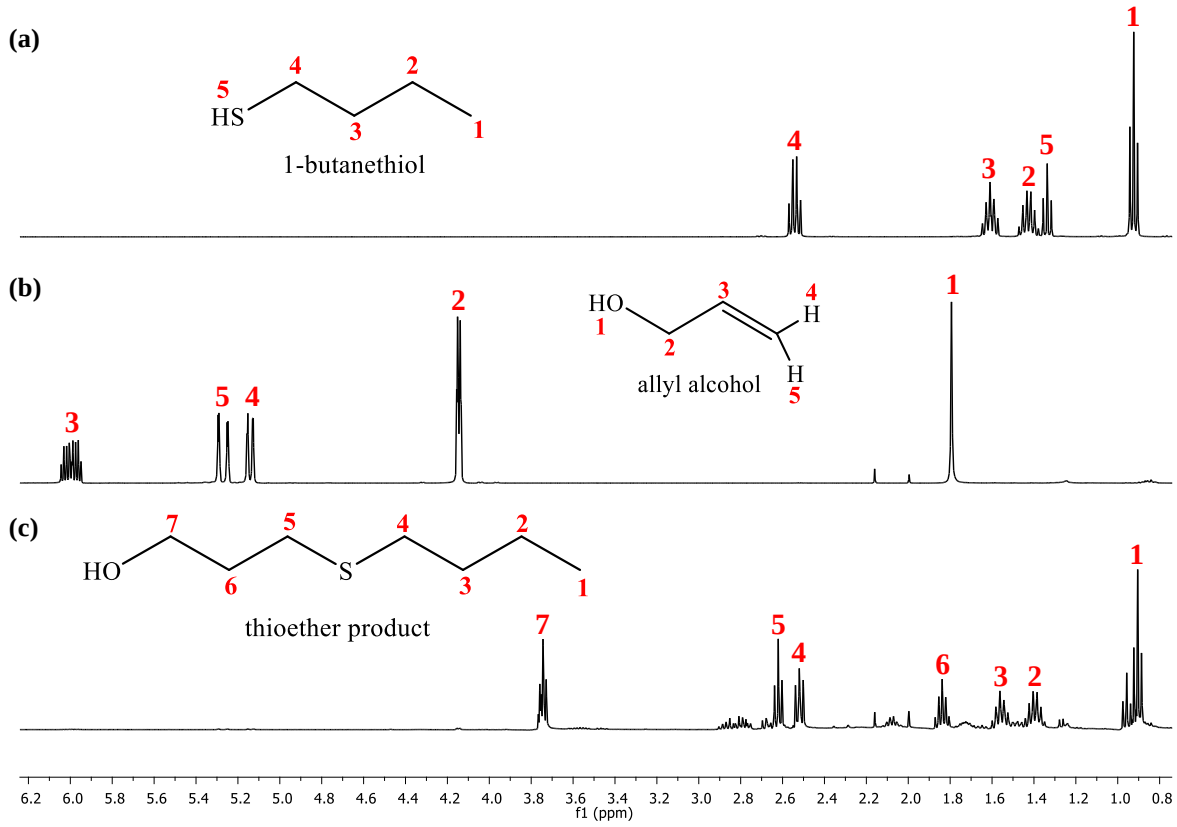

Figure 3.7 Stacked ^{1}H NMR spectra of (a) 1-butanethiol, (b) allyl alcohol and (c) isolated product in $CDCl_3$.

This confirms that allyl alcohol may not be an effective olefinic coupling partner for thiophenol hence the disulfide product was favoured over the formation of the thioether product in the previous section (Section 3.2.3). The ligand-modified complexes (**8-12**) successfully photocatalysed this coupling reaction, however, the efficiency of the catalysts relative to the unmodified catalyst (**7**) cannot be compared since the thioether product could not be isolated and quantified.

3.3 Summary

The ligand-modified complexes **8-12** were successfully evaluated as potential visible-light photoredox catalysts in the radical thiol-ene coupling reactions and the obtained results were compared to that of the prototypical $[Ru(bpy)_3](PF_6)_2$ complex (**7**). The thiol-ene coupling reaction between thiophenol and styrene resulted in the highest yield (54%) for the prototypical complex **7** in comparison to the ligand-modified mononuclear complexes (**8-10**). This was attributed to the oxidising potential of this unmodified complex (**7**), which is more positive than ligand-modified mononuclear complexes (**8-10**). However, when the aromatic thiol was replaced with an aliphatic thiol, the obtained yields for the mononuclear ligand-modified complexes improved in comparison to that of complex **7**. This demonstrated the role of substrate choice in the thiol-ene coupling reactions, where an aliphatic thiol resulted in slow addition of the generated thiyl radical to the styrene, which was faster in the case of thiophenol. Comparing the obtained yields for the complex containing an imine functional group (**9**) with that of the complex bearing an amine functionality (**10**), it was observed that the yields improved significantly upon using the amine-functionalised complex (**10**). This was attributed to the oxidising strength of the photoexcited catalyst **10** which is more positive than that of the photoexcited catalyst **9**, making the amine-functionalised complex (**10**) a better photoredox catalyst for these reactions than the imine-functionalised complex (**9**). Also, the relatively small energy gap of complex **9** (1.96 eV) possibly caused a rapid decay of the excited-state back to the ground-state (short-lived excited-state lifetime), resulting in an inefficient SET process between the photocatalyst and the thiol. The reactions carried out in the presence of the trinuclear complexes (**11** and **12**) generally resulted in a 3-fold increase in isolated yields in comparison with their respective mononuclear analogues (**9** and **10**). For example, the yield for the thiol-ene coupling reaction between thiophenol and styrene increased from 8% to 26% upon replacing the mononuclear catalyst **9** with its trinuclear analogue (**11**). A similar trend was observed between the obtained yields for the amine-containing mononuclear catalyst **10** and its trinuclear analogue (**12**), demonstrating the advantages of a multinuclear photocatalyst. This observed increase was ascribed to the presence of several photoactive centres causing a multi-electron transfer in a single step. The role of the photocatalyst was clearly demonstrated, where the control reactions carried out in the absence of the photocatalyst resulted in significantly lower yields or no product formation. Therefore, these complexes are potential visible-light photoredox catalysts for the radical thiol-ene coupling reactions and the reaction conditions can be further optimised to improve isolated yields. To better understand substrate

compatibility, the electrochemical properties of the substrates used will have to be evaluated by means of cyclic voltammetry and compared with that of the photoexcited catalyst. Moreover, the competing radical-radical homocoupling that was observed could be solved by optimising the reaction conditions such as using a higher concentration of the alkene, paving the way to future studies and optimisation of the reaction conditions for each varied substrate.

3.4 References

1. A. K. Sinha and D. Equbal, *Asian J. Org. Chem.*, 2019, **8**, 32-47.
2. D. M. Love, K. Kim, J. T. Goodrich, B. D. Fairbanks, B. T. Worrell, M. P. Stoykovich and C. N. Bowman, *J. Org. Chem.*, 2018, **83**, 2912-2919.
3. T. Tamai, K. Fujiwara, S. Higashimae, A. Nomoto and A. Ogawa, *Org. Lett.*, 2016, **18**, 2114-2117.
4. T. Tamai and A. Ogawa, *J. Org. Chem.*, 2014, **79**, 5028-5035.
5. S. P. Koo, M. M. Stamenović, R. A. Prasath, A. J. Inglis, F. E. Du Prez, C. Barner-Kowollik and T. Junkers, *J. Polym. Sci. A: Polym. Chem.*, 2010, **48**, 1699-1713.
6. K. Griesbaum, *Angew. Chem. Int. Ed.*, 1970, **9**, 273-287.
7. W. Guo, K. Tao, W. Tan, M. Zhao, L. Zheng and X. Fan, *Org. Chem. Front.*, 2019, **6**, 2048-2066.
8. I. P. Beletskaya and V. P. Ananikov, *Chem. Rev.*, 2011, **111,** 1596-1636.
9. C. E. Hoyle and C. N. Bowman, *Angew. Chem. Int. Ed.*, 2010, **49**, 1540-1573.
10. M. H. Shaw, J. Twilton and D. W. MacMillan, *J. Org. Chem.*, 2016, **81**, 6898-6926.
11. K. L. Dunbar, D. H. Scharf, A. Litomska and C. Hertweck, *Chem. Rev.*, 2017, **117**, 5521-5577.
12. K. A. Scott and J. T. Njardarson, Analysis of US FDA-approved drugs containing sulfur atoms. Sulfur Chemistry, *Springer, Cham*, 2019, 1-34.
13. A. K. Sinha and D. Equbal, *Asian J. Org. Chem.*, 2019, **8**, 32-47.
14. A. B. Lowe, *Polym. Chem.*, 2014, **5**, 4820-4870.
15. E. L. Tyson, M. S. Ament and T. P. Yoon, *J. Org. Chem.*, 2013, **78**, 2046-2050.
16. K. A. Margrey and D. A. Nicewicz, *Acc. Chem. Res.*, 2016, **49**, 1997-2006.
17. D. Mangion and D. R. Arnold, *Acc. Chem. Res.*, 2002, **35**, 297-304.
18. V. V. Levin and A. D. Dilman, *J. Org. Chem.*, 2019, **84**, 8337-8343.
19. J. K. Dunleavy, *Platin. Met. Rev.*, 2006, **50**, 110.

20. Y. Li, J. Cai, M. Hao and Z. Li, *Green Chem.*, 2019, **21**, 2345-2351.
21. N. T. Brummelhuis, C. Diehl and H. Schlaad, *Macromolecules*, 2008, **41**, 9946-9947.
22. T. Kondo and T. A. Mitsudo, *Chem. Rev.*, 2000, **100**, 3205-3220.
23. F. Denes, M. Pichowicz, G. Povie and P. Renaud, *Chem. Rev.*, 2014, **114**, 2587-2693.
24. T. Miyashita and M. Matsuda, *Bull. Chem. Soc. Jpn.*, 1985, **58**, 3031-3032.
25. E. L. Tyson, Z. L. Niemeyer and T. P. Yoon, *J. Org. Chem.*, 2014, **79**, 1427-1436.
26. J. Xu and C. Boyer, *Macromolecules*, 2015, **48**, 520-529.
27. A. B. Lowe, *Polym. Chem.*, 2010, **1**, 17-36.
28. S. Chun, J. Chung, J. E. Park and Y. K. Chung, *ChemCatChem*, 2016, **8**, 2476-2481.
29. C. He, S. Yu, S. Ma and F. Cheng, *Transit. Met. Chem.*, 2019, **44**, 515-524.
30. F. Cheng, C. He and S. Yu, *Transit. Met. Chem.*, 2017, **42**, 395-403.
31. G. Zhao, S. Kaur and T. Wang, *Org. Lett.*, 2017, **19**, 3291-3294.

Chapter 4

Overall summary and future outlook

4.1 Overall summary

Five bipyridyl ligands (**1-5**), three monomeric (**1-3**) and two new trimeric (**4** and **5**) ligands bearing aldehyde, imine and amine functionalities were prepared. The ligands were synthesised using known literature procedures that were modified accordingly for the trimeric analogues. The imine- and amine-functionalised ligands were synthesised *via* Schiff base condensation (**2** (32%) and **4** (55%)) and reductive amination reactions (**3** (36%) and **5** (74%)), respectively. The ligands were then reacted with the *cis*-dichlorobis(2,2'-bipyridine)ruthenium(II) complex (**6**) to afford their corresponding heteroleptic ruthenium(II) hexafluorophosphate complexes (**8-12**) in moderate to good yields (27–86%). The known $[Ru(bpy)_3](PF_6)_2$ complex (**7**) was also synthesised (94%) and used as a reference for this study. The resulting complexes were fully characterised by various spectroscopic and analytical techniques such as ^{1}H NMR, $^{13}C\{^1H\}$ NMR, FT-IR spectroscopy and mass spectrometry.

Furthermore, electrochemical, electronic absorption and emission studies for the complexes (**8-12** and the prototypical complex **7**) were carried out. The concentrations for the trinuclear complexes were adjusted accordingly to allow direct comparison with their mononuclear analogues. The obtained data was comparable to that of the known complex (**7**) and all complexes displayed a broad emission band in the 609–633 nm range. This emission band was assigned to the transition from the triplet MLCT excited-state (^{3}MLCT) to the ground-state. The ligand-modified complexes (**8-12**) exhibited red shifted emission spectra relative to complex **7**, with complex **9** being the most red shifted. This observed red shift was attributed to a lowered LUMO energy of the excited-state for this complex (**9**), demonstrating the effects of ligand modifications on the excited-state photophysical properties of such complexes.

The excited-state redox potentials for complexes **8-12** were comparable to that of the known complex (**7**) with reversible redox couples, displaying promising photocatalytic activity. The photoexcited complex **7** displayed the most positive excited-state reduction potential ($E_{red\ (2+*/+)}$ = +0.350 V), making it a more potent oxidant compared with the photoexcited states of complexes **8-12**. These complexes (**7-12**) were then evaluated as visible-light photoredox

catalysts in the radical hydrothiolation reaction of olefins (thiol-ene reactions) to produce thioethers.

The thiol-ene experiments were carried out in duplicate and the product was purified by column chromatography. The isolated yield from the reaction between thiophenol and styrene, was higher for complex **7** (54%) in comparison to the mononuclear complexes **8-10** (8–24%). This result was expected, based on electrochemical data, since **7** exhibited the most positive excited-state reduction potential, making the photoexcited state of this complex more readily quenched by the thiophenol. However, upon replacing the thiophenol with 1-butanethiol, an aliphatic thiol, the yield for complex **7** (39%) decreased. The lower yield was possibly due to a shorter excited-state lifetime for this complex (**7**) relative to mononuclear complexes **8** and **10**, resulting in an inefficient single-electron (SET) process with the relatively less reactive 1-butanethiol. Comparing the obtained yield for complex **9** with that of complex **10**, it was observed that the yields improved significantly on changing the imine substituent (**9**) to an amine substituent (**10**). This was attributed to the oxidising strength of the photoexcited catalyst **10** which is more positive than that of complex **9**, making the amine-functionalised complex (**10**) a better photoredox catalyst for these reactions than the imine-functionalised complex (**9**). Also, the relatively small energy gap of complex **9** (1.96 eV) possibly caused a rapid decay of the excited-state back to the ground-state (short-lived excited-state lifetime), resulting in an inefficient SET process between the photocatalyst and the thiol.

The reactions carried out in the presence of the trinuclear complexes (**11** and **12**) generally resulted in a 3-fold increase in isolated yields in comparison with their respective mononuclear analogues (**9** and **10** respectively). For example, the obtained yields for the thiol-ene coupling reaction between thiophenol and styrene increased from 8% to 26% upon replacing the mononuclear catalyst **9** with its trinuclear analogue (**11**). A similar trend was observed between the obtained yields for the amine-containing mononuclear catalyst **10** (26%) and its trinuclear analogue (**12**, 73%), demonstrating the advantages of a multinuclear photocatalyst. This observed increase was ascribed to the presence of several photoactive centres causing a multi-electron transfer in a single step. Lastly, the role of the photocatalyst was clearly shown by the control reactions carried out in the absence of the photocatalyst, which resulted in significantly lower yields or no product formation. Therefore, these complexes are potential visible-light

photoredox catalysts for the radical thiol-ene coupling reactions and the reaction conditions can be further optimised to improve isolated yields.

4.2 Future outlook

The effects of ligand-modifications and the multinuclearity of the ruthenium(II) complexes in the photoredox catalysis of radical thiol-ene coupling reactions was investigated in this study. The obtained yields from the photocatalytic experiments demonstrated the advantages of multinuclear photocatalysts in enhancing the photo-activity of the catalyst in these types of reactions. These complexes display great potential in the field of photoredox catalysis, particularly in the synthesis of small organic molecules. Analogous complexes may be designed with modifications on the ligands that will increase the HOMO-LUMO energy gap of the triplet MLCT excited-state such that the resulting photocatalysts have long-lived excited-states, that is, slow decay of the excited-state to the ground-state. The obtained data from the thiol-ene experiments also revealed the importance of substrate compatibility when designing such photocatalytic systems. Therefore, future studies on a broader scope of substrates may be carried out to determine the trends in photocatalyst-substrate interaction. Additionally, studies on the excited-state kinetics, quantum yields and DFT calculations for these complexes may be performed to determine the excited-state lifetimes and the relative HOMO-LUMO gap energies. This will allow for a better understanding on the types of ligands and substituents (electron-withdrawing or electron-donating) best suited for certain types of applications and organic transformations for these Ru^{II}-type complexes.

Chapter 5

Experimental

5.1 General methods

All reactions were carried out under N_2 atmosphere using standard Schlenk line techniques unless stated otherwise. Solvents used were reagent grade and were used as received with the exception of 1,4-dioxane, *N*,*N*-dimethylformamide and methanol which were degassed with nitrogen prior to use. All other chemicals were purchased from Merck and used without further purification. Nuclear Magnetic Resonance (NMR) spectra were recorded using either a Bruker X400 (^{1}H: 400.22 MHz, ^{13}C{^{1}H}: 100.65 MHz) or a Varian Mercury 300 (^{1}H: 300.08 MHz, ^{13}C{^{1}H}: 75.46 MHz) spectrometer. Chemical shift values (δ) and *J*-coupling constants are reported in ppm and Hz respectively, relative to tetramethylsilane (TMS) as an internal standard (δ 0.00). Infrared spectra were recorded using a Perkin-Elmer Spectrum 100 FT-IR spectrometer equipped with an Attenuated Total Reflectance Infrared unit (ATR-IR).

Purity was determined using an analytical Agilant HPLC 1260 equipped with an Agilent infinity diode array detector (DAD) 1260 UV-Vis detector, with an absorption wavelength range of 210 – 640 nm. The ligands were eluted with a mixture of solvent A (10 mM NH_4OAc/H_2O) and solvent B (10 mM NH_4OAc/CH_3OH) at a flow rate of 0.9 mL min^{-1}. The gradient elution conditions were as follows: 10% solvent B from 0 - 1 min, 10 – 95% solvent B from 1 - 3 min, 95% solvent B from 3 - 5 min. High resolution mass spectrometry was performed using a Waters Synapt G2 electron spray ionisation mass spectrometer (ESI-MS) with data recorded in positive-ion mode. Melting points were determined using a Büchi B-540 melting point apparatus.

Emission spectroscopy data was collected using a Varian Cary Eclipse fluorescence spectrophotometer at room temperature with an excitation wavelength of 450 nm. Electrochemical measurements were performed on a BASi EC Epsilon potentiostat connected to a BASi C3 cell stand and analysed using Epsilon software. A standard three-electrode setup was used, consisting of a glassy carbon working electrode, platinum-wire counter electrode and $Ag/AgNO_3$ reference electrode. All samples were degassed with argon prior to measurements.

5.2 Synthesis of aldehyde-functionalised bipyridyl ligand (1)[1]

Ligand (**1**) was synthesised following a procedure that has been previously reported in the literature.[1]

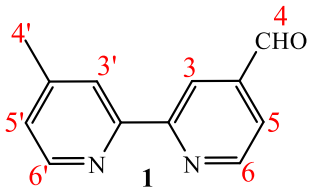

1

A suspension of 4,4'-dimethyl-2,2'-bipyridine (1.46 g, 7.93 mmol) and selenium dioxide (1.06 g, 9.52 mmol) in 1,4-dioxane (70 mL) was heated under reflux for 24 h. The hot reaction mixture was filtered by gravity to remove metallic selenium as a by-product. The filtrate was cooled to room temperature and further filtered by gravity to remove a brown solid. The solvent of the filtrate was then removed under reduced pressure and the orange residue was partially dissolved in ethyl acetate (140 mL) followed by gravity filtration to remove excess selenium dioxide. The filtrate was washed with 1.0 *M* Na_2CO_3 solution (2 × 35 mL) to remove acids and with 0.3 *M* $Na_2S_2O_5$ solution (3 × 35 mL) to form an aldehyde bisulfite intermediate. The combined aqueous extracts were adjusted to pH 10 using Na_2CO_3 and extracted with dichloromethane (4 × 35 mL). The combined organic extracts were dried over anhydrous magnesium sulfate and filtered by gravity. The solvent of the filtrate was removed under reduced pressure to afford ligand **1** as a white solid.

Yield: (1.57 g, 28%). **Melting point**: 132–139 °C (literature value: 131–132 °C). **^{1}H NMR** (300 MHz, $CDCl_3$) δ_{ppm} 10.18 (s, 1H, 4-C**H**O), 8.89 (d, ^3J = 4.9 Hz, 1H, H-6), 8.84 (s, 1H, H-3), 8.58 (d, ^3J = 4.9 Hz, 1H, H-6'), 8.29 (s, 1H, H-3'), 7.72 (dd, ^3J = 4.9 Hz, ^4J = 1.5 Hz, 1H, H-5), 7.20 (dd, ^3J = 4.9 Hz, ^4J = 0.9 Hz, 1H, H-5'), 2.47 (s, 3H, 4'-C**H$_3$**). **IR/ATR ($\boldsymbol{v/cm^{-1}}$):** sharp, strong (C=O) 1702, sharp, strong $(C=N)_{bpy}$ 1595. **LC-MS**: *m/z* = 199.1 (100%, $[M+H]^+$) (calcd. 198.1).

5.3 Syntheses of bipyridyl ligands containing an imine functionality

The imine bipyridyl ligands **2** and **4** were synthesised following a method reported in the literature for the Schiff base condensation reaction of bipyridyl, which was modified accordingly for the trimeric ligand (**4**).[2]

*5.3.1 Synthesis of monomeric ligand (**2**)*[2]

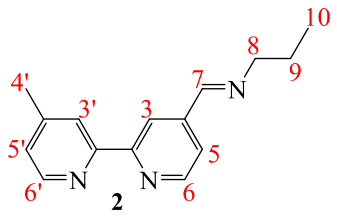

2

A solution of *n*-propylamine (94.8 mg, 1.60 mmol) in dry dichloromethane (5 mL) was added dropwise to a stirred solution of 4'-methyl-2,2'-bipyridine-4-carboxaldehyde (0.212 g, 1.07 mmol) in dry dichloromethane (15 mL) and stirred for 24 h at room temperature over anhydrous magnesium sulfate. The reaction mixture was filtered by gravity and the solvent removed by rotary evaporation to afford a yellow oil. The resulting oil was dissolved in dichloromethane (20 mL) and washed with water (10 × 10 mL). The organic fractions were combined, dried over anhydrous magnesium sulfate and filtered by gravity. The solvent of the filtrate was removed under reduced pressure and the resulting oil (**2**) was then dried *in vacuo*.

Yield: (82.3 mg, 32%). **^{1}H NMR** (300 MHz, $CDCl_3$) δ_{ppm} 8.70 (d, ^3J = 5.0 Hz, 1H, H-6), 8.62 – 8.49 (m, 2H, H-7, H-6'), 8.34 (s, 1H, H-3), 8.23 (s, 1H, H-3'), 7.69 (dd, ^3J = 5.0 Hz, ^4J = 1.5 Hz, 1H, H-5), 7.13 (d, ^3J = 5.7 Hz, 1H, H-5'), 3.63 (td, ^3J = 6.9 Hz, ^4J = 1.2 Hz, 2H, H-8), 2.43 (s, 3H, 4'-C**H**$_3$), 1.84 – 1.64 (m, 2H, H-9), 0.95 (t, ^3J = 7.4 Hz, 3H, H-10). **IR/ATR (ν/cm^{-1}):** sharp, strong $(C{=}N)_{imine}$ 1650, sharp, strong $(C{=}N)_{bpy}$ 1594.

*5.3.2 Synthesis of trimeric ligand (**4**)*

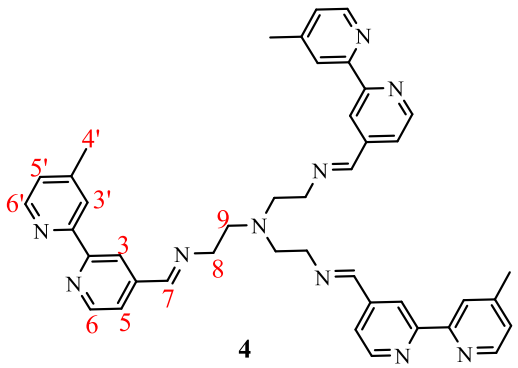

4

A solution of tris(2-aminoethyl)amine (41.8 mg, 0.286 mmol) in dry dichloromethane (5 mL) was added dropwise to a stirring solution of 4'-methyl-2,2'-bipyridine-4-carboxaldehyde (0.170 g, 0.858 mmol) in dry dichloromethane (10 mL) and stirred for 48 h at room temperature over anhydrous magnesium sulfate. The reaction mixture was filtered by gravity and the solvent removed under reduced pressure to afford a yellow oil. The resulting oil was dissolved in dichloromethane (15 mL) and washed with water (10 × 5 mL). The organic layer was separated, dried over anhydrous magnesium sulfate and filtered by gravity. The solvent was then removed under reduced pressure and the resulting yellow oil (**4**) was dried *in vacuo*.

Yield: (0.108 g, 55%). **^{1}H NMR** (300 MHz, $CDCl_3$) δ_{ppm} 8.63 (d, ^{3}J = 5.0 Hz, 3H, H-6), 8.57 – 8.47 (m, 6H, H-7, H-6'), 8.28 (s, 3H, H-3), 8.18 (s, 3H, H-3'), 7.54 (dd, ^{3}J = 5.0 Hz, ^{4}J = 1.5 Hz, 3H, H-5), 7.12 (dd, ^{3}J = 4.9 Hz, ^{4}J = 0.9 Hz, 3H, H-5'), 3.77 (t, ^{3}J = 6.1 Hz, 6H, H-8), 3.00 (t, ^{3}J = 6.4 Hz, 6H, H-9), 2.42 (s, 9H, 4'-C**H**$_3$). **^{13}C{^{1}H} NMR** (101 MHz, $CDCl_3$) δ_{ppm} 160.3 (**C**H_{imine}), 149.7 (**C**H_{Ar}), 149.2 (**C**H_{Ar}), 125.5 (**C**H_{Ar}), 125.0 (**C**H_{Ar}), 122.1 (**C**H_{Ar}), 121.1 (**C**H_{Ar}), 60.4 (**C**H_2), 55.4 (**C**H_2), 21.3 (4'-**C**H_3). **IR/ATR (ν/cm^{-1}):** sharp, medium $(C{=}N)_{imine}$ 1647, sharp, strong $(C{=}N)_{bpy}$ 1594.

5.4 Syntheses of bipyridyl ligands containing an amine functionality

The amine-functionalised bipyridyl ligands **3** and **5** were synthesised using a procedure previously reported in the literature, which was modified accordingly.[3]

*5.4.1 Synthesis of monomeric ligand (**3**)*[3]

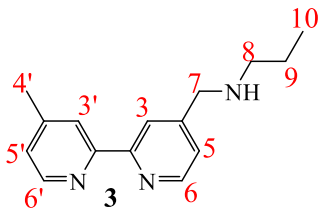

3

Sodium borohydride (0.0716 mg, 1.89 mmol) was added to a stirred solution of compound **2** (0.174 g, 0.727 mmol) in 15 mL of anhydrous methanol. The reaction mixture was stirred for 24 h at room temperature and the excess hydride was quenched with ice-cold water (15 mL) and filtered by gravity. The azeotropic mixture was reduced by rotary evaporation to afford an aqueous mixture of the product. The aqueous layer was extracted with dichloromethane (5 × 10 mL). The combined organic extracts were washed with water (4 × 20 mL), dried over anhydrous magnesium sulfate and filtered by gravity. The solvent was removed under reduced pressure to afford compound **3** as a yellow oil.

Yield: (63.8 mg, 36%). **^{1}H NMR** (300 MHz, $CDCl_3$) δ_{ppm} 8.64 (d, ^3J = 5.0 Hz, 1H, H-6), 8.52 (d, ^3J = 4.9 Hz, 1H, H-6'), 8.35 (s, 1H, H-3), 8.21 (s, 1H, H-3'), 7.49 (dd, ^3J = 5.0 Hz, ^4J = 1.4 Hz, 1H, H-5), 7.12 (d, ^3J = 4.9 Hz, 1H, H-5'), 3.98 (s, 2H, H-7), 2.78 – 2.59 (m, 2H, H-8), 2.42 (s, 3H, 4'-C**H$_3$**), 1.79 – 1.54 (m, 2H, H-9), 0.93 (t, ^3J = 7.4 Hz, 3H, H-10). **IR/ATR ($\boldsymbol{\nu/cm^{-1}}$):** broad, weak (N−H) 3367, sharp, strong $(C{=}N)_{bpy}$ 1596. **LC-MS**: *m/z* = 242.1 (100%, $[M+H]^+$) (calcd. 242.2).

*5.4.2 Synthesis of trimeric ligand (**5**)*

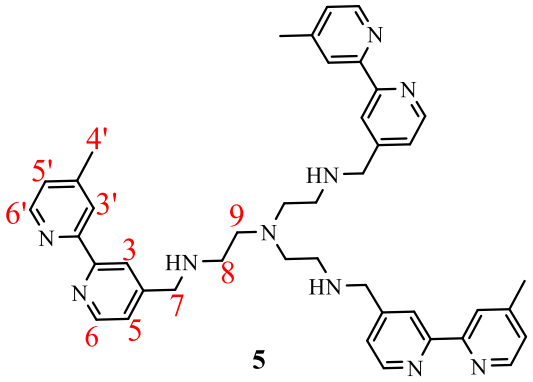

5

To a stirring solution of 4'-methyl-2,2'-bipyridine-4-carboxaldehyde (30.8 mg, 0.155 mmol) in dry dichloromethane (10 mL), was added tris(2-aminoethyl)amine (7.60 mg, 0.0518 mmol) in dry dichloromethane (5 mL) and stirred for 24 h at room temperature over anhydrous magnesium sulfate. The reaction mixture was filtered by gravity and the solvent of the filtrate was removed under reduced pressure to afford a yellow oil. The crude oil was dissolved in dry methanol (15 mL) and stirred for 30 min. Thereafter, sodium borohydride (8.82 mg, 0.233 mmol) was added slowly to the stirring solution and the reaction proceeded overnight at room temperature. The reaction mixture was cooled in an ice bath and excess hydride was quenched with ice-cold water (15 mL) and filtered by gravity. The azeotropic mixture was reduced under reduced pressure to afford an aqueous mixture. The product was extracted with dichloromethane (4 × 10 mL). The combined organic extracts were washed with water (5 × 10 mL), followed by washing with brine (3 × 10 mL), dried over anhydrous magnesium sulfate and filtered by gravity. The solvent of the filtrate was removed under reduced pressure to afford the new compound **5** as a yellow oil.

Yield: (26.6 mg, 74%). **^{1}H NMR** (400 MHz, CD_3OD) δ_{ppm} 8.42 – 8.39 (m, 6H, H-6, H-6'), 8.17 (s, 3H, H-3), 8.01 (s, 3H, H-3'), 7.27 – 7.24 (m, 3H, H-5), 7.19 (d, ^{3}J = 4.3 Hz, 3H, H-5'), 3.83 (s, 6H, H-7), 2.73 (d, ^{3}J = 4.9 Hz, 6H, H-8), 2.68 (d, ^{3}J = 5.0 Hz, 6H, H-9), 2.39 (s, 9H, 4'-C**H**$_3$). **^{13}C{^{1}H} NMR** (101 MHz, CD_3OD) δ_{ppm} 151.8 (**C**$_{Ar}$), 150.5 (**C**$_{Ar}$), 150.2 – 149.6 (**C**$_{Ar}$), 126.1 (**C**H$_{Ar}$), 124.5 (**C**H$_{Ar}$), 123.6 (**C**H$_{Ar}$), 122.6 (**C**H$_{Ar}$), 122.1 (**C**H$_{Ar}$), 120.2 (**C**H$_{Ar}$), 63.6 (**C**H$_2$), 55.1 (**C**H$_2$), 53.3 (**C**H$_2$), 21.2 (4'-**C**H$_3$). **IR/ATR (ν/cm^{-1}):** broad, weak (N−H) 3294, sharp, strong (C=N)$_{bpy}$ 1594.

5.5 Synthesis of *cis*-dichlorobis(2,2'-bipyridine)ruthenium(II) complex (6)[4]

The *cis*-dichlorobis(2,2'-bipyridine)ruthenium(II) complex precursor (**6**) was synthesised following a procedure that has been previously reported in literature.[4]

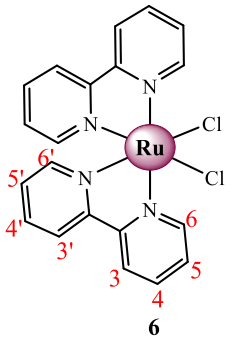

6

A mixture of $RuCl_3 \bullet 3H_2O$ (0.193 g, 0.930 mmol), 2,2'-bipyridine (0.292 g, 1.87 mmol) and LiCl (0.167 g, 3.95 mmol) were refluxed in anhydrous *N,N'*-dimethylformamide (10 mL) for 24 h. After cooling to room temperature, the reaction mixture was concentrated to *ca*. 3 mL under vacuum, followed by the addition of reagent grade acetone (95 mL). The resulting solution was cooled at *ca.* −5 ℃ overnight. A black precipitate was collected by vacuum filtration to afford compound **6** as a black solid. The solid (**6**) was washed with water (10 mL) followed by diethyl ether (20 mL) and then dried *in vacuo*.

Yield: (0.368 g, 82%). **^{1}H NMR** (300 MHz, $(CD_3)_2SO$) δ_{ppm} 10.12 – 9.84 (m, 2H, H-6), 8.72 – 8.56 (m, 2H, H-3), 8.54 – 8.37 (m, 2H, H-3'), 8.06 (ddd, ^3J = 9.1 Hz, ^3J = 6.5 Hz, ^4J = 1.5 Hz, 2H, H-4), 7.77 (ddd, ^3J = 7.2 Hz, ^3J = 3.5 Hz, ^4J = 0.7 Hz, 2H, H-5), 7.67 (qd, ^3J = 7.8 Hz, ^4J = 1.4 Hz, 2H, H-4'), 7.51 (dd, ^3J = 5.7 Hz, ^4J = 0.7 Hz, 2H, H-6'), 7.10 (ddd, ^3J = 7.2 Hz, ^3J = 5.8 Hz, ^4J = 1.3 Hz, 2H, H-5'). **IR/ATR ($\boldsymbol{\nu/cm^{-1}}$):** sharp, weak $(C{=}N)_{bpy}$ 1601.

5.6 Synthesis of tris(2,2'-bipyridine)ruthenium(II) complex (7)[5]

The tris(2,2'-bipyridine)ruthenium(II) hexafluorophosphate complex (**7**) was synthesised following a procedure previously reported in literature, which was modified accordingly.[5]

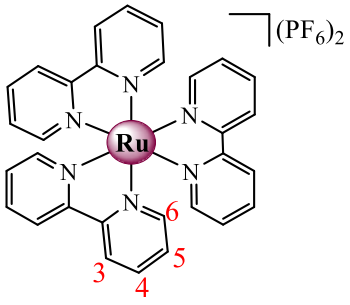

7

A mixture of $RuCl_3 \bullet 3H_2O$ (1.03 g, 4.95 mmol) and 2,2'-bipyridine (2.40 g, 15.4 mmol) were refluxed in anhydrous *N,N'*-dimethylformamide (15 mL) for 24 h. After cooling to room temperature, the solvent was removed under reduced pressure followed by the addition of water (10 mL) and a saturated aqueous solution of ammonium hexafluorophosphate (*ca.* 10 mL). The resulting orange-brown precipitate was collected by vacuum filtration and washed with water (15 mL) and diethyl ether (20 mL). The solid was dissolved in acetone and precipitated with diethyl ether to afford compound **7** as an orange powder which was collected by vacuum filtration and dried *in vacuo*.

Yield: (3.98 g, 94%). **Melting point**: onset occurs at 308 °C (decomposes without melting). **^{1}H NMR** (300 MHz, $(CD_3)_2SO$) δ_{ppm} 8.83 (d, ^3J = 8.1 Hz, 6H, H-3), 8.17 (td, ^3J = 8.0 Hz, ^4J = 1.3 Hz, 6H, H-4), 7.74 (d, ^3J = 4.9 Hz, 6H, H-6), 7.63 – 7.43 (m, 6H, H-5). **IR/ATR (ν/cm^{-1}):** sharp, medium $(C{=}N)_{bpy}$ 1605. **Emission:** λ_{em} = 609 nm. **HR-ESI-MS**: *m/z* = 285.0564 (100%, $[M-2PF_6]^{2+}$) (calcd. 285.0550).

5.7 Synthesis of ruthenium(II) bipyridyl complex functionalised with an aldehyde (8)[6,7]

Complex **8** was synthesised by reacting ligand **1** with complex precursor **6**, following a method previously reported in the literature.[6,7]

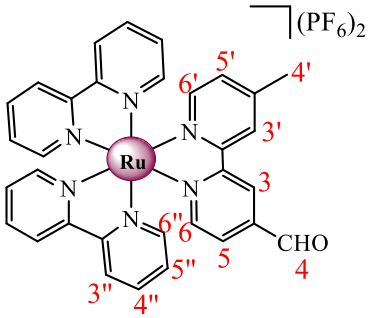

8

To a stirred solution of *cis*-dichlorobis(2,2'-bipyridine)ruthenium(II) (0.107 g, 0.221 mmol) in ethanol (20 mL) was added 4'-methyl-2,2'-bipyridine-4-carboxaldehyde slowly (65.8 mg, 0.332 mmol), and the mixture was refluxed for 24 h. Thereafter, the solvent of the reaction mixture was removed under reduced pressure. The remaining residue was re-dissolved in water (30 mL) and washed with dichloromethane (4 × 15 mL) and diethyl ether (2 × 15 mL). The aqueous fraction was then concentrated to *ca.* 3 mL under reduced pressure. A saturated aqueous solution of ammonium hexafluorophosphate was added (*ca.* 10 mL) and stirred for 30 min. at room temperature. A red precipitate (**8**) was collected *via* filtration by vacuum, washed with cold water (10 mL) and diethyl ether (15 mL), and dried *in vacuo*.

Yield: (0.168 g, 85%). **Melting point**: onset occurs at 217 °C (decomposes without melting). **^{1}H NMR** (300 MHz, $(CD_3)_2CO$) δ_{ppm} 10.23 (s, 1H, 4-C**H**O), 9.12 (d, ^4J = 1.0 Hz, 1H, H-3), 8.90 (s, 1H, H-3'), 8.81 (d, ^3J = 8.1 Hz, 4H, H-3''), 8.37 (d, ^3J = 5.8 Hz, 1H, H-5), 8.26 – 8.17 (m, 4H, H-4''), 8.11 – 8.01 (m, 4H, H-6''), 7.89 (dd, ^3J = 5.5 Hz, ^4J = 2.2 Hz, 2H, H-6, H-6'), 7.62 – 7.53 (m, 4H, H-5''), 7.47 (dd, ^3J = 5.7 Hz, ^4J = 0.9 Hz, 1H, H-5'), 2.62 (s, 3H, 4'-C**H**$_3$). **IR/ATR (ν/cm^{-1}):** sharp, medium (C=O) 1707, weak $(C{=}N)_{bpy}$ 1605. **Emission:** λ_{em} = 616 nm. **HR-ESI-MS**: *m/z* = 306.0609 (100%, $[M-2PF_6]^{2+}$) (calcd. 306.0600), *m/z* = 757.0843 (10%, $[M-PF_6]^+$) (calcd. 757.0800).

5.8 Syntheses of mononuclear and trinuclear ruthenium(II) complexes containing imine functionalities

Complexes **9** and **11** were synthesised following a literature reported procedure, which was modified accordingly for both complexes.[8]

*5.8.1 Synthesis of mononuclear ruthenium(II) complex (**9**)*[8]

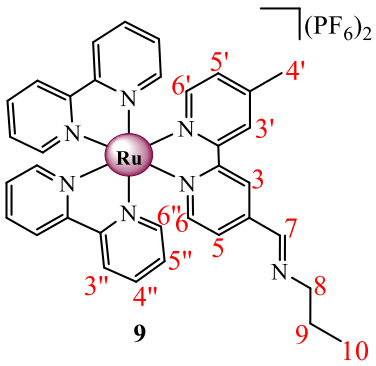

9

Compound **8** (67.9 mg, 0.0753 mmol) was suspended in ethanol (10 mL) and *n*-propylamine (44.5 mg, 0.753 mmol) was added dropwise to this solution. The reaction mixture was heated at 50 ℃ over anhydrous magnesium sulfate. After 3 h, the reaction mixture was cooled to room temperature and filtered by gravity. The solvent of the filtrate was concentrated to *ca.* 2 mL under reduced pressure and the product was precipitated upon addition of diethyl ether. The resulting red solid (**9**) was collected *via* filtration by vacuum and washed with diethyl ether and pentane, and dried *in vacuo*.

Yield: (19.1 mg, 27%). **Melting point**: onset occurs at 178 ℃ (decomposes without melting). **^{1}H NMR** (300 MHz, $(CD_3)_2CO$) δ_{ppm} 9.01 (s, 1H, H-3), 8.80 (m, 5H, H-3'', H-7), 8.53 (s, 1H, H-3'), 8.21 (t, ^{3}J = 7.7 Hz, 4H, H-4''), 8.12 (t, ^{3}J = 6.1 Hz, 2H, H-5), 8.05 (d, ^{3}J = 5.0 Hz, 3H, H-6''), 7.87 (d, ^{3}J = 5.7 Hz, 1H, H-6'), 7.81 (d, ^{3}J = 5.0 Hz, 1H, H-6), 7.58 (t, ^{3}J = 6.5 Hz, 4H, H-5''), 7.44 (d, ^{3}J = 5.5 Hz, 1H, H-5'), 3.68 (t, ^{3}J = 6.6 Hz, 2H, H-8), 2.60 (s, 3H, 4'-C**H**$_3$), 1.80 – 1.63 (m, 2H, H-9), 0.94 (t, ^{3}J = 7.4 Hz, 3H, H-10). **^{13}C{^{1}H} NMR** (101 MHz, $(CD_3)_2CO$) δ_{ppm} 157.6 – 156.2 (**C**$_{Ar}$), 152.2 – 150.6 (**C**H$_{Ar,}$ **C**H$_{imine}$), 137.9 (**C**H$_{Ar}$), 127.8 (**C**H$_{Ar}$), 124.4 (**C**H$_{Ar}$), 63.0 (C-8), 23.6 (4'-**C**H$_3$), 20.2 (C-9), 11.1 (C-10). **IR/ATR (ν/cm^{-1}):** weak (C=N)$_{imine}$ 1623, weak (C=N)$_{bpy}$ 1605. **Emission:** λ_{em} = 633 nm. **HR-ESI-MS**: *m/z* = 315.0670 (88%, $[M+3H]^{3+}$) (calcd. 315.2373).

*5.8.2 Synthesis of trinuclear ruthenium(II) complex (**11**)*

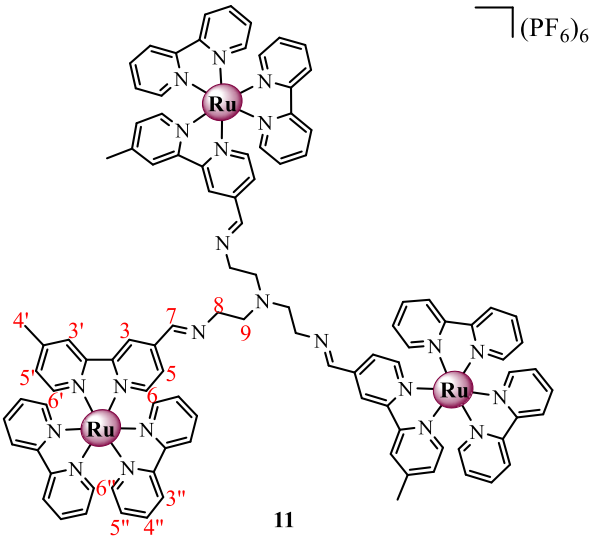

Compound **8** (0.152 g, 0.169 mmol) was suspended in ethanol (25 mL) and tris(2-aminoethyl)amine (8.23 mg, 0.0563 mmol) in ethanol (5 mL) was added dropwise to this solution. The reaction mixture was heated for 3 h at 50 ℃ over anhydrous magnesium sulfate. The reaction mixture was then cooled to room temperature and filtered by gravity. The solvent was then reduced to a minimum (*ca.* 3 mL) and the product was precipitated upon addition of diethyl ether and the mixture was cooled overnight at *ca.* −5 ℃. The resulting fine orange precipitate was collected *via* vacuum filtration and washed with diethyl ether. The collected orange solid was re-dissolved in minimum acetonitrile and the resulting solution was added dropwise to diethyl ether with vigorous stirring. The resulting orange precipitate (**11**) was collected by vacuum filtration and dried *in vacuo*.

Yield: (0.103 g, 59%). **Melting point**: onset occurs at 189 ℃ (decomposes without melting). **^{1}H NMR** (300 MHz, $(CD_3)_2CO$) δ_{ppm} 8.80 (m, 18H, H-3, H-3'', H-7), 8.68 (s, 3H, H-3'), 8.18 (dd, ^3J = 9.6 Hz, ^3J = 3.4 Hz, 12H, H-4''), 8.12 – 7.97 (m, 15H, H-5, H-6''), 7.95 – 7.78 (m, 6H, H-6', H-6), 7.56 (dd, ^3J = 11.9 Hz, ^3J = 6.1 Hz, 12H, H-5''), 7.40 (d, ^3J = 5.5 Hz, 3H, H-5'), 2.57 (s, 9H, 4'-C**H$_3$**), 2.26 (td, ^3J = 4.8 Hz, ^3J = 2.6 Hz, 6H, H-9), 1.84 (td, ^3J = 4.6 Hz, ^3J = 2.3 Hz, 6H, H-8). **IR/ATR (ν/cm^{-1}):** weak $(C{=}N)_{imine}$ 1623, weak $(C{=}N)_{bpy}$ 1605. **Emission:** λ_{em} = 615 nm. **HR-ESI-MS**: *m/z* = 306.5714 (38%, $[M-6PF_6-CH_3]^{6+}$) (calcd. 306.4133).

5.9 Syntheses of mononuclear and trinuclear ruthenium(II) complexes containing an amine functionality

The general method for the reaction between ligands **3** and **5** and complex precursor **6** was obtained from the literature, and modified accordingly to afford complexes **10** and **12**, respectively.[9,10]

*5.9.1 Synthesis of mononuclear ruthenium(II) complex(**10**)*

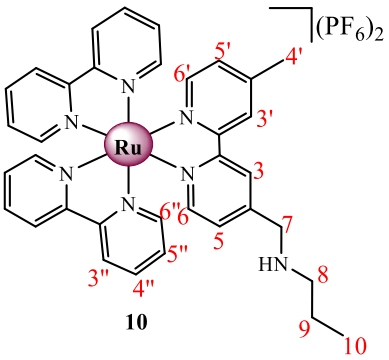

10

cis-Dichlorobis(2,2'-bipyridine)ruthenium(II) (0.131 g, 0.270 mmol) and compound **3** (78.1 mg, 0.324 mmol) were dissolved in ethanol/water (50:50) (40 mL) and refluxed for 18 h. The solvent was removed under reduced pressure to afford a red-orange residue. The chloride counter-anion was exchanged for hexafluorophosphate *via* a metathesis reaction, by dissolving the residue in minimum amount water (*ca.* 3 mL), followed by the addition of a saturated aqueous solution of ammonium hexafluorophosphate (*ca.* 10 mL) and stirred for 30 min. at room temperature. The product (**10**) was collected as a red solid *via* vacuum filtration and washed with water, diethyl ether and dried *in vacuo*.

Yield: (0.219 g, 86%). **Melting point**: 162–169 °C (decomposes with melting). **^{1}H NMR** (300 MHz, $(CD_3)_2CO$) δ_{ppm} 8.95 (d, ^{4}J = 0.6 Hz, 1H, H-3), 8.80 (dd, ^{3}J = 7.6 Hz, ^{4}J = 3.8 Hz, 4H, H-3''), 8.55 (s, 1H, H-3'), 8.26 – 8.11 (m, 5H, H-4''), 8.07 – 7.99 (m, 3H, H-6''), 7.99 – 7.95 (m, 1H, H-6'), 7.86 (d, ^{3}J = 5.8 Hz, 1H, H-5), 7.73 (dd, ^{3}J = 5.8 Hz, ^{4}J = 1.6 Hz, 1H, H-6), 7.63 – 7.49 (m, 4H, H-5''), 7.46 – 7.39 (m, 1H, H-5'), 4.75 (s, 2H, H-7), 2.84 (t, 2H, H-8), 2.57 (s, 3H, 4'-C**H**$_3$), 1.88 (dq, ^{3}J = 14.9 Hz, ^{3}J = 7.5 Hz , 2H, H-9), 1.01 (t, ^{3}J = 7.5 Hz, 3H, H-10). **^{13}C{^{1}H} NMR** (101 MHz, $(CD_3)_2CO$) δ_{ppm} 158.8 (**C**$_{Ar}$), 158.2 (**C**$_{Ar}$), 157.0 (**C**$_{Ar}$), 153.2 (**C**H$_{Ar}$), 152.6 (**C**H$_{Ar}$), 151.9 (**C**H$_{Ar}$), 142.8 (**C**$_{Ar}$), 139.0 (**C**H$_{Ar}$), 130.0 (**C**H$_{Ar}$), 129.2 (**C**H$_{Ar}$), 128.8 (**C**H$_{Ar}$), 126.5 (**C**H$_{Ar}$), 126.2 (**C**H$_{Ar}$), 125.4 (**C**H$_{Ar}$), 51.6 (C-8), 51.1 (C-7), 21.2 (4'-**C**H$_3$), 20.4

(C-9), 11.0 (C-10). **IR/ATR (ν/cm^{-1}):** weak (C=N)$_{bpy}$ 1605. **Emission:** λ_{em} = 616 nm. **HR-ESI-MS**: *m/z* = 327.6000 (100%, $[M-2PF_6]^{2+}$) (calcd. 327.3900), *m/z* = 946.1381 (100%, $[M+H]^{+}$) (calcd. 946.1273).

*5.9.2 Synthesis of trinuclear ruthenium(II) complex (**12**)*

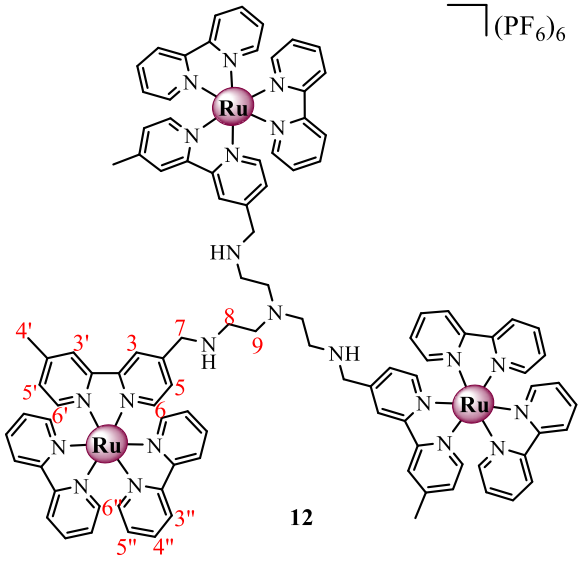

cis-Dichlorobis(2,2'-bipyridine)ruthenium(II) (0.586 g, 1.21 mmol) and compound **5** (0.279 g, 0.403 mmol) were dissolved in ethanol/water (50:50) (40 mL) and refluxed for 20 h. The solvent was removed under reduced pressure to afford a red-orange residue. The chloride counter-anion was exchanged for hexafluorophosphate *via* a metathesis reaction, by dissolving the residue in minimum amount water (*ca.* 3 mL), followed by the addition of a saturated aqueous solution of ammonium hexafluorophosphate (*ca.* 10 mL), which was stirred for 30 min. at room temperature. Compound **12** was collected as a red precipitate *via* gravity filtration and washed with water, diethyl ether and dried *in vacuo*.

Yield: (0.916 g, 81%). **Melting point**: onset occurs at 184 °C (decomposes without melting). **^{1}H NMR** (400 MHz, $(CD_3)_2CO$) δ_{ppm} 8.81 (s, 3H, H-3), 8.76 (m, 12H, H-3''), 8.57 (s, 3H, H-3'), 8.23 – 8.11 (m, 12H, H-4''), 8.04 (d, ^3J = 11.6 Hz, 3H, H-5), 8.02 – 7.94 (m, 12H, H-6''), 7.93 (d, ^3J = 5.8 Hz, 3H, H-6'), 7.86 – 7.78 (m, 3H, H-6), 7.62 – 7.44 (m, 12H, H-5''), 7.44 – 7.33 (m, 3H, H-5'), 4.88 (s, 6H, H-7), 2.58 (s, 9H, 4'-C**H**$_3$), 2.27 – 2.17 (m, 6H, H-9), 1.94 – 1.85 (m, 6H, H-8). **IR/ATR (ν/cm^{-1}):** weak (C=N)$_{bpy}$ 1605. **Emission:** λ_{em} = 614 nm.

5.10 General procedure for the radical thiol-ene photoredox catalysis

Photochemical reactions were irradiated with a custom-made blue LED light connected to a Weir Majoreg 441 power supply (Voltage: 34 V, Current: 0.5 A). All reagents were purchased from Sigma-Aldrich/Merck and were used as received. All reactions were carried out in an unsealed reaction tube at room temperature. Reaction progress was monitored using thin-layer chromatography (TLC) on pre-coated silica-gel F254 plates in ethyl acetate/hexane (1: 10 v/v) solvent system and visualised under UV light at 254 nm. Chromatography was performed with 60 Å silica gel (70–230 mesh ASTM). All photocatalytic reactions were carried out following a literature reported procedure, which was modified accordingly for each varied substrate.[11]

5.10.1 Photoredox catalytic reactions

A reaction tube was charged with a thiol, an alkene (1: 1, thiol: alkene), photocatalyst (**7-12**, 0.25 mol %) and *p*-toluidine (5 mol %) and acetonitrile (2 mL). The unsealed reaction tube was then irradiated under blue LED light while stirring at room temperature. Upon completion of the reaction, the reaction mixture was concentrated under reduced pressure and purified by column chromatography (ethyl acetate/hexane, 1: 10 v/v). Reported yields are for the model reaction carried out using the prototypical complex $[Ru(bpy)_3](PF_6)_2$ (**7**) as a photoredox catalyst. The yields for the other complexes (**8-12**) are given in Chapter 3, Sections 3.2.1–3.2.3. All reactions were carried out in duplicate and the reported yields are the average of two reproducible experiments.

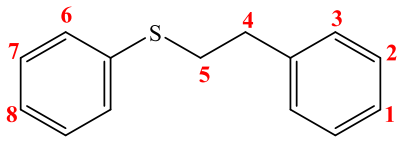

Yield: (54%). **^{1}H NMR** (400 MHz, $CDCl_3$) δ_{ppm} 7.38 (d, ^3J = 7.5 Hz, 2H, C**H$_{Ar}$**), 7.32 (t, ^3J = 6.5 Hz, 4H, C**H$_{Ar}$**), 7.24 – 7.17 (m, 4H, C**H$_{Ar}$**), 3.22 – 3.15 (m, 2H, H-5), 2.98 – 2.91 (m, 2H, H-4). R_f value = 0.37 (100% hexane). The spectroscopic data are consistent with reported values.[11,12]

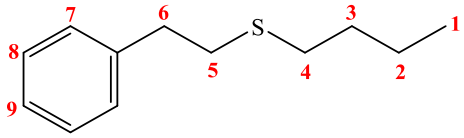

Yield: (39%). **^{1}H NMR** (400 MHz, $CDCl_3$) δ_{ppm} 7.44 – 7.14 (m, 5H, C**H$_{Ar}$**), 2.88 (dd, ^3J = 9.9 Hz, ^3J = 6.6 Hz, 2H, H-6), 2.81 – 2.72 (m, 2H, H-5), 2.58 – 2.49 (m, 2H, H-4), 1.58 (dt, ^3J = 15.1 Hz, ^3J = 7.5 Hz, 2H, H-3), 1.39 (dt, ^3J = 14.5 Hz, ^3J = 7.3 Hz, 2H, H-2), 0.91 (t, ^3J = 7.3 Hz, 3H, H-1). R_f = 0.79 (50% ethyl acetate: hexane). The spectroscopic data are consistent with reported values.[12]

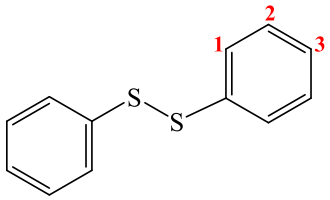

Yield: (18%). **^{1}H NMR** (400 MHz, $CDCl_3$) δ_{ppm} 7.52 (d, ^3J = 7.7 Hz, 4H, H-1), 7.32 (t, ^3J = 7.4 Hz, 4H, H-2), 7.24 (t, ^3J = 7.3 Hz, 2H, H-3). R_f value = 0.52 (100% hexane). The spectroscopic data are consistent with reported values.[13]

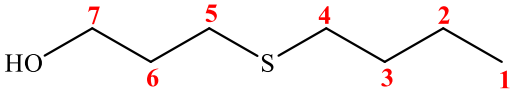

Yield: (not isolated). **^{1}H NMR** (400 MHz, $CDCl_3$) δ_{ppm} 3.77 – 3.72 (m, 2H, H-7), 2.62 (t, ^3J = 7.1 Hz, 2H, H-5), 2.55 – 2.49 (m, 2H, H-4), 1.88 – 1.80 (m, 2H, H-6), 1.61 – 1.51 (m, 2H, H-3), 1.39 (dq, ^3J = 14.4 Hz, ^3J = 7.2 Hz, 2H, H-2), 0.90 (t, ^3J = 7.3 Hz, 3H, H-1). R_f value = 0.31 (30% ethyl acetate: hexane). The spectroscopic data are consistent with reported values.[14]

5.11 References

1. B. M. Peek, G. T. Ross, S. W. Edwards, G. J. Meyer, T. J. Meyer and B. W. Erickson, *Int. J. Pept. Protein Res.*, 1991, **38**, 114-123.
2. P. Govender, S. Pai, U. Schatzschneider and G. S. Smith, *Inorg. Chem.*, 2013, **52**, 5470-5478.
3. S. Yao, A. M. Jones, J. Du, R. K. Jackson, J. O. Massing, D. P. Kennedy and W. R. Seitz, *Analyst*, 2012, **137**, 4734-4741.
4. B. P. Sullivan, D. J. Salmon and T. J. Meyer, *Inorg. Chem.*, 1978, **17**, 3334-3341.
5. C. H. Lin, H. C. Kao, C. J. Hsu and W. J. Wang, *J. Chin. Chem. Soc.*, 2010, **57**, 1167-1171.
6. A. Ito, N. Kobayashi and Y. Tek, *Inorg. Chem.*, 2017, **56**, 3794-3808.
7. M. J. Li, C. Q. Zhan, M. J. Nie, G. N. Chen and X. Chen, *J. Inorg. Biochem.*, 2011, **105**, 420-425.
8. J. Karges, F. Heinemann, F. Maschietto, M. Patra, O. Blacque, I. Ciofini and G. Gasser, *Bioorg. Med. Chem.*, 2019, **27**, 2666-2675.
9. M. D. Pratt and P. D. Beer, *Tetrahedron*, 2004, **60**, 11227-11238.
10. A. M. Cancelliere, F. Puntoriero, S. Serroni, S. Campagna, Y. Tamaki, D. Saito and O. Ishitani, *Chem. Sci.*, 2020, **11**, 1556-1563.
11. E. L. Tyson, M. S. Ament and T. P. Yoon, *J. Org. Chem.*, 2013, **78**, 2046-2050.
12. S. Chun, J. Chung, J. E. Park and Y. K. Chung, *ChemCatChem*, 2016, **8**, 2476-2481.
13. H. Loghmani-Khouzani, M. R. Poorheravi, M. M. Sadeghi, L. Caggiano and R. F. Jackson, *Tetrahedron*, 2008, **64**, 7419-7425.
14. J. V. Comasseto, R. A. Gariani, J. L. Princival, A. A. Dos Santos and F. K. Zinn, *J. Organomet. Chem.*, 2008, **693**, 2929-2936.

Appendix A

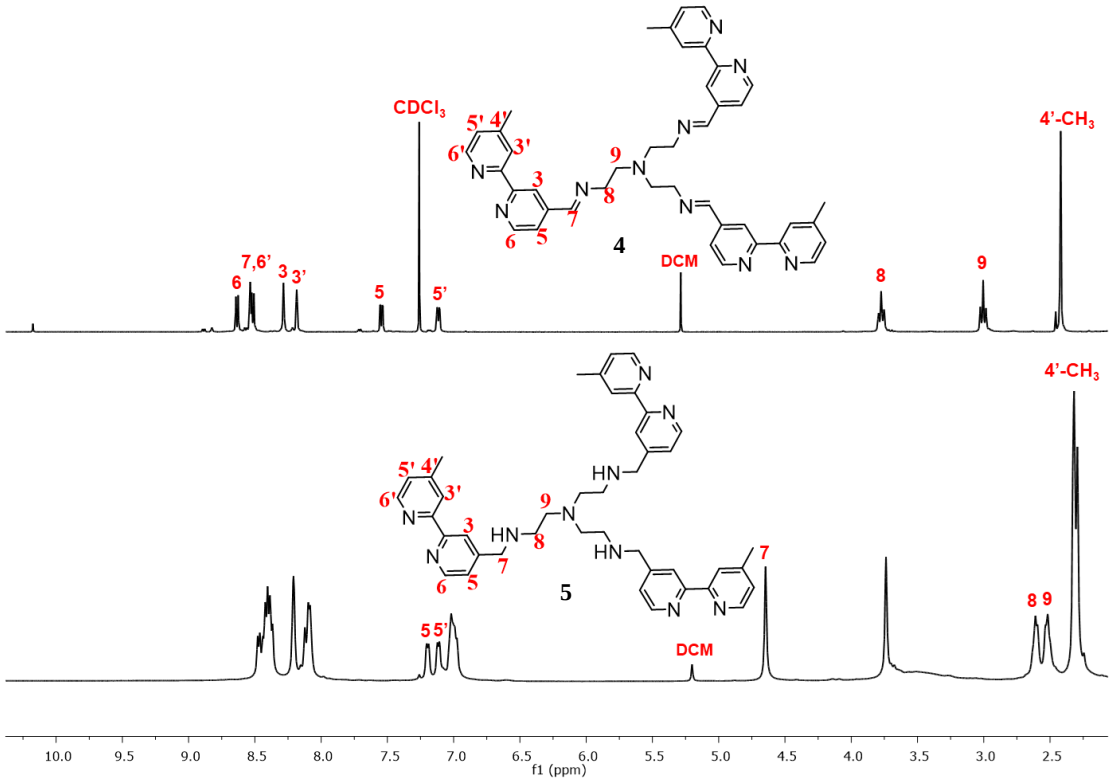

Figure A1 Stacked ^{1}H NMR spectra of trimeric ligands **4** and **5** in $CDCl_3$.

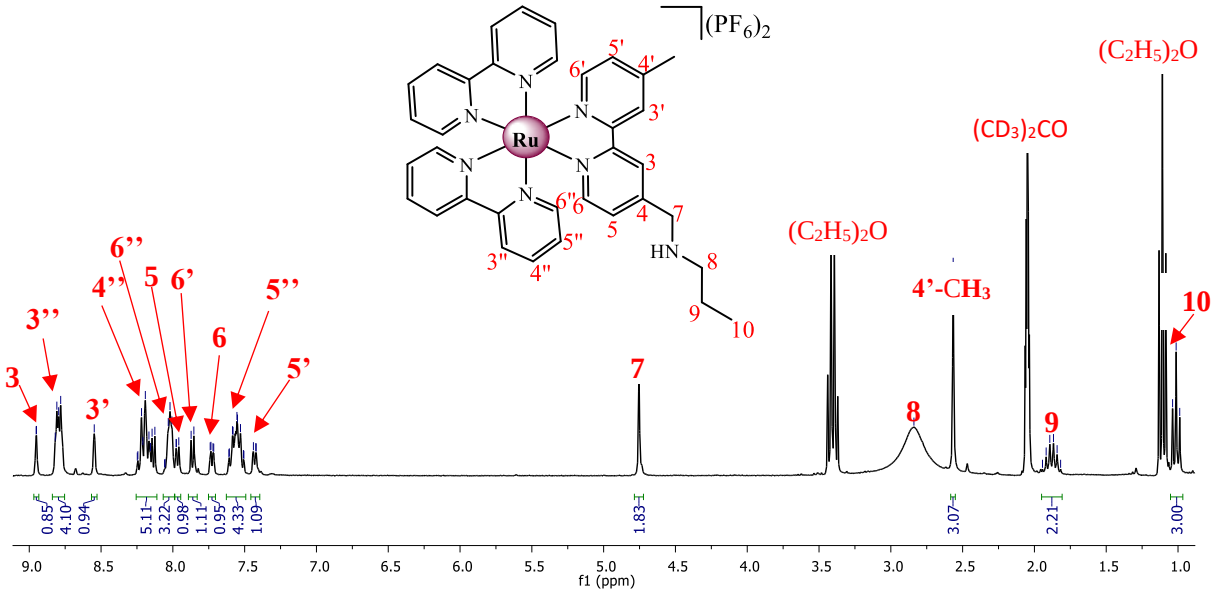

Figure A2 ^{1}H NMR spectrum of complex **10** in $(CD_3)_2CO$.

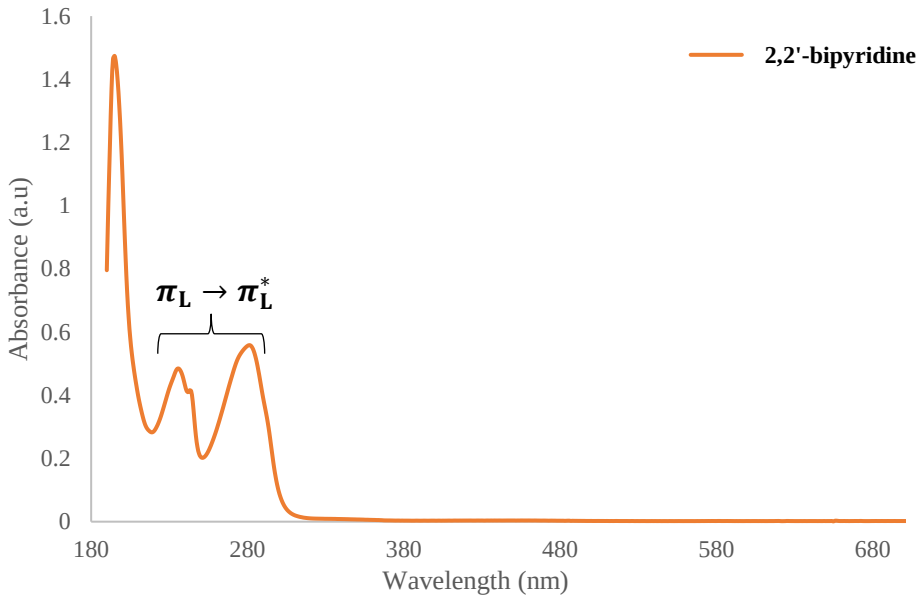

Figure A3 Electronic absorption spectrum of 2,2'-bipyridine (1×10^{-5} *M*) in anhydrous acetonitrile.